

**THE UNIVERSITY OF OKLAHOMA
GRADUATE COLLEGE**

EHD-ENHANCED HEAT AND MASS TRANSFER

**A DISSERTATION
SUBMITTED TO THE GRADUATE FACULTY**

In partial fulfillment of the requirement for the

Degree of

DOCTOR OF PHILOSOPHY

By

MEIRONG HUANG

Norman, Oklahoma

2005

UMI Number: 3203291



UMI Microform 3203291

Copyright 2006 by ProQuest Information and Learning Company.
All rights reserved. This microform edition is protected against
unauthorized copying under Title 17, United States Code.

ProQuest Information and Learning Company
300 North Zeeb Road
P.O. Box 1346
Ann Arbor, MI 48106-1346

EHD-ENHANCED HEAT AND MASS TRANSFER

**A DISSERTATION APPROVED FOR
THE SCHOOL OF AEROSPACE AND MECHANICAL ENGINEERING**

By

Dr. Feng-Chyuan Lai (Chair)

Dr. Ramkumar N. Parthasarathy

Dr. M. Cengiz Altan

Dr. Brandon W. Olson

Dr. Walter Wei

**© Copyright by Meirong Huang, 2005
All Rights Reserved**

ACKNOWLEDGMENTS

The author would like to express her appreciation and gratitude to Professor Feng-Chyuan Lai, for being an excellent advisor and the chairman of this dissertation committee. His guidance, motivation, and patience were the significant factors that contributed to the successful completion of this work. It was an honor and pleasure to work under his guidance.

The author also thanks Professor Ramkumar N. Parthasarathy, Professor M. Cengiz Altan, Professor Brandon W. Olson, Professor Walter Wei, Professor Ajay Agrawal, and Professor William H. Sutton for their time, effort, valuable advice and suggestions as members of this dissertation committee.

Especially, the author would like to thank Professor Kurt Gramoll for offering her financial supports for the last two years of her study.

The author would like to thank Professor Haiheng Zhao. His caring and encouragement have carried her through the entire course of her PhD study. The author also likes to thank her husband Rui and son Max for all their unconditional love and support that they have given her all the time. Without which this work could not have been accomplished. This work is dedicated to them.

ABSTRACT

The present study has addressed some fundamental issues involved in the heat and mass transfer enhancement by electric field. To examine the heat transfer enhancement by the electric field, forced convection in a horizontal channel has been first numerically modeled using two-way coupling between the electric field and the fluid field. Heat transfer enhancement in the presence of electric field has been evaluated by employing both one-way and two-way coupling models. Numerical solutions have been obtained for a wide range of governing parameters ($V_0 = 10.0, 12.5, 15.0$ and 17.5 kV as well as $u_i = 0.0759$ to 1.2144 m/s). Since the difference in the results obtained by these two approaches is insignificant, it is concluded that the assumption of one-way coupling is valid. Then, the heat transfer enhancement by electric field is examined for natural convection in an enclosure with the effects of Joule heating. Numerical solutions have been obtained for three electrode locations and a wide range of governing parameters ($Ra = 10^4, 10^5, \text{ and } 10^6$, and $V_0 = 12, 15, \text{ and } 18$ kV). The results obtained show that the effects of Joule heating are negligible when the Rayleigh number is large ($Ra \geq 10^5$). For a small Rayleigh number ($Ra = 10^4$), the effects of Joule heating are significant.

To study the mass transfer enhancement by the electric field, experiments have been conducted and the effects of corona wind ($V_0 = 14 - 20$ kV), corona polarities (positive and negative), and cross-flow ($u_i = 2.2$ m/s) on the evaporation rate of water have been carefully examined. Correlations have been proposed for the water evaporation rate under the application of electric field for both positive and negative corona polarities. Then, numerical models are developed for the electric, flow, and

concentration fields. Numerical results have been compared with the experiment results and the agreement between them is found to be satisfactory.

TABLE OF CONTENTS

ACKNOWLEDGMENTS	iv
ABSTRACT.....	v
TABLE OF CONTENTS	vii
LIST OF TABLES	x
LIST OF FIGURES	xi
NOMENCLATURE.....	xiv
CHAPTER ONE INTRODUCTION AND LITERATURE REVIEW.....	1
1.1 Introduction.....	1
1.2 EHD-enhanced Heat Transfer.....	3
1.2.1 EHD-enhanced Natural Convection	3
1.2.2 EHD-enhanced Forced Convection	5
1.3 EHD-enhanced Mass Transfer.....	6
1.4 Objective of Present Study.....	9
CHAPTER EHD-ENHANCED HEAT TRANSFER	12
2.1 Electric Field.....	12
2.1.1 Governing Equations	12
2.1.2 Numerical Formulation of Electric Field.....	13
2.2 EHD-enhanced Forced Convection Employing Two-way Coupling	17
2.2.1 Governing Equations for Fluid and Temperature Fields	19
2.2.2 Numerical Formulation of Flow and Temperature Fields	21
2.2.3 The Wood's Algorithm.....	24
2.2.4 Evaluation of Heat Transfer Results.....	25

2.2.6 Results and Discussion	28
2.3 EHD-enhanced Natural Convection with Joule Heating	40
2.3.1 Heat Generation for a Wire-plate System.....	42
2.3.2 Governing Equations for Flow and Temperature Fields.....	44
2.3.3 Evaluation of Heat Transfer Results	46
2.3.4 Code Validation	46
2.3.5 Results and Discussion	47
CHAPTER THREE EHD-ENHANCED MASS TRANSFER	54
3.1 Experiment Study.....	54
3.1.1 Experiment Setup.....	54
3.1.2 Experimental Apparatus.....	55
3.1.3 Experiment Procedure.....	61
3.1.4 Data Analysis	63
3.1.5 Calculation of Sherwood Number	64
3.1.5 Results and Discussion	66
3.2 Numerical Simulation	74
3.2.1 Electric Field.....	74
3.2.2 Flow and Concentration Fields	84
3.2.3 The Sherwood Number	87
3.2.4 Code Validation	88
3.2.5 Results and Discussion	92
CHAPTER FOUR CONCLUSIONS	101
4.1 EHD-enhanced Heat Transfer.....	101

4.2 EHD-enhanced Mass Transfer.....	102
4.3 Recommendations for Future Study	103
REFERENCES.....	105
APPENDIX A FLOW AND TEMPERATURE FIELDS FOR ONE-WAY AND TWO-WAY COUPLING MODELS.....	109
APPENDIX B FLOW AND TEMPERATURE FIELDS OF JOULE HEATING	131
APPENDIX C EXPERIMENT RESULTS.....	150

LIST OF TABLES

Table 2.1	Current at the grounded plates [10]	18
Table 2.2	The thermal and hydrodynamic entrance lengths for various inlet velocities .	27
Table 2.3	Comparison of Nusselt numbers obtained from empirical correlation [34] and present study	28
Table 2.4	Comparison of Nusselt numbers obtained from both one-way and two-way coupling models ($V_0 = 15.0$ kV).....	28
Table 2.5	Period of the oscillatory flow in EHD-enhanced forced convection	35
Table 2.6	Corona currents produced by various wire locations in the enclosure studied [8].....	42
Table 2.7	Comparison of Nusselt numbers obtained from correlation [37] and present study.....	47
Table 3.1	Comparison of Nusselt numbers for forced convection	91
Table 3.2	Comparison of Sherwood numbers (positive discharge, $u_i = 2.2$ m/s)	93
Table 3.3	Comparison of Sherwood numbers (positive discharge, $u_i = 1.0$ m/s)	95

LIST OF FIGURES

Figure 1.1	Mechanism of EHD-enhanced heat and mass transfer.....	2
Figure 2.1	The control volume of nodal P in a two-dimensional computational domain	14
Figure 2.2	A two-dimensional channel with constant wall temperature and one electrode wire located at the center ($L = 21$ cm, $H = 3$ cm)	19
Figure 2.3	Flow fields predicted by one-way coupling model for $V_0 = 15$ kV	30
Figure 2.4	Flow fields predicted by two-way coupling model for $V_0 = 15$ kV	31
Figure 2.5	Temperature fields predicted by one-way coupling model for $V_0 = 15$ kV .	32
Figure 2.6	Temperature fields predicted by two-way coupling model for $V_0 = 15$ kV .	33
Figure 2.7	Flow fields at $V_0 = 15$ kV and $Re = 450$ (one-way coupling model).....	36
Figure 2.8	Flow fields at $V_0 = 15$ kV and $Re = 450$ (two-way coupling model)	36
Figure 2.9	Temperature fields at $V_0 = 15$ kV and $Re = 450$ (one-way coupling model)	37
Figure 2.10	Temperature fields at $V_0 = 15$ kV and $Re = 450$ (two-way coupling model)	37
Figure 2.11	Modification of the electric field by air flow, $V_0 = 15$ kV and $u_i = 5$ m/s (a) charge density, (b) potential. (one-way – solid line, two-way – dashed line)	38
Figure 2.12	Heat transfer enhancement as a function of EHD number	39
Figure 2.13	Wire positions in the two-dimensional enclosure ($L = 4$ inches).....	41
Figure 2.14	Electric diagram for a wire-plate system.....	43
Figure 2.15	Temperature fields at the wire position 2 ($V_0 = 12$ kV, $Ra = 10^4$, with Joule heating)	50
Figure 2.16	Temperature fields at the wire position 2 ($V_0 = 12$ kV, $Ra = 10^4$, without Joule heating).....	50
Figure 2.17	Flow fields at the wire position 2 ($V_0 = 12$ kV).....	51

Figure 2.18	Temperature fields at the wire position 2 ($V_0 = 12$ kV).....	51
Figure 2.19	Heat transfer enhancement with the effect of Joule heating (a) position 1, (b) position 2, (c) position 3.	52
Figure 2.20	Heat transfer enhancement without the effect of Joule heating (a) position 1, (b) position 2, (c) position 3.	53
Figure 3.1	Experiment setup	56
Figure 3.2	Blower	57
Figure 3.3	High-voltage power supply	57
Figure 3.4	Digital balance.....	58
Figure 3.5	Temperature/Humidity data logger	59
Figure 3.6	Variation of ambient temperature and humidity recorded by the data logger	60
Figure 3.7	Statistical data recorded by the data logger.....	60
Figure 3.8	Van velocimeter.....	61
Figure 3.9	Typical experimental results with an applied voltage of 16 kV without cross-flow	64
Figure 3.10	Water evaporation enhancement without cross-flow for both positive and negative corona discharge.....	69
Figure 3.11	Water evaporation enhancement with cross-flow for both positive and negative corona discharge ($u_i = 2.2$ m/s)	69
Figure 3.12	Variation of Sherwood number with EHD Reynolds number in the absence of cross-flow.....	71
Figure 3.13	Water evaporation enhancement in the absence of cross-flow	71
Figure 3.14	Variation of Sherwood number with the EHD number in the presence of cross-flow	73
Figure 3.15	Water evaporation enhancement in the presence of cross-flow	74
Figure 3.16	A two-dimensional channel with a pool of water in the bottom wall	76

Figure 3.17	The symmetric geometric channel for electric field numerical simulation..	77
Figure 3.18	The surface and contour used to determine the boundary conditions at the interface between two dissimilar dielectrics	78
Figure 3.19	Imaginary nodal points.....	82
Figure 3.20	Electric field in a two-dimensional channel with a pool of water in the bottom wall ($V_0 = 18$ kV), (a) electric potential (b) charge density ...	84
Figure 3.21	Computational domain for the simulation of flow and concentration fields	85
Figure 3.22	The physical model of heat transfer by forced convection.....	89
Figure 3.23	Heat transfer from a flat plate with unheated sections	89
Figure 3.24	Variation of flow fields with applied voltage ($u_i = 2.2$ m/s)	97
Figure 3.25	Variation of concentration fields with applied voltage	98
Figure 3.26	Variation of flow fields with applied voltage ($u_i = 1.0$ m/s)	99
Figure 3.27	Variation of concentration fields with applied voltage	100

NOMENCLATURE

A	surface area of the channel wall, [m ²]
A_c	surface area of the water surface, [m ²]
A_p	surface area of the copper plate, [m ²]
A_{wire}	cross-sectional area of the wire, [m ²]
b	ion mobility, [m ² /V·s]
b_a	ion mobility of air, [m ² /V·s]
b_w	ion mobility of water, [m ² /V·s]
c_w	water vapor concentration at the sample surface, [kg/m ³]
c_∞	water vapor concentration in air, [kg/m ³]
c_p	specific heat, [J/kg·K]
d	diameter of the wire electrode, [m]
D	electric flux vector, [C/ m ²]
D	mass diffusivity, [m ² /s]
D_h	hydraulic diameter of the channel, [m]
E	electric field vector, [V/m]
E_x	x-component electric field, [V/m]
E_y	y-component electric field, [V/m]
g	gravitational acceleration, [m/s ²]
h	convective heat transfer coefficient, [W/m ² ·K]
H	height of the computational domain, [m]

I	corona current, [A]
\mathbf{J}	current density vector, [A/m ²]
k	thermal conductivity, [W/m·K]
L	length of the channel, or width of the enclosure, [m]
Le	Lewis number, α/D
L_h	hydrodynamic entrance length, [m]
L_p	length of the wire, [m]
L_t	thermal entrance length, [m]
L_w	length of the water surface, [m]
\dot{m}	mass transfer rate, [kg/s]
N_{EHD}	EHD number
Nu	average Nusselt number, hL/k
Nu_x	local Nusselt number, hx/k
\overline{Nu}	time-averaged Nusselt number
p	pressure, [Pa]
Pe	Peclet number, $PrRe$
Pe_{EHD}	Peclet number, $PrRe_{EHD}$
P_g	saturated vapor pressure, [Pa]
Pr	Prandtl number, ν/α
R	electrical resistance of the wire, [Ω]
Ra	Relyleigh number, $g\beta(T_h - T_c)L^3/\nu\alpha$
Re	Reynolds number, u_iH/ν
Re_{EHD}	Reynolds number, u_eL/ν

s	distance between the emitting electrode and ground surface, [m]
Sh	Sherwood number, $\alpha_D L_w / D$
t	time, [s]
T	temperature, [K]
T_c	temperature of the cold wall, [K]
T_h	temperature of the hot wall, [K]
T_i	temperature of air at inlet, [K]
T_w	wall temperature, [K]
T_∞	temperature of the ambient air in the lab, [K]
u	velocity in x-direction, [m/s]
\mathbf{u}	velocity vector, [m/s]
u_e	characteristic velocity of ionic wind, $\sqrt{\rho_{e0} V_0 / \rho}$
u_i	cross-flow velocity, [m/s]
v	velocity in the y-direction, [m/s]
V	electric potential, [V]
V_0	electric potential at the wire, [V]
\bar{V}	dimensionless electric potential, V/V_0
x, y	Cartesian coordinate, [m]
X, Y	dimensionless Cartesian coordinates
α	thermal diffusivity, [m ² /s]
α_D	mass transfer coefficient, [m/s]
β	coefficient of thermal expansion, [1/K]
ϵ_0	permittivity of free space, [F/m]

ϵ_a	permittivity of air, [F/m]
ϵ_w	permittivity of water, [F/m]
ν	kinematic viscosity, [m ² /s]
θ	dimensionless temperature
ϕ	relative humidity
ρ	fluid density, [kg/m ³]
ρ_c	space charge density, [C/m ³]
ρ_{c0}	space charge density at the wire, [C/m ³]
ρ_e	electrical resistivity of copper, [Ω -m]
ρ_s	surface charge density, [C/m ²]
$\overline{\rho_c}$	dimensionless space charge density, ρ_c/ρ_{c0}
τ	dimensionless time
ω	specific humidity, [kg water vapor/kg dry air]
ψ	dimensionless stream function
Ω	dimensionless vorticity

CHAPTER ONE

INTRODUCTION AND LITERATURE REVIEW

1.1 Introduction

Heat and mass transfer between a surface and its ambient air can be significantly enhanced through the application of a high electric field. When a high voltage is applied to a fine wire or a sharp needle, air in its vicinity is ionized and the ions are drawn toward the electrically grounded plates (Figure 1.1). During the migration to the plate electrodes, the ions transfer their momentum to neutral molecules by collision. A bulk flow of ionized air molecules is thus created, and is called corona wind, or secondary flow. The corona wind disturbs the boundary layer on the grounded surface and thus enhances heat and mass transfer between the grounded surface and its ambient air. This technique is called electrohydrodynamically enhanced (or EHD-enhanced) heat and mass transfer [1].

The advantages of heat and mass transfer enhancement by electric field are

1. The implementation is simple by using only a small transformer and electrodes (needles, wires or mesh).
2. Heat and mass transfer coefficients can be rapidly controlled by adjusting the electric field strength.
3. This technique can be applied to special environments, like zero-gravity.
4. CFC alternatives, oils, and liquids with relatively small electrical conductivity, as well as gases are all acceptable working fluids at the present level of EHD technology.
5. The electric power consumption is usually negligible in many applications [1].

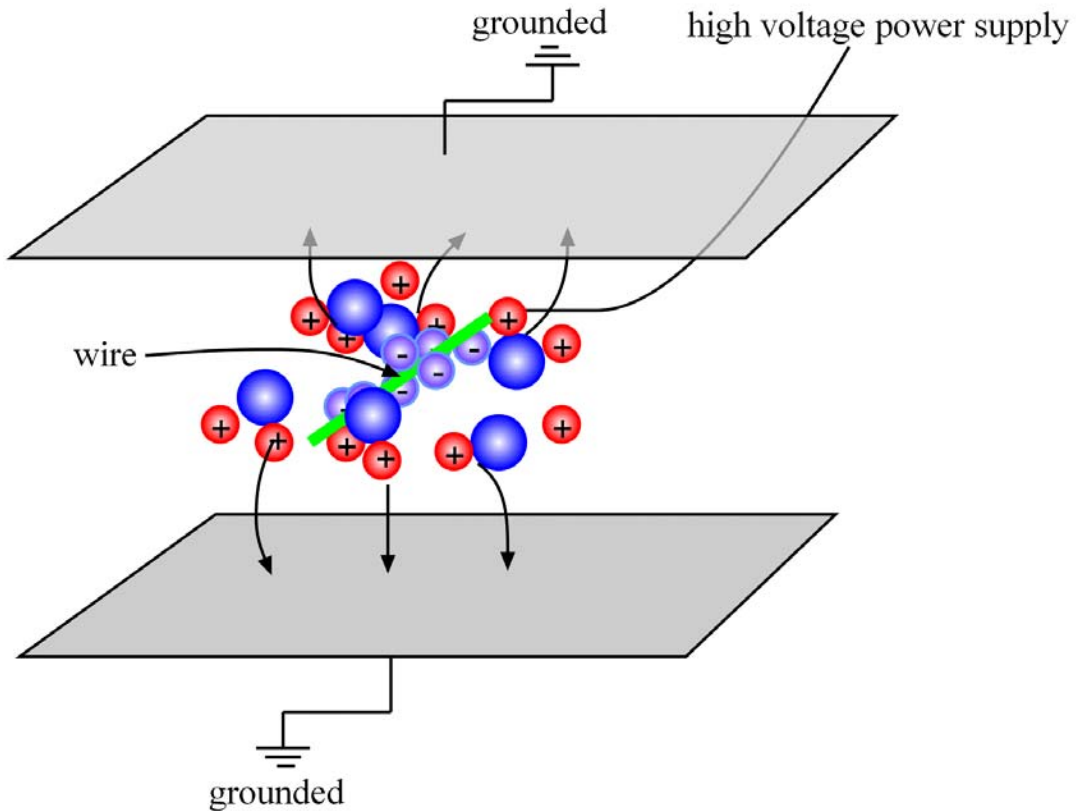


Figure 1.1 Mechanism of EHD-enhanced heat and mass transfer

EHD technique can be applied to various heat and mass transfer processes, such as convection, boiling, condensation, and evaporation [1]. The complication of EHD-enhanced heat and mass transfer is due to the interactions among the electric, flow, temperature, and concentration fields. Also, different EHD phenomena are involved with different substances. Therefore, the EHD-enhancement phenomenon is system-specific. The enhancement of heat and mass transfer using electric field has long been demonstrated by experiments. Due to the complexity of the problem, numerical solutions are often difficult to obtain. This chapter presents a literature review on EHD-enhanced

heat transfer in natural and forced convection, as well as EHD-enhanced mass transfer in drying.

1.2 EHD-enhanced Heat Transfer

1.2.1 EHD-enhanced Natural Convection

EHD-enhanced natural convection has been investigated by Lykoudis and Yu as early as 1962 [2]. In their experiment, the natural convection between a horizontally heated wire and a coaxial cooled cylinder under a non-uniform radial electric field was examined. They reported that the enhancement of convection was due to the additional recirculation produced by the electric force. Similar to the work by Lykoudis and Yu [2], Marco and Velkoff [3] used flat plates instead of coaxial cylinder. It was found that the corona wind led to the increase of approximately five times the pure natural convection in the experiments. The photographs demonstrated that the enhancement was due to the disruption of the thermal boundary layer. Later, Franke [4] investigated the effect of vortices induced by corona discharge on natural convection from a vertical plate. His results showed that heat transfer rate was doubled with the presence of an electric field.

Yabe et al. [5] developed a model to analyze experimentally and theoretically on the effect of corona wind. In their experiment, a fine wire was used as an anode and a plate was used as a cathode in a two-dimensional enclosure filled with nitrogen. Yabe et al. [5] found that positive ions predominated in the whole space, except in an extremely narrow region close to the wire. A theoretical analysis was performed based on the model that positive ions produced by ionization near the wire electrode moved toward the plate. The electric potential distribution in the space was calculated numerically. It was

shown that the corona wind was caused by the Coulomb force exerted on ions, and collisions of ions and neutral molecules of gas.

Franke and Hutson [6] investigated the effects of corona wind on natural convection inside a vertical hollow cylinder. By calculating the heat input required to maintain the inner surface of the cylinder at a constant temperature, the heat transfer rate was found to be nearly doubled along the inner surface due to the effect of the corona wind.

Recently, some numerical solutions of EHD-enhanced natural convection have been reported. Liu and Lai [7] performed numerical simulations to study the effects of wire location on the EHD-enhanced natural convection in an enclosure. It was found that the enhancement in heat transfer was possible due to the oscillation of the flow field. When the wire was located at the lower part of the enclosure, the effect of EHD-enhanced heat transfer was more significant than those of other wire locations. The maximum EHD-enhanced heat transfer rate was four times higher than those without the electric field. Following Liu and Lai's work [7], Tan and Lai [8] considered a two-dimensional cavity with an aspect ratio of 5 and applied positive corona discharge from an electrode wire charged from a high voltage supply in several locations. The enclosure was differentially heated from the vertical walls. It was observed that at low Rayleigh numbers, the flow and temperature fields were basically oscillatory in nature. When the Rayleigh number was sufficiently increased, a steady state might be reached. Heat transfer enhancement was found to increase with the applied voltage, but decrease with the Rayleigh number. Similar to Tan and Lai's work [8], Ngo and Lai [9] presented some numerical results for the effects of electric field on natural convection in an enclosure

filled with air and heated from below. The geometry considered was a two-dimensional rectangular cavity with an aspect ratio of one fifth. Ngo and Lai [9] also found that the flow and temperature fields might become steady, periodic, or non-periodic depending on the applied voltage and Rayleigh number. Because of the EHD-induced oscillatory flows, heat transfer was enhanced and was most significant at small Rayleigh numbers.

1.2.2 EHD-enhanced Forced Convection

Yamamoto and Velkoff [10] experimentally and numerically studied the secondary flow interaction in an electrostatic precipitator. A two-dimensional, laminar flow model was used. In the experiment, a Schlieren system and mist-injected smoke was used to visualize the interaction of the secondary flows. In the numerical study, the electric field distribution and space charge density were determined by using the Maxwell's equation, Poisson's equation, and the current continuity equation. Then the flow field was determined by solving the Navier-Stokes equations in term of vorticity and stream function. The numerical results were found to be consistent with the experiment results.

Tada et al. [11] conducted experiments in a channel with airflow in which equally spaced positive wire electrodes were placed in parallel to the primary flow. Tada et al. [11] found that heat transfer augmentation resulting from the combined flow was achieved, especially in the laminar flow range. Also, a theoretical analysis was performed on electric, flow, and temperature fields, taking into account the interactions among them.

Kulkarni and Lai [12] studied laminar mixed convection in a vertical channel. The electrical field was generated by positive corona discharge from a wire electrode.

The parameters considered in their study were the Reynolds numbers ($Re = 600, 1200,$ and 1800) and Grashof numbers ($Gr = 10^4, 10^5,$ and 10^6). Their results showed that heat transfer improved for Grashof number up to 10^5 for aiding flows. For opposing flows, heat transfer was increased in all cases of Reynolds and Grashof numbers. The flow and temperature fields was oscillatory for low Reynolds numbers ($Re = 600$ and 1200) and tended to stabilize when the Reynolds or Grashof numbers were increased.

Mathew and Lai [13] presented a numerical study of EHD-enhanced forced convection using two electrodes in a horizontal channel. Various electric potentials and Reynolds numbers were considered in their study. For a given electric field, flow and temperature fields were oscillatory at small Reynolds numbers and tended to stabilize when the Reynolds number was increased. Heat transfer was increased as much as 375% when compared with the cases without electric field due to the existence of oscillatory secondary flows.

Owsenek and Seyed-Yagoobi [14] conducted an experiment by suspending multiple fine wire electrodes in the open air above a grounded and heated horizontal surface. An infrared camera was used to obtain a complete and accurate distribution of local heat transfer coefficient on the impingement surface. Also, a numerical code was developed and verified by comparison with the experimental data.

1.3 EHD-enhanced Mass Transfer

EHD-enhanced mass transfer offers a wide range of applications to food-processing, textile, biomedical and mining sectors of the industry. Extensive experimental results on EHD-enhanced drying have been published. Kulacki and Daubenmier [15] studied the effect of corona wind on drying cookie dough. Their results

showed that when an electric field was applied, the baking time was 20% less than those without electric field. Kirschvink-Kobayashi and Kirschvink [16] conducted an experimental study using various materials. Their results showed a reduction in drying time from 20% to 50% for drying filter paper, wool, and chopped onions with the application of electric field. It was found that the corona wind produced by the electric field disturbed the boundary layer and increased the rate of water evaporation.

Similarly, Chen and Barthakur [17] conducted an experiment to study the dehydration of a potato slab with the presence of electric field. Compared with the convectional air-drying, the drying rate was increased 2.2 to 3.0 times when the potato slab was subjected to fluxes of 3.02×10^{12} positive ions/cm²-s alone or in combination with 7.31×10^{12} negative ions/cm²-s. It was concluded that the enhancement in drying was caused by the ion-drag force. Hashinaga et al. [18] studied EHD-enhanced drying technique experimentally using apple slices. It was found that the sharper needle was more efficient than the blunter copper electrode and the multiple point-to-plate electrodes. Also, using AC voltage was more effective in enhancing the drying rate.

Carlson and Latham [19] performed experiments to measure the drying rate of discs of paper towel moistened by water as a function of the strength of the electric field in which they were placed. The results showed that for a certain strength of electric field, the rate of mass loss (dm/dt) remained constant until the substrate started to become dry. Also, mass loss (dm/dt) varied monotonically with the strength of electric field.

Banarjee and Law [20] developed a laboratory system for experimentally characterizing electro-osmotic dewatering of two biomass materials at both constant voltage and constant current. The experimental results revealed that the dominant

mechanism of water removal in the experiments was via electroosmosis. In the constant-voltage mode, the flow rate of liquid water out of the bed linearly increased with the applied voltage. In the constant-current model, the electrical energy consumed was a quadratic function of time.

Sadek et al. [21] examined the heat and mass transfer coefficients in a forced convection system. A saturated sponge was placed on a flat plate and an air stream flowed tangentially. An array of wire electrodes was set on a certain distance above the flat surface to produce a corona wind impinging on the flat plate. The results showed that the drying rate of wet materials was governed by simultaneous heat and mass transfer in the hot gas passed through. Also, the electrohydrodynamic augmentation of heat and mass transfer rates with small-diameter or sharp electrodes was due to ion-drag forces, and was correlated under forced convection by means of the ratio of ion-drag and momentum forces.

Wolny [22] and Wolny and Kaniuk [23] experimentally investigated the process of evaporation from flat and cylindrical surfaces into an air stream flowing tangentially to them. The results confirmed that an electric field could significantly intensify heat and mass transfer in the evaporation and drying processes, up to eight times higher heat and mass transfer coefficients were observed with the presence of the electric field than those without. An increase in the gas flow velocity was observed over the liquid surface diminished the effect of electric field. Also, an increase in the gas temperature intensified gas ionization; and, augmented the transport processes significantly.

Barthakur and Arnold [24] used a point-to-plate electrode system to study the enhancement in the evaporation rates of water. It was observed that the turbulence

produced in the water by the electric wind caused the observed enhancement without any primary heat involvement. Also, the mass transfer coefficient for positive corona was higher because of its lower mobility than its negative counterpart if everything else remained the same.

EHD-enhanced drying has been experimentally evaluated by Lai and Lai [25] using a wire electrode to dry glass beads saturated with water. Their experiments were conducted for a wide range of operating voltage, electrode spacing and different size of sample materials. The results showed that the drying rate depended on the strength of the electric field and the velocity of the cross-flow. The enhancement of drying rate increased linearly with the applied voltage with the absence of cross-flow, but the electric field became insignificant on the drying enhancement when the cross-flow velocity was increased. With the same experiment setup, Lai and Wong [26] studied the EHD-enhanced drying using a needle. They also concluded that the drying rate depended on the strength of the electric field and the velocity of the cross-flow. In addition, they realized that positive corona discharge generally performed better than negative corona discharge, and wire electrode performed better than needle electrode at a lower applied voltage.

1.4 Objective of Present Study

Due to the complicated interactions among the electric, flow, and temperature fields, previous studies on heat transfer enhancement by electric field were mostly accomplished by experiments. Numerical solutions are only usually possible with some simplification of these complicated interactions. Two of the most common assumptions made are the one-way coupling between the electric and flow fields and the neglect of the

Joule heating caused by the electric field. Under the one-way coupling assumption (i.e., the ions travel at a much faster velocity than the ambient air), electric field can have influences on the flow field, but not vice versa. The second assumption is commonly used to simplify the energy equation. Although these assumptions may seem reasonable (and deemed necessary in some cases), they have never been verified.

Similarly, experiments on EHD-enhanced mass transfer have been conducted by drying various materials (for example, cookie dough [15], chopped onion [16], filter paper [16], wool [16], potato slab [17], apple slice [18], paper towel [19], and biomass materials [20]), very few numerical studies have been reported. Since the drying process takes place between gas/vapor and liquid phases, an interface exists. As such, in numerical studies, one needs to deal with the interface problem when solving for both electric and flow fields. The two-phase interface problems have been studied by several investigators [27-29], but their numerical solutions are based on an unjustified assumption that both space charge and surface charge are negligible. This assumption leads to a simple Laplacian equation for the electric field.

$$\nabla^2 V = 0. \tag{1.1}$$

In boiling, one substance occurs in two phase, such as water in vapor and liquid phase. The value of the specific dielectric constant is approximately 1 for gases and vapors and in the range of 5 to 10 for most dielectric liquids [27]. For the drying mentioned above [15-20], the substances are air in gas and water in liquid and vapor. In this case, the space charge cannot be neglected and the electric field is governed by two equations [1].

$$\nabla^2 V = -\frac{\rho_c}{\epsilon}, \tag{1.2}$$

$$\nabla \rho_c \cdot (b\mathbf{E} + \mathbf{u}) + b \frac{\rho_c^2}{\varepsilon} = 0. \quad (1.3)$$

At the interface, the surface charge also exists, which makes the problem more complicated. Particularly, the ratio of specific dielectric constant between water and air (at room temperature) ($\varepsilon_w / \varepsilon_a$) is 80.1; the ratio of ion mobility between air and water (b_a / b_w) is about 1000 [1, 30], which makes the numerical simulation of the interface even more difficult.

Based on the above analysis, the objectives of the present study can be summarized below:

1. Verify the one-way coupling assumption by a comparison of the results obtained from both one-way and two-way coupling models as applied to the problem of EHD-enhanced forced convection in a horizontal channel.
2. Verify the effects of Joule heating by investigating the heat transfer enhancement due to the Joule heating from a wire electrode located at the mid-plane of an enclosure, which is subjected to differentially heated vertical walls.
3. Experimentally and numerically study the EHD-enhanced water evaporation in a horizontal channel, with or without cross-flow.

CHAPTER TWO

EHD-ENHANCED HEAT TRANSFER

This chapter presents the numerical studies on the EHD-enhanced heat transfer. First, EHD-enhanced forced convection in a two-dimensional channel with electric field produced by a wire suspended in the air is studied to verify the one-way coupling assumption. Then, the EHD-enhanced natural convection in an enclosure is studied to evaluate the effect of Joule heating on the heat transfer enhancement using electric field.

2.1 Electric Field

2.1.1 Governing Equations

The electric field involved in the present study is governed by Maxwell equation, current continuity equation, and Ohm's law with the following assumptions [1].

1. Only positive corona discharge is considered since it provides a stable electric field.
2. The mobility of air is considered constant.
3. The specific dielectric constant is unity, so the permittivity of air equals the permittivity of vacuum.
4. The magnetic field due to the corona discharge is negligible.

Maxwell equation

$$\nabla \cdot \mathbf{D} = \rho_c. \quad (2.1)$$

Current continuity equation

$$\frac{d\rho}{dt} + \nabla \cdot \mathbf{J} = 0. \quad (2.2)$$

The time-dependent term in equation (2.2) reduces to zero when a steady DC power source is applied.

Ohm's law

$$\mathbf{J} = \rho_c \mathbf{bE} + \rho_c \mathbf{u}. \quad (2.3)$$

where \mathbf{u} is the free-stream velocity, which provides the coupling between the flow field and electric field.

From the definitions of the electric flux and electric potential

$$\mathbf{D} = \varepsilon \mathbf{E}, \quad \mathbf{E} = -\nabla V. \quad (2.4)$$

equation (2.1) can be rewritten as

$$\nabla^2 V = -\frac{\rho_c}{\varepsilon}. \quad (2.5)$$

Combining equations (2.3) and (2.5), equation (2.2) can be reformulated to give

$$\nabla \rho_c \cdot (\mathbf{bE} + \mathbf{u}) + b \frac{\rho_c^2}{\varepsilon} = 0. \quad (2.6)$$

So the governing equations for the electric field are equations (2.5) and (2.6).

2.1.2 Numerical Formulation of Electric Field

In Cartesian coordinates, equations (2.5) and (2.6) become

$$\frac{\partial^2 V}{\partial x^2} + \frac{\partial^2 V}{\partial y^2} = -\frac{\rho_c}{\varepsilon}, \quad (2.7)$$

$$b \frac{\rho_c^2}{\varepsilon} + \frac{\partial \rho_c}{\partial x} (bE_x + u) + \frac{\partial \rho_c}{\partial y} (bE_y + v) = 0. \quad (2.8)$$

A uniform mesh is used to discretize the governing equations. The computational domain is first divided into a two-dimensional grid system (Figure 2.1). Then the

governing equations are integrated over a control volume to get the finite difference form of governing equations. The finite difference form of equation (2.7) is given by

$$\int_{y,s}^{y,n} \int_{x,w}^{x,e} \left(\frac{\partial V^2}{\partial x^2} + \frac{\partial V^2}{\partial y^2} \right) dx dy = - \int_{y,s}^{y,n} \int_{x,w}^{x,e} \frac{\rho_c}{\varepsilon} dx dy, \quad (2.9)$$

$$\left(\frac{V_E - V_P}{x_E - x_P} - \frac{V_P - V_W}{x_P - x_W} \right) (y_n - y_s) + \left(\frac{V_N - V_P}{y_N - y_P} - \frac{V_P - V_S}{y_P - y_S} \right) (x_e - x_w)$$

$$= - \frac{\rho_c}{\varepsilon} (x_e - x_w) (y_n - y_s).$$

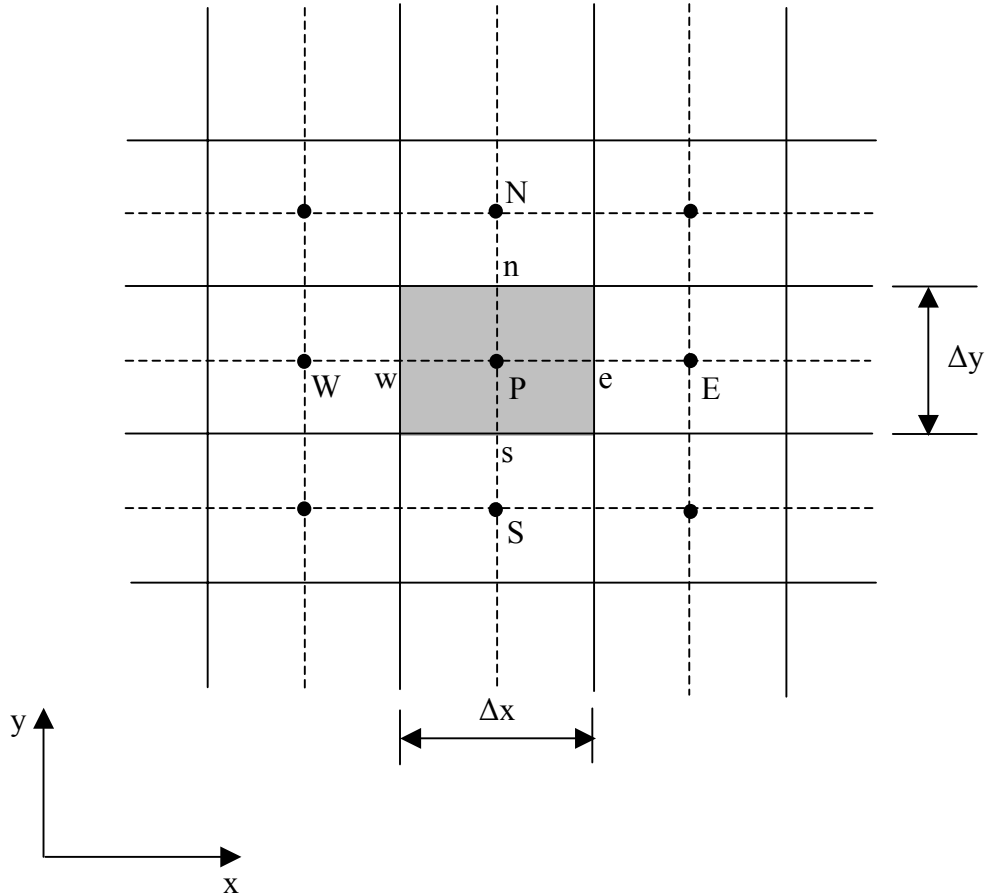


Figure 2.1 The control volume of nodal P in a two-dimensional computational domain

For a uniform grid, $\Delta x = \Delta y = \Delta$, equation (2.9) can be simplified to give

$$V_P = \frac{1}{4}(V_E + V_W + V_N + V_S) + \frac{\rho_c}{\varepsilon} \Delta^2. \quad (2.10)$$

The finite difference form of equation (2.8) is given by

$$\int_{y,s}^{y,n} \int_{x,w}^{x,e} b \frac{\rho_c^2}{\varepsilon} dx dy + \int_{y,s}^{y,n} \int_{x,w}^{x,e} \frac{\partial \rho_c}{\partial x} (bE_x + u) dx dy + \int_{y,s}^{y,n} \int_{x,w}^{x,e} \frac{\partial \rho_c}{\partial y} (bE_y + v) dx dy = 0,$$

$$b \frac{\rho_c^2}{\varepsilon} \Delta x \Delta y + (\rho_{ce} - \rho_{cw})(bE_x + u)(y_n - y_s) + (\rho_{cn} - \rho_{cs})(bE_y + v)(x_e - x_w) = 0. \quad (2.11)$$

In solving equation (2.11), a backward difference scheme is employed for numerical stability, and this can be summarized in four forms [31].

$$(1) \quad bE_x + u \geq 0 \quad \text{and} \quad bE_y + v \geq 0$$

Equation (2.11) is reformulated to give

$$b \frac{\rho_c^2}{\varepsilon} \Delta + (\rho_{cP} - \rho_{cW})(bE_x + u) + (\rho_{cP} - \rho_{cS})(bE_y + v) = 0,$$

which can be rearranged to give

$$\frac{b\Delta}{\varepsilon} \rho_{cP}^2 + [(bE_x + u) + (bE_y + v)] \rho_{cP} + [-(bE_x + u)\rho_{cW} - (bE_y + v)\rho_{cS}] = 0. \quad (2.12a)$$

$$(2) \quad bE_x + u \leq 0 \quad \text{and} \quad bE_y + v \geq 0$$

Equation (2.11) is reformulated to give

$$b \frac{\rho_c^2}{\varepsilon} \Delta + (\rho_{cE} - \rho_{cP})(bE_x + u) + (\rho_{cP} - \rho_{cS})(bE_y + v) = 0,$$

which can be rearranged to give

$$\frac{b\Delta}{\varepsilon} \rho_{cP}^2 + [-(bE_x + u) + (bE_y + v)] \rho_{cP} + [(bE_x + u)\rho_{cE} - (bE_y + v)\rho_{cS}] = 0. \quad (2.12b)$$

$$(3) \quad bE_x + u \leq 0 \quad \text{and} \quad bE_y + v \leq 0$$

Equation (2.11) is reformulated to give

$$b \frac{\rho_c^2}{\varepsilon} \Delta + (\rho_{cE} - \rho_{cP})(bE_x + u) + (\rho_{cN} - \rho_{cP})(bE_y + v) = 0,$$

which can be rearranged to give

$$\frac{b\Delta}{\varepsilon} \rho_{cP}^2 + [-(bE_x + u) - (bE_y + v)] \rho_{cP} + [(bE_x + u)\rho_{cE} + (bE_y + v)\rho_{cN}] = 0. \quad (2.12c)$$

$$(4) \quad bE_x + u \geq 0 \quad \text{and} \quad bE_y + v \leq 0$$

Equation (2.11) is reformulated to give

$$b \frac{\rho_c^2}{\varepsilon} \Delta + (\rho_{cP} - \rho_{cW})(bE_x + u) + (\rho_{cN} - \rho_{cP})(bE_y + v) = 0,$$

which can be rearranged to give

$$\frac{b\Delta}{\varepsilon} \rho_{cP}^2 + [(bE_x + u) - (bE_y + v)] \rho_{cP} + [-(bE_x + u)\rho_{cW} + (bE_y + v)\rho_{cN}] = 0. \quad (2.12d)$$

Equation (2.12) has the form

$$a(\rho_{cP})^2 + b(\rho_{cP}) + c = 0.$$

To solve for charge density (ρ_{cP}), we use the formula of $\rho_{cP} = \frac{-b \pm \sqrt{b^2 - 4ac}}{2a}$.

For one-way coupling, which implies that $u = 0$ and $v = 0$ in equation (2.12), the present algorithm used to calculate the electric field is reduced to that proposed by Yamamoto and Velkoff [10]. In one-way coupling approach, the electric field can be determined independently of the flow field following the steps outlined below.

1. The potential distribution is first estimated by solving equation (2.10) with the absence of the charge density.

2. After the potential distribution is known, the charge density can be determined by solving equation (2.12) with an initial guess of the charge density at the wire.
3. With the charge density given, the potential distribution can be recalculated using equation (2.10).
4. With the newly available potentials, the charge density can be updated by solving equation (2.12) again.
5. The process is repeated until both potential and charge density converge. When converged, the current on the grounded surface is calculated using

$$I = \int_0^L \rho_c b E_y L_P dx. \quad (2.13)$$

6. If this value agrees well with the experimental data ($\left| \frac{I - I_{\text{exp}}}{I} \right| \leq 10^{-4}$), then the electric field is determined. Otherwise, a new charge density at the wire is assumed and the process is repeated from step two.

In two-way coupling approach, the electric field has to be determined simultaneously with the flow field. At each time step, the electric field is first calculated, followed by the flow field. After the flow field is determined, the electric field is recalculated using the most recently available velocity data. In each time step, the electric field is determined using the same procedures as one-way coupling approach.

2.2 EHD-enhanced Forced Convection Employing Two-way Coupling

In this study, two-way coupling is considered in EHD-enhanced forced convection. The system considered is shown in Figure 2.2. Because of the symmetry, only half of the channel was used as the computational domain. A finite difference

method based on the control volume approach was used to solve the governing equations subject to the boundary conditions imposed. A uniform grid (225×33) has been shown to produce satisfactory results [35]. In addition, a time step of 5×10^{-4} has been shown to be adequate for the present calculations [35].

To obtain the electric field numerically, the current density on the grounded plate first needs to be determined experimentally. Since this channel has the same configuration as the one that Yamamoto and Velkoff [10] used in their experiment, their experimental current data (shown in Table 2.1) were used in the present numerical study.

The corresponding boundary conditions for the electric potential field are

$$x = L/2, \quad y = 0, \quad V = V_0. \quad (2.14a)$$

$$y = H, \quad V = 0. \quad (2.14b)$$

$$y = 0, \quad \frac{\partial V}{\partial y} = 0. \quad (2.14c)$$

$$x = 0, \quad \frac{\partial V}{\partial x} = 0. \quad (2.14d)$$

$$x = L, \quad \frac{\partial V}{\partial x} = 0. \quad (2.14e)$$

Table 2.1 Current at the grounded plates [10]

Voltage (kV)	Current measured at the grounded plates (A)
10.0	3.4e-5
12.5	8.8e-5
15.0	16.0e-5
17.5	2.48e-4

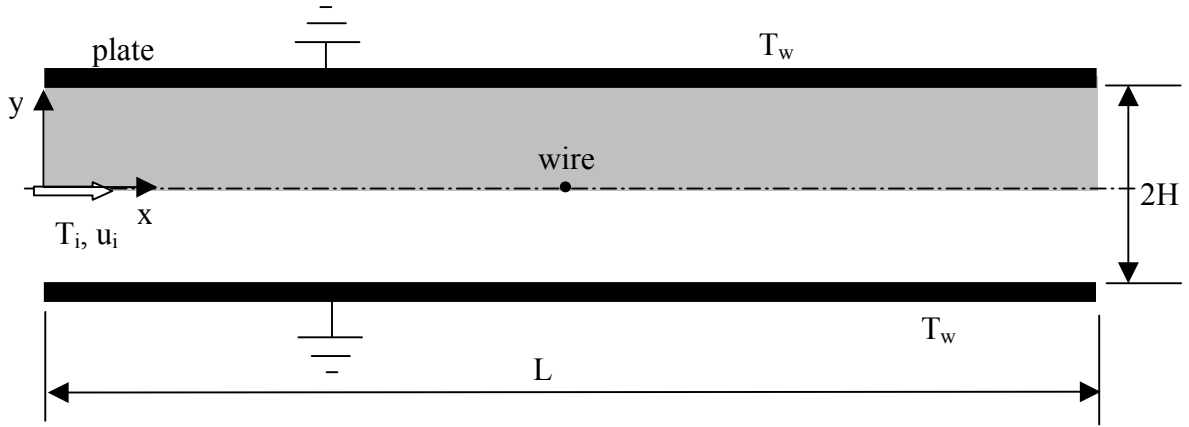


Figure 2.2 A two-dimensional channel with constant wall temperature and one electrode wire located at the center ($L = 21$ cm, $H = 3$ cm)

2.2.1 Governing Equations for Fluid and Temperature Fields

The governing equations for the unsteady flow and temperature fields with constant properties are continuity equation, momentum equations in x and y direction, and the energy equation.

$$\frac{\partial u}{\partial x} + \frac{\partial v}{\partial y} = 0, \quad (2.15)$$

$$\frac{\partial u}{\partial t} + u \frac{\partial u}{\partial x} + v \frac{\partial u}{\partial y} = -\frac{1}{\rho} \frac{\partial p}{\partial x} + \nu \left(\frac{\partial^2 u}{\partial x^2} + \frac{\partial^2 u}{\partial y^2} \right) + \frac{\rho_c}{\rho} E_x, \quad (2.16)$$

$$\frac{\partial v}{\partial t} + u \frac{\partial v}{\partial x} + v \frac{\partial v}{\partial y} = -\frac{1}{\rho} \frac{\partial p}{\partial y} + \nu \left(\frac{\partial^2 v}{\partial x^2} + \frac{\partial^2 v}{\partial y^2} \right) + \frac{\rho_c}{\rho} E_y, \quad (2.17)$$

$$\frac{\partial T}{\partial t} + u \frac{\partial T}{\partial x} + v \frac{\partial T}{\partial y} = \alpha \left(\frac{\partial^2 T}{\partial x^2} + \frac{\partial^2 T}{\partial y^2} \right). \quad (2.18)$$

The last term in the momentum equations, equations.(2.16) and (2.17), represents the electric body force, which provides the coupling from the electric field to the flow field.

The effects of Joule heating are assumed negligible in this heat transfer application.

The governing equations can be non-dimensionalized by introducing the following dimensionless variables.

$$\begin{aligned}
X &= \frac{x}{H}, & Y &= \frac{y}{H}, & \theta &= \frac{T - T_w}{T_i - T_w}, & \tau &= \frac{u_i t}{H}, & \text{Pr} &= \frac{\nu}{\alpha}, \\
U &= \frac{u}{u_i}, & V &= \frac{v}{u_i}, & \Omega &= \frac{\omega H}{u_i}, & \bar{V} &= \frac{V}{V_0}, & \bar{\rho}_c &= \frac{\rho_c}{\rho_{c0}}, \\
u_e &= \sqrt{\frac{\rho_{c0} V_0}{\rho}}, & & & U &= \frac{\partial \Psi}{\partial Y}, & V &= -\frac{\partial \Psi}{\partial X}, & \text{Re} &= \frac{u_i H}{\nu}.
\end{aligned} \tag{2.19}$$

In the model of two-way coupling, the charge density at the wire (ρ_{c0}) changes in each time step, so the electric characteristic velocity u_e is no longer a constant. Therefore, the inlet velocity u_i is used as the reference velocity. This is different from the previous studies based on the one-way coupling. The dimensionless governing equations in terms of stream function and vorticity are given by

Vorticity Equation

$$\frac{\partial^2 \Psi}{\partial X^2} + \frac{\partial^2 \Psi}{\partial Y^2} = -\Omega, \tag{2.20}$$

Vorticity Transport Equation

$$\frac{\partial \Omega}{\partial \tau} + \frac{\partial \Psi}{\partial Y} \frac{\partial \Omega}{\partial X} - \frac{\partial \Psi}{\partial X} \frac{\partial \Omega}{\partial Y} = \frac{1}{\text{Re}} \left(\frac{\partial^2 \Omega}{\partial X^2} + \frac{\partial^2 \Omega}{\partial Y^2} \right) + \frac{u_e^2}{u_i^2} \left(\frac{\partial \bar{\rho}_c}{\partial Y} \frac{\partial \bar{V}}{\partial X} - \frac{\partial \bar{\rho}_c}{\partial X} \frac{\partial \bar{V}}{\partial Y} \right), \tag{2.21}$$

Energy Equation

$$\frac{\partial \theta}{\partial \tau} + \frac{\partial \Psi}{\partial Y} \frac{\partial \theta}{\partial X} - \frac{\partial \Psi}{\partial X} \frac{\partial \theta}{\partial Y} = \frac{1}{\text{Pr Re}} \left(\frac{\partial^2 \theta}{\partial X^2} + \frac{\partial^2 \theta}{\partial Y^2} \right). \tag{2.22}$$

The corresponding boundary conditions for the flow and temperature fields are

$$X=0, \quad \Omega=0, \quad \Psi=Y, \quad \theta=1. \tag{2.23}$$

$$X = \frac{L}{H}, \quad \frac{\partial \Omega}{\partial X} = 0, \quad \frac{\partial \Psi}{\partial X} = 0, \quad \frac{\partial \theta}{\partial X} = 0. \quad (2.24)$$

$$Y = 0, \quad \Omega = 0, \quad \Psi = 0, \quad \frac{\partial \theta}{\partial Y} = 0. \quad (2.25)$$

$$Y = 1, \quad \Omega = -\frac{\partial^2 \Psi}{\partial^2 Y}, \quad \Psi = 1, \quad \theta = 0. \quad (2.26)$$

Numerical results reported by Kulkarni and Lai [12] have shown that the outflow condition, equation (2.24), is appropriate for the determination of the flow and temperature fields.

2.2.2 Numerical Formulation of Flow and Temperature Fields

A finite difference method [31] is employed to solve these governing equations of the flow and temperature fields. Similar to the electric field, a uniform mesh is used to discretize the governing equations, and the finite difference equations are obtained by integrating the governing equations over a control volume (Figure 2.1). The diffusion terms in the vorticity equation can be discretized in the following manner.

$$\int_{X_w}^{X_e} \int_{Y_s}^{Y_n} \left(\frac{\partial^2 \Psi}{\partial X^2} + \frac{\partial^2 \Psi}{\partial Y^2} \right) dXdY = \int_{Y_s}^{Y_n} \left(\frac{\partial \Psi}{\partial X} \Big|_e - \frac{\partial \Psi}{\partial X} \Big|_w \right) dY + \int_{X_w}^{X_e} \left(\frac{\partial \Psi}{\partial Y} \Big|_n - \frac{\partial \Psi}{\partial Y} \Big|_s \right) dX. \quad (2.27)$$

Applying the central difference approximation to the above equation gives

$$\int_{Y_s}^{Y_n} \left(\frac{\partial \Psi}{\partial X} \Big|_e - \frac{\partial \Psi}{\partial X} \Big|_w \right) dY = \frac{\Psi_E - \Psi_P}{X_E - X_P} (Y_n - Y_s) - \frac{\Psi_P - \Psi_W}{X_P - X_W} (Y_n - Y_s), \quad (2.28)$$

$$\int_{X_w}^{X_e} \left(\frac{\partial \Psi}{\partial Y} \Big|_n - \frac{\partial \Psi}{\partial Y} \Big|_s \right) dX = \frac{\Psi_N - \Psi_P}{Y_N - Y_P} (X_e - X_w) - \frac{\Psi_P - \Psi_S}{Y_P - Y_S} (X_e - X_w),$$

$$\int_{X_w}^{X_e} \int_{Y_s}^{Y_n} \left(\frac{\partial^2 \Psi}{\partial X^2} + \frac{\partial^2 \Psi}{\partial Y^2} \right) dXdY = (B_E \Psi_E + B_W \Psi_W + B_N \Psi_N + B_S \Psi_S) - (B_E + B_W + B_N + B_S) \Psi_P, \quad (2.29)$$

where

$$\begin{aligned}
B_E &= \frac{Y_n - Y_s}{X_E - X_P}, & B_W &= -\frac{Y_n - Y_s}{X_P - X_W}, \\
B_N &= \frac{X_e - X_w}{Y_N - Y_P}, & B_S &= \frac{X_e - X_w}{Y_P - Y_S}.
\end{aligned} \tag{2.30}$$

For uniform grid ($\Delta X = \Delta Y = \Delta$),

$$B_E = B_W = B_N = B_S = 1. \tag{2.31}$$

In the same manner, the diffusion terms in the vorticity transport and energy equations are discretized into the following forms.

$$\frac{1}{\text{Re}} \int_{X_w}^{X_e} \int_{Y_s}^{Y_n} \left(\frac{\partial^2 \Omega}{\partial X^2} + \frac{\partial^2 \Omega}{\partial Y^2} \right) dXdY = \frac{1}{\text{Re}} (\Omega_E + \Omega_W + \Omega_N + \Omega_S - 4\Omega_P), \tag{2.32}$$

$$\frac{1}{\text{Pr Re}} \int_{X_w}^{X_e} \int_{Y_s}^{Y_n} \left(\frac{\partial^2 \theta}{\partial X^2} + \frac{\partial^2 \theta}{\partial Y^2} \right) dXdY = \frac{1}{\text{Pr Re}} (\theta_E + \theta_W + \theta_N + \theta_S - 4\theta_P). \tag{2.33}$$

The convective terms in the vorticity transport equation are integrated over the control volume to obtain the following discretized form.

$$\begin{aligned}
& \int_{X_w}^{X_e} \int_{Y_s}^{Y_n} \left(\frac{\partial \Psi}{\partial Y} \frac{\partial \Omega}{\partial X} - \frac{\partial \Psi}{\partial X} \frac{\partial \Omega}{\partial Y} \right) dXdY \\
&= \int_{Y_s}^{Y_n} \left(\frac{\partial \Psi}{\partial Y} \Big|_e \Omega_e - \frac{\partial \Psi}{\partial Y} \Big|_w \Omega_w \right) dY + \int_{X_w}^{X_e} \left(\frac{\partial \Psi}{\partial X} \Big|_n \Omega_n - \frac{\partial \Psi}{\partial X} \Big|_s \Omega_s \right) dX, \\
&= (A_E + A_W + A_N + A_S) \Omega_P - (A_E \Omega_E + A_W \Omega_W + A_N \Omega_N + A_S \Omega_S),
\end{aligned} \tag{2.34}$$

where

$$\begin{aligned}
A_E &= \frac{1}{8} [(\Psi_{SE} + \Psi_S - \Psi_{NE} - \Psi_N) + |\Psi_{SE} + \Psi_S - \Psi_{NE} - \Psi_N|], \\
A_W &= \frac{1}{8} [(\Psi_{NW} + \Psi_N - \Psi_{SW} - \Psi_S) + |\Psi_{NW} + \Psi_N - \Psi_{SW} - \Psi_S|], \\
A_N &= \frac{1}{8} [(\Psi_{NE} + \Psi_E - \Psi_{NW} - \Psi_W) + |\Psi_{NE} + \Psi_E - \Psi_{NW} - \Psi_W|], \\
A_S &= \frac{1}{8} [(\Psi_{SW} + \Psi_W - \Psi_{SE} - \Psi_E) + |\Psi_{SW} + \Psi_W - \Psi_{SE} - \Psi_E|].
\end{aligned} \tag{2.35}$$

In the same manner, the convective terms in the energy equation are discretized into the following form.

$$\begin{aligned}
& \int_{X,w}^{X,e} \int_{Y,s}^{Y,n} \left(\frac{\partial \Psi}{\partial Y} \frac{\partial \theta}{\partial X} - \frac{\partial \Psi}{\partial X} \frac{\partial \theta}{\partial Y} \right) dXdY \\
&= \int_{Y,s}^{Y,n} \left(\frac{\partial \Psi}{\partial Y} \Big|_e \theta_e - \frac{\partial \Psi}{\partial Y} \Big|_w \theta_w \right) dY + \int_{X,w}^{X,e} \left(\frac{\partial \Psi}{\partial X} \Big|_n \theta_n - \frac{\partial \Psi}{\partial X} \Big|_s \theta_s \right) dX, \\
&= (A_E + A_W + A_N + A_S) \theta_P - (A_E \theta_E + A_W \theta_W + A_N \theta_N + A_S \theta_S),
\end{aligned} \tag{2.36}$$

where A_E , A_W , A_N , and A_S are given in equation (2.35). The electric body force term in the vorticity transport equation (2.21) is integrated to obtain the following discretized form.

$$\begin{aligned}
& \frac{u_e^2}{u_i^2} \int_{Y,s}^{Y,n} \int_{X,w}^{X,e} \left(\frac{\partial \bar{\rho}_c}{\partial Y} \frac{\partial \bar{V}}{\partial X} - \frac{\partial \bar{\rho}_c}{\partial X} \frac{\partial \bar{V}}{\partial Y} \right) dXdY \\
&= \frac{u_e^2}{u_i^2} [(\bar{V}_e - \bar{V}_w)(\bar{\rho}_{c,n} - \bar{\rho}_{c,s}) - (\bar{V}_n - \bar{V}_s)(\bar{\rho}_{c,e} - \bar{\rho}_{c,w})], \\
&= \frac{u_e^2}{u_i^2} \left[\left(\frac{\bar{V}_E - \bar{V}_P}{2} - \frac{\bar{V}_P - \bar{V}_W}{2} \right) \left(\frac{\bar{\rho}_{c,N} - \bar{\rho}_{c,P}}{2} - \frac{\bar{\rho}_{c,P} - \bar{\rho}_{c,S}}{2} \right) - \right. \\
&\quad \left. \left(\frac{\bar{V}_N - \bar{V}_P}{2} - \frac{\bar{V}_P - \bar{V}_S}{2} \right) \left(\frac{\bar{\rho}_{c,E} - \bar{\rho}_{c,P}}{2} - \frac{\bar{\rho}_{c,P} - \bar{\rho}_{c,W}}{2} \right) \right],
\end{aligned} \tag{2.37}$$

The time-derivative terms in the vorticity transport and energy equations are discretized into the following form by forward difference approximation.

$$\begin{aligned}
& \int_{X,w}^{X,e} \int_{Y,s}^{Y,n} \left(\frac{\partial \Omega}{\partial Y} \right) dXdY = \frac{\Omega_P^{t+1} - \Omega_P^t}{\Delta \tau} \Delta^2, \\
& \int_{X,w}^{X,e} \int_{Y,s}^{Y,n} \left(\frac{\partial \theta}{\partial Y} \right) dXdY = \frac{\theta_P^{t+1} - \theta_P^t}{\Delta \tau} \Delta^2.
\end{aligned} \tag{2.38}$$

Finally, the vorticity, vorticity transport and energy equations at a new time step (t+1) can be evaluated numerically after substituting all the discretized terms at the previous time step (t). They are summarized below.

Vorticity Equation

$$\Psi_P^{t+1} = \frac{1}{4} \left[\Psi_E^t + \Psi_W^t + \Psi_N^t + \Psi_S^t + \Omega_P^t \Delta^2 \right]. \quad (2.39)$$

Vorticity Transport Equation

$$\Omega_P^{t+1} = \Omega_P^t + \frac{\Delta\tau}{\Delta^2} \left\{ \left[\frac{1}{\text{Re}_{\text{EHD}}} \left(\left(\sum_{i=E,W,N,S} \Omega_i^t \right) - 4\Omega_P^t \right) \right] - \left[\left(\sum_{i=E,W,N,S} A_i \right) \Omega_P^t - \left(\sum_{i=E,W,N,S} A_i \Omega_i^t \right) \right] + \text{Electric body force term} \right\},$$

$$\begin{aligned} \text{Electric body force term} = & \left(\frac{\overline{V_E} - \overline{V_P}}{2} - \frac{\overline{V_P} - \overline{V_W}}{2} \right) \left(\frac{\overline{\rho_{c,N}} - \overline{\rho_{c,P}}}{2} - \frac{\overline{\rho_{c,P}} - \overline{\rho_{c,S}}}{2} \right) \\ & - \left(\frac{\overline{V_N} - \overline{V_P}}{2} - \frac{\overline{V_P} - \overline{V_S}}{2} \right) \left(\frac{\overline{\rho_{c,E}} - \overline{\rho_{c,P}}}{2} - \frac{\overline{\rho_{c,P}} - \overline{\rho_{c,W}}}{2} \right). \end{aligned} \quad (2.40)$$

Energy Equation

$$T_P^{t+1} = T_P^t + \frac{\Delta\tau}{\Delta^2} \left\{ \left[\frac{1}{\text{Pr Re}} \left(\left(\sum_{i=E,W,N,S} T_i^t \right) - 4T_P^t \right) \right] - \left[\left(\sum_{i=E,W,N,S} A_i \right) T_P^t - \left(\sum_{i=E,W,N,S} A_i T_i^t \right) \right] \right\}. \quad (2.41)$$

2.2.3 The Wood's Algorithm

The vorticity of the wall can be calculated using Wood's algorithm as following.

Evaluate the stream function at the node just next to the wall (Ψ_{w+1}) in terms of the stream function at the wall (Ψ_w) using Taylor series expansion, which yields

$$\begin{aligned}\Psi_{W+1} = \Psi_W + \left(\frac{\partial\Psi}{\partial Y}\right)_W (Y_{W+1} - Y_W) \\ + \frac{1}{2}\left(\frac{\partial^2\Psi}{\partial Y^2}\right)_W (Y_{W+1} - Y_W)^2 + \frac{1}{3}\left(\frac{\partial^3\Psi}{\partial Y^3}\right)_W (Y_{W+1} - Y_W)^3 + \dots\end{aligned}\quad (2.42)$$

Since

$$\left(\frac{\partial\Psi}{\partial Y}\right)_W = 0, \quad \left(\frac{\partial^2\Psi}{\partial Y^2}\right)_W = -\Omega_W, \quad \text{and} \quad \left(\frac{\partial^3\Psi}{\partial Y^3}\right)_W = -\left.\frac{\partial\Omega}{\partial Y}\right|_W,$$

the vorticity at the wall can be determined from the previous equation (2.42) by

$$\Omega_W = -\frac{3(\Psi_{W+1} - \Psi_W)}{\Delta^2} - \frac{1}{2}\Omega_{W+1}.\quad (2.43)$$

2.2.4 Evaluation of Heat Transfer Results

To evaluate the heat transfer results, the local Nusselt number at the wall is calculated by [32, 33]

$$Nu_x = \frac{hD_h}{k}.$$

$$\text{Since } Q = Ah(T_w - T_m) = -kA \left.\frac{\partial T}{\partial y}\right|_{y=H},$$

$$\text{One obtains } Nu_x = -\frac{D_h}{T_w - T_m} \left.\left(\frac{\partial T}{\partial y}\right)\right|_{y=H}.\quad (2.44)$$

In the dimensionless form, this yields

$$Nu_x = \frac{D_h}{L} \frac{T_i - T_w}{T_w - T_m} \left.\left(\frac{\partial\theta}{\partial Y}\right)\right|_{Y=1}.\quad (2.45)$$

Here T_m is the mean bulk temperature. The temperature difference $(T_w - T_m)$ was obtained using the Logarithmic Mean Temperature Difference (LMTD) [32].

The average Nusselt number can then be obtained from the local Nusselt number by

$$\text{Nu} = \frac{1}{A} \int_0^A \text{Nu}_x \, dx. \quad (2.46)$$

For periodic flows, the time-averaged Nusselt number is determined by averaging the Nusselt number over a period of oscillation and is given by

$$\overline{\text{Nu}} = \frac{1}{\tau_p} \int_{\tau}^{\tau+\tau_p} \text{Nu} \, d\tau, \quad (2.47)$$

where τ_p is the period of oscillation, and Nu is determined from equation (2.46) at each time step.

For non-periodic flows, the average Nusselt number is determined by averaging the Nusselt number over a long period of time after the initial transient settles.

$$\overline{\text{Nu}} = \frac{1}{\tau_1} \int_{\tau}^{\tau+\tau_1} \text{Nu} \, d\tau. \quad (2.48)$$

2.2.5 Code Validation

To validate the code, it has been tested against the heat transfer by forced convection in a horizontal channel without electric field. The channel considered is 21cm long and 6 cm high. From literature [34], the thermal and hydrodynamic entrance lengths can be evaluated using the following correlations.

The thermal entrance length

$$L_t = 0.0797 D_h \text{Pe}. \quad (2.49)$$

The hydrodynamic entrance length

$$L_h = D_h \left(\frac{0.315}{0.0175 \text{Re} + 1} + 0.011 \text{Re} \right). \quad (2.50)$$

where $D_h = 4A/P = 12$ cm is the hydraulic diameter of the channel. For different inlet velocities, the corresponding thermal and hydrodynamic entrance lengths are listed in Table 2.2. Since the channel is only 21 cm long, the flow is simultaneously developing. Nusselt number for the laminar simultaneously developing flows is given by the following empirical correlation [34].

$$Nu_0 = 7.55 + \frac{0.024(x^*)^{-1.14}}{1 + 0.0358(x^*)^{-0.64} Pr^{0.17}}, \quad (2.51)$$

$$x^* = \frac{x}{D_h Re Pr}.$$

The results from both numerical simulation (Nu) and equation (2.51) (Nu_0) are listed in Table 2.3 for comparison. Depending on the Reynolds number, the discrepancies between these two results vary from one to eight percent, which is acceptable in the consideration of the uncertainty involved in the correlation itself.

Table 2.2 The thermal and hydrodynamic entrance lengths for various inlet velocities

Inlet Velocity (m/s)	Re_{Dh}	L_t (m)	L_h (m)
0.0759	600	4.19	0.80
0.1518	1200	8.38	1.59
0.2277	1800	12.6	2.38
0.3036	2400	16.8	3.17
0.3795	3000	20.9	3.96
0.4554	3600	25.1	4.75
0.5313	4200	29.3	5.54
0.6072	4800	33.5	6.34
0.9108	7200	50.3	9.50
1.2144	9600	67.0	12.7

Table 2.3 Comparison of Nusselt numbers obtained from empirical correlation [34] and present study

Inlet Velocity u_i (m/s)	$Re = D_h u_i/\nu$	Nu_0	Nu	$\left \frac{Nu - Nu_0}{Nu} \right \times 100\%$
0.0759	600	13.45	14.60	7.9
0.1518	1200	17.57	18.32	4.1
0.2277	1800	20.93	21.07	0.7
0.3036	2400	23.83	23.40	1.8
0.3795	3000	26.42	25.48	3.7
0.4554	3600	28.78	27.10	6.3

Table 2.4 Comparison of Nusselt numbers obtained from both one-way and two-way coupling models ($V_0 = 15.0$ kV)

Inlet Velocity (m/s)	$Re = \frac{u_i H}{\nu}$	Nusselt Number						Forced Convection
		One-way Coupling			Two-way Coupling			
		Min.	Average	Max.	Min.	Average	Max.	
0.0759	150	38.65	45.79	53.01	38.12	45.77	53.60	14.60
0.1518	300	45.18	53.50	63.31	43.99	53.97	65.68	18.32
0.2277	450	41.86	46.31	51.09	42.51	47.26	52.45	21.07
0.3036	600		37.02			36.89		23.40
0.3795	750		36.74			36.71		25.48
0.4554	900		37.08			37.07		27.10
0.5315	1050		37.41			37.40		28.65
0.6072	1200		37.70			37.69		30.06
0.9108	1800		38.72			38.73		34.80
1.2144	2400		40.73			40.71		38.50

2.2.6 Results and Discussion

Numerical simulations were performed using a Pentium 4 personal computer. For one-way coupling model, it took 2.1 hours for calculations to advance 100 dimensionless time, but 6.75 hours were needed for two-way coupling model to proceed the same amount of calculations. For the iteration of stream function, relative convergence criterion was used. If $\left| (\psi_{\text{new}} - \psi_{\text{old}}) / \psi_{\text{new}} \right| \leq 10^{-4}$, then it was assumed that stream functions were converged.

Table 2.4 summarizes the heat transfer results obtained from both one-way and two-way coupling models at an applied voltage of 15.0 kV and the Reynolds number varying from 150 to 2400. For steady periodic flows, the minimum, maximum and average Nusselt numbers in an oscillating period are given. The Nusselt number at the same Reynolds number without electric field is also listed in the table for comparison.

One can observe from the table when the flow and temperature fields are steady (for example, $V_0 = 15$ kV, and $Re = 600$ to 2400), the Nusselt numbers obtained both from one-way and two-way coupling are almost the same. Also, the contours of the flow and temperature fields (in terms of streamlines and isotherms, respectively) are exactly the same (Figures 2.3 – 2.6). Both show that a secondary flow (i.e., recirculating cell) appears directly above the wire (the circle in the center of the lower boundary) as the result of the interaction between the corona wind and the primary flow. The impingement of the corona wind on the wall perturbs the thermal boundary layer. It increases the local heat flux at the region directly above the wire. As the Reynolds number increases, the strength of the recirculating cell decreases and the perturbation of thermal boundary layer by the corona wind is suppressed.

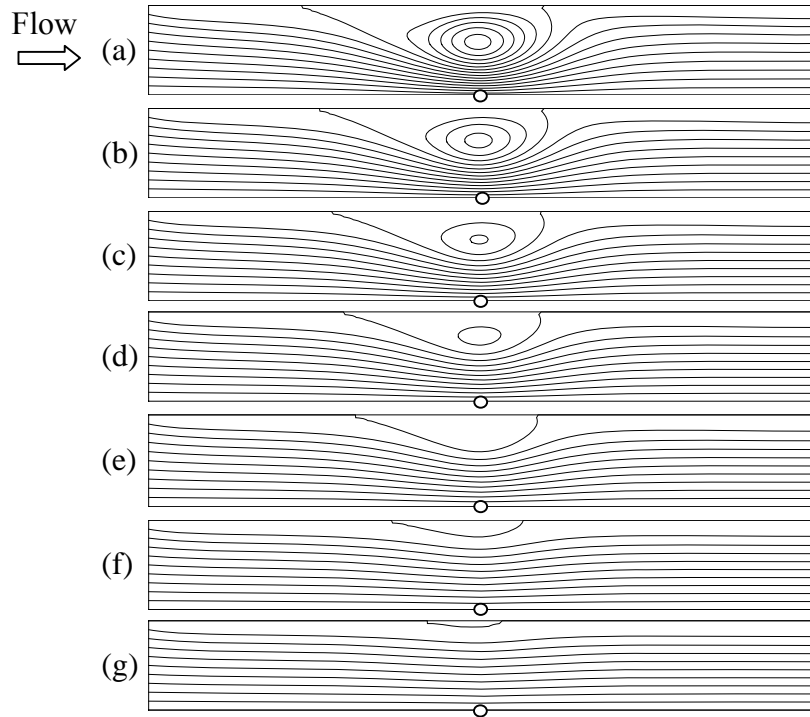


Figure 2.3 Flow fields predicted by one-way coupling model for $V_0 = 15$ kV

- (a) $Re = 600$, $\Psi_{\max} = 1.3$, $\Psi_{\min} = 0.5$, $\Delta\Psi = 0.05$
- (b) $Re = 750$, $\Psi_{\max} = 1.2$, $\Psi_{\min} = 0.5$, $\Delta\Psi = 0.05$
- (c) $Re = 900$, $\Psi_{\max} = 1.1$, $\Psi_{\min} = 0.5$, $\Delta\Psi = 0.05$
- (d) $Re = 1050$, $\Psi_{\max} = 1.1$, $\Psi_{\min} = 0.5$, $\Delta\Psi = 0.05$
- (e) $Re = 1200$, $\Psi_{\max} = 1.0$, $\Psi_{\min} = 0.5$, $\Delta\Psi = 0.05$
- (f) $Re = 1800$, $\Psi_{\max} = 1.0$, $\Psi_{\min} = 0.5$, $\Delta\Psi = 0.05$
- (g) $Re = 2400$, $\Psi_{\max} = 1.0$, $\Psi_{\min} = 0.5$, $\Delta\Psi = 0.05$

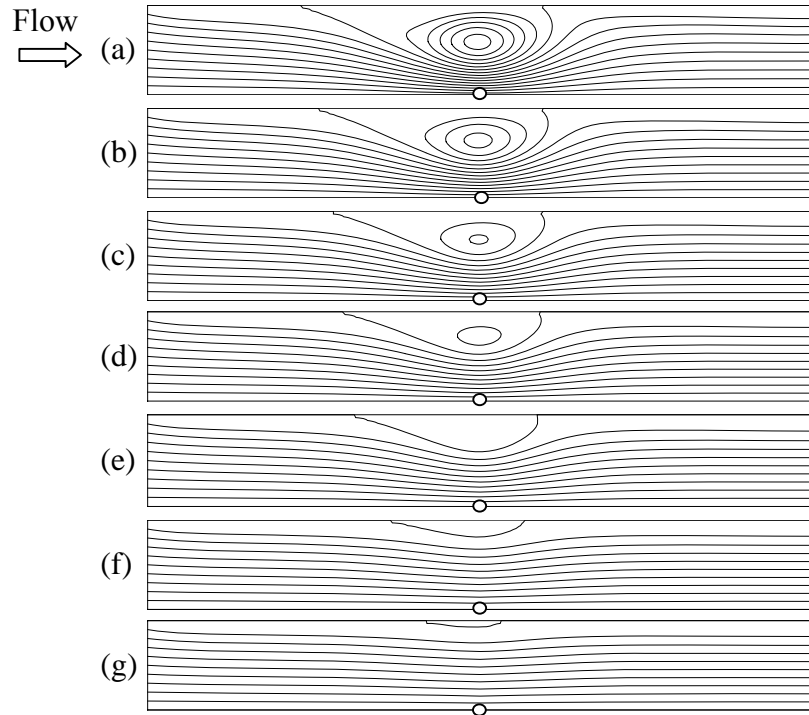


Figure 2.4 Flow fields predicted by two-way coupling model for $V_0 = 15$ kV

- (a) $Re = 600$, $\Psi_{\max} = 1.3$, $\Psi_{\min} = 0.5$, $\Delta\Psi = 0.05$
- (b) $Re = 750$, $\Psi_{\max} = 1.2$, $\Psi_{\min} = 0.5$, $\Delta\Psi = 0.05$
- (c) $Re = 900$, $\Psi_{\max} = 1.1$, $\Psi_{\min} = 0.5$, $\Delta\Psi = 0.05$
- (d) $Re = 1050$, $\Psi_{\max} = 1.1$, $\Psi_{\min} = 0.5$, $\Delta\Psi = 0.05$
- (e) $Re = 1200$, $\Psi_{\max} = 1.0$, $\Psi_{\min} = 0.5$, $\Delta\Psi = 0.05$
- (f) $Re = 1800$, $\Psi_{\max} = 1.0$, $\Psi_{\min} = 0.5$, $\Delta\Psi = 0.05$
- (g) $Re = 2400$, $\Psi_{\max} = 1.0$, $\Psi_{\min} = 0.5$, $\Delta\Psi = 0.05$

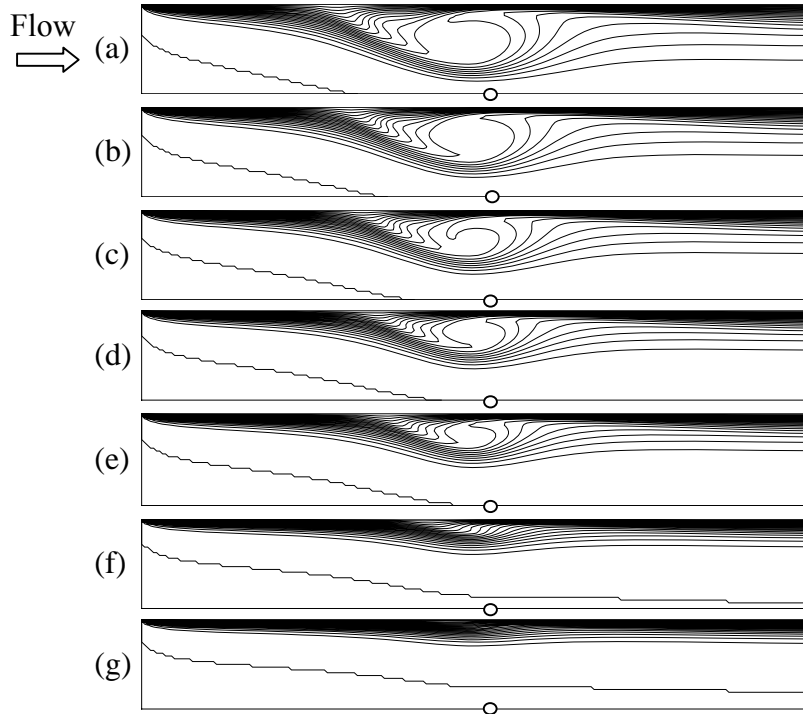


Figure 2.5 Temperature fields predicted by one-way coupling model for $V_0 = 15$ kV

- (a) $Re = 600$, $\theta_{\max} = 1.0$, $\theta_{\min} = 0.0$, $\Delta\theta = 0.05$
- (b) $Re = 750$, $\theta_{\max} = 1.0$, $\theta_{\min} = 0.0$, $\Delta\theta = 0.05$
- (c) $Re = 900$, $\theta_{\max} = 1.0$, $\theta_{\min} = 0.0$, $\Delta\theta = 0.05$
- (d) $Re = 1050$, $\theta_{\max} = 1.0$, $\theta_{\min} = 0.0$, $\Delta\theta = 0.05$
- (e) $Re = 1200$, $\theta_{\max} = 1.0$, $\theta_{\min} = 0.0$, $\Delta\theta = 0.05$
- (f) $Re = 1800$, $\theta_{\max} = 1.0$, $\theta_{\min} = 0.0$, $\Delta\theta = 0.05$
- (g) $Re = 2400$, $\theta_{\max} = 1.0$, $\theta_{\min} = 0.0$, $\Delta\theta = 0.05$

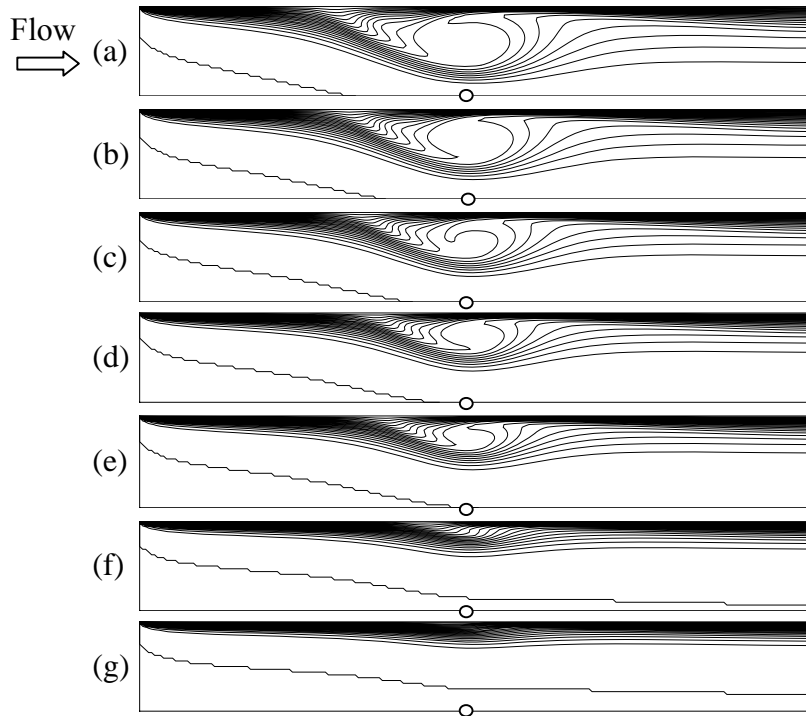


Figure 2.6 Temperature fields predicted by two-way coupling model for $V_0 = 15$ kV

- (a) $Re = 600$, $\theta_{max} = 1.0$, $\theta_{min} = 0.0$, $\Delta\theta = 0.05$
- (b) $Re = 750$, $\theta_{max} = 1.0$, $\theta_{min} = 0.0$, $\Delta\theta = 0.05$
- (c) $Re = 900$, $\theta_{max} = 1.0$, $\theta_{min} = 0.0$, $\Delta\theta = 0.05$
- (d) $Re = 1050$, $\theta_{max} = 1.0$, $\theta_{min} = 0.0$, $\Delta\theta = 0.05$
- (e) $Re = 1200$, $\theta_{max} = 1.0$, $\theta_{min} = 0.0$, $\Delta\theta = 0.05$
- (f) $Re = 1800$, $\theta_{max} = 1.0$, $\theta_{min} = 0.0$, $\Delta\theta = 0.05$
- (h) $Re = 2400$, $\theta_{max} = 1.0$, $\theta_{min} = 0.0$, $\Delta\theta = 0.05$

When the flow and temperature fields become oscillatory, which usually occurs at a low Reynolds number and a high applied voltage (for example, $V_0 = 15.0$ kV, and $Re = 150$ to 450), the results obtained from one-way and two-way coupling are still quite similar, but there exist some slight differences between them. Figures 2.7 – 2.10 show the variation of flow and temperature fields through a complete cycle of oscillation. For this particular case, $V_0 = 15$ kV and $Re = 450$ ($u_i = 0.2277$ m/s), one notices that there is a small difference in the oscillating period despite the similarity in the flow and temperature profiles (Table 2.5). Nevertheless, both results have captured the nature of the flow oscillation. When no flow is introduced to the channel, the flow field is induced by the electric field alone and remains stable. Four recirculating cells produced by the corona wind locate symmetrically about the center of the channel. When an external flow is introduced to the channel, the symmetry of corona-induced flow is destroyed. As a result, one can clearly observe the regeneration and destruction of the secondary cells in the flow field, which in turn produces a wave-like isotherm pattern in the temperature field. The periods of oscillation as predicted by one-way and two-way coupling are mostly the same (Table 2.5). For the cases in which they are different, the difference is usually small (less than 0.1 dimensionless time).

The reason why the prediction of flow and temperature fields using one-way and two-way coupling agrees so well is attributed to the small change of the electric field by the bulk airflow. For the range of inlet velocities considered in the present study, it is found that the modification of electric field by airflow is quite negligible. To produce a noticeable change in the electric field by convective air, one needs to increase the inlet velocity substantially (for example, $u_i = 5$ m/s, which is about four times the maximum

velocity considered in the present study). From Figure 2.11, it is clear that most changes in the electric potential and charge density take place at a location far away from the wire. Also, the magnitude of these changes is observed to be proportional to the distance from the wire. The charge density at the wire is found to be $9.62 \times 10^{-4} \text{ C/m}^3$ when one-way coupling approach is used while it is $9.71 \times 10^{-4} \text{ C/m}^3$ when two-way coupling approach is applied. The ion velocity is found to vary from -160 to 160 m/s , which is more than 30 times faster than the inlet air velocity. As a result, the modification of the electric field by convective air is minimal. However, it is interesting to observe that the electric field also becomes oscillatory when the flow and temperature fields are oscillatory, which cannot be revealed using the one-way approach.

The relative magnitude of flow inertia and electric body force can be quantified by the EHD number, which is defined below.

$$N_{\text{EHD}} = \frac{HI}{b\rho u_i^2 A}. \quad (2.52)$$

Table 2.5 Period of the oscillatory flow in EHD-enhanced forced convection

Re	Applied Voltage (kV)	Dimensionless Period	
		One-way Coupling	Two-way Coupling
150	10	2.0	2.0
300	12.5	2.2	2.2
150	15	2.0	2.0
300	15	3.4	3.4
450	15	2.4	2.3
150	17.5	1.7	1.6
300	17.5	3.0	2.9
450	17.5	2.0	1.9
600	17.5	2.3	2.4
750	17.5	3.0	3.0

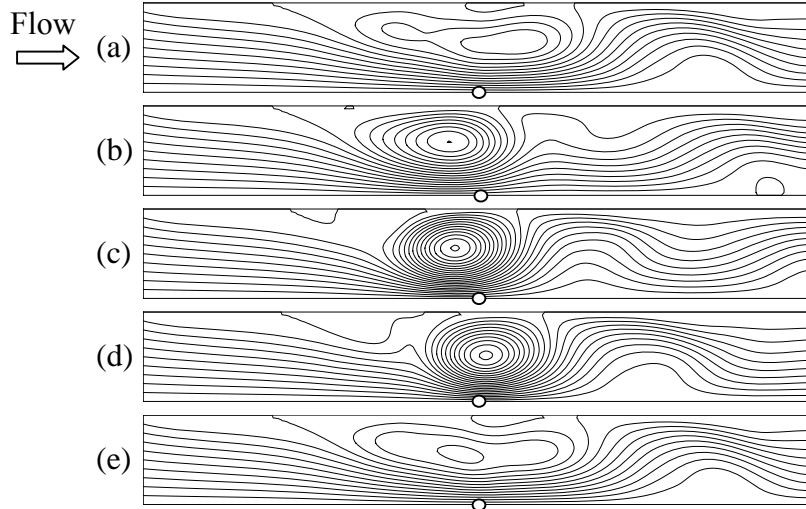


Figure 2.7 Flow fields at $V_0 = 15$ kV and $Re = 450$ (one-way coupling model)

- (a) $\tau = 55.8$, $\Psi_{\max} = 1.4$, $\Psi_{\min} = 0.0$, $\Delta\Psi = 0.2$
- (b) $\tau = 56.4$, $\Psi_{\max} = 1.8$, $\Psi_{\min} = 0.0$, $\Delta\Psi = 0.2$
- (c) $\tau = 57.0$, $\Psi_{\max} = 2.2$, $\Psi_{\min} = 0.0$, $\Delta\Psi = 0.2$
- (d) $\tau = 57.6$, $\Psi_{\max} = 2.0$, $\Psi_{\min} = 0.0$, $\Delta\Psi = 0.2$
- (e) $\tau = 58.2$, $\Psi_{\max} = 1.4$, $\Psi_{\min} = 0.0$, $\Delta\Psi = 0.2$

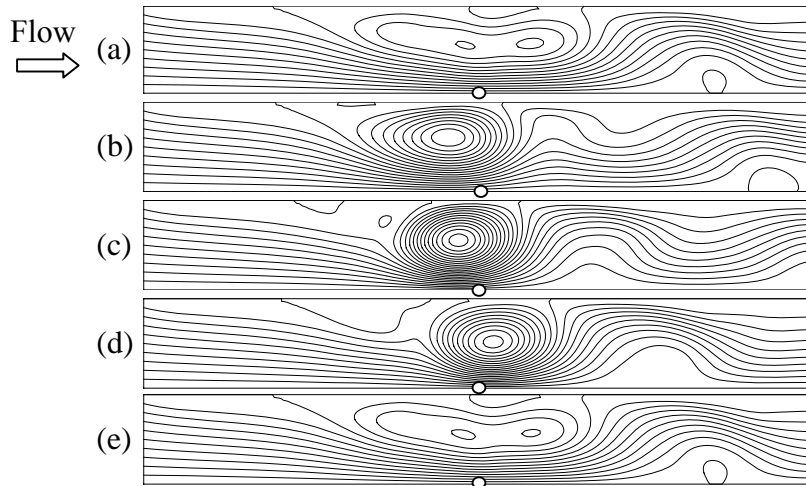


Figure 2.8 Flow fields at $V_0 = 15$ kV and $Re = 450$ (two-way coupling model)

- (a) $\tau = 57.9$, $\Psi_{\max} = 1.4$, $\Psi_{\min} = 0.0$, $\Delta\Psi = 0.2$
- (b) $\tau = 58.5$, $\Psi_{\max} = 1.9$, $\Psi_{\min} = 0.0$, $\Delta\Psi = 0.2$
- (c) $\tau = 59.1$, $\Psi_{\max} = 2.3$, $\Psi_{\min} = 0.0$, $\Delta\Psi = 0.2$
- (d) $\tau = 59.7$, $\Psi_{\max} = 2.0$, $\Psi_{\min} = 0.0$, $\Delta\Psi = 0.2$
- (e) $\tau = 60.2$, $\Psi_{\max} = 1.4$, $\Psi_{\min} = 0.0$, $\Delta\Psi = 0.2$

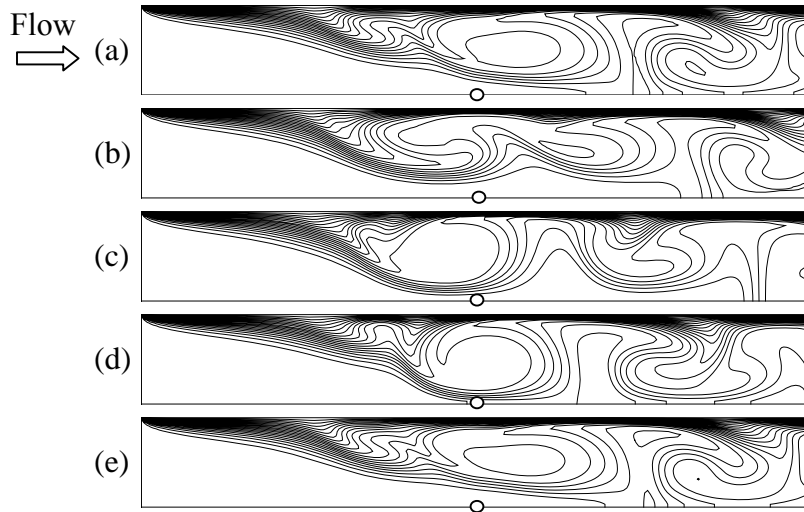


Figure 2.9 Temperature fields at $V_0 = 15$ kV and $Re = 450$ (one-way coupling model)

- (a) $\tau = 55.8$, $\theta_{\max} = 1.0$, $\theta_{\min} = 0.0$, $\Delta\theta = 0.1$
- (b) $\tau = 56.4$, $\theta_{\max} = 1.0$, $\theta_{\min} = 0.0$, $\Delta\theta = 0.1$
- (c) $\tau = 57.0$, $\theta_{\max} = 1.0$, $\theta_{\min} = 0.0$, $\Delta\theta = 0.1$
- (d) $\tau = 57.6$, $\theta_{\max} = 1.0$, $\theta_{\min} = 0.0$, $\Delta\theta = 0.1$
- (e) $\tau = 58.2$, $\theta_{\max} = 1.0$, $\theta_{\min} = 0.0$, $\Delta\theta = 0.1$

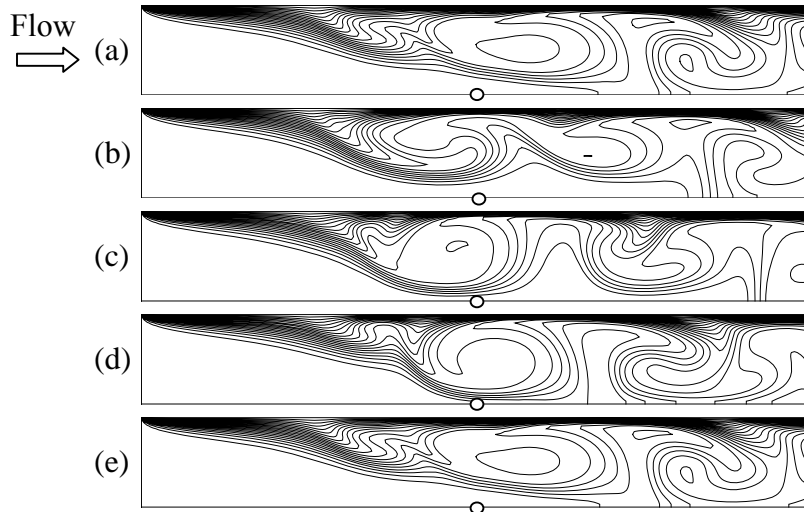


Figure 2.10 Temperature fields at $V_0 = 15$ kV and $Re = 450$ (two-way coupling model)

- (a) $\tau = 57.9$, $\theta_{\max} = 1.0$, $\theta_{\min} = 0.0$, $\Delta\theta = 0.1$
- (b) $\tau = 58.5$, $\theta_{\max} = 1.0$, $\theta_{\min} = 0.0$, $\Delta\theta = 0.1$
- (c) $\tau = 59.1$, $\theta_{\max} = 1.0$, $\theta_{\min} = 0.0$, $\Delta\theta = 0.1$
- (d) $\tau = 59.7$, $\theta_{\max} = 1.0$, $\theta_{\min} = 0.0$, $\Delta\theta = 0.1$
- (e) $\tau = 60.2$, $\theta_{\max} = 1.0$, $\theta_{\min} = 0.0$, $\Delta\theta = 0.1$

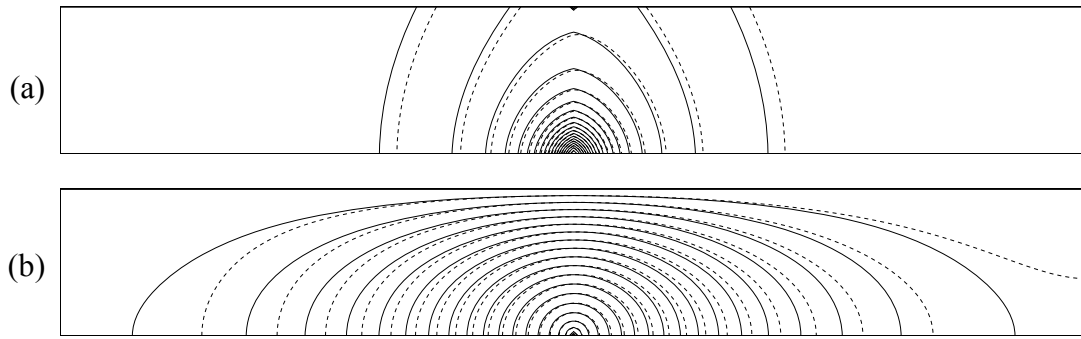


Figure 2.11 Modification of the electric field by air flow, $V_0 = 15$ kV and $u_i = 5$ m/s
 (a) charge density, (b) electric potential. (one-way – solid line, two-way – dashed line)

It is the ratio of the electric body force to inertial force and is expressed in terms of the measurable quantities [35]. When its value is zero, it represents pure forced convection. When its value approaches infinity, it becomes the corona wind dominated flow.

For the present study, the heat transfer enhancement is defined as the ratio of the Nusselt number resulting from the electric field to that without the electric field. The heat transfer enhancement is shown in Figure 2.12 as a function of the EHD number. For oscillatory flows, the time-averaged Nusselt numbers along with its maximum and minimum values are presented. As observed, oscillatory flows usually occur at a large EHD number (i.e., a low Reynolds number at a given electric field) and normally lead to a higher heat transfer enhancement. For oscillatory flows, the average Nusselt numbers predicted by both approaches are nearly the same. But, there are some slight differences in the maximum and minimum values. From the figure, one also observes that heat transfer enhancement increases with the applied voltage and is negligible when the EHD Number is less than 0.1. The maximum heat transfer enhancement can be as high as 3.5 times of that with out electric field.

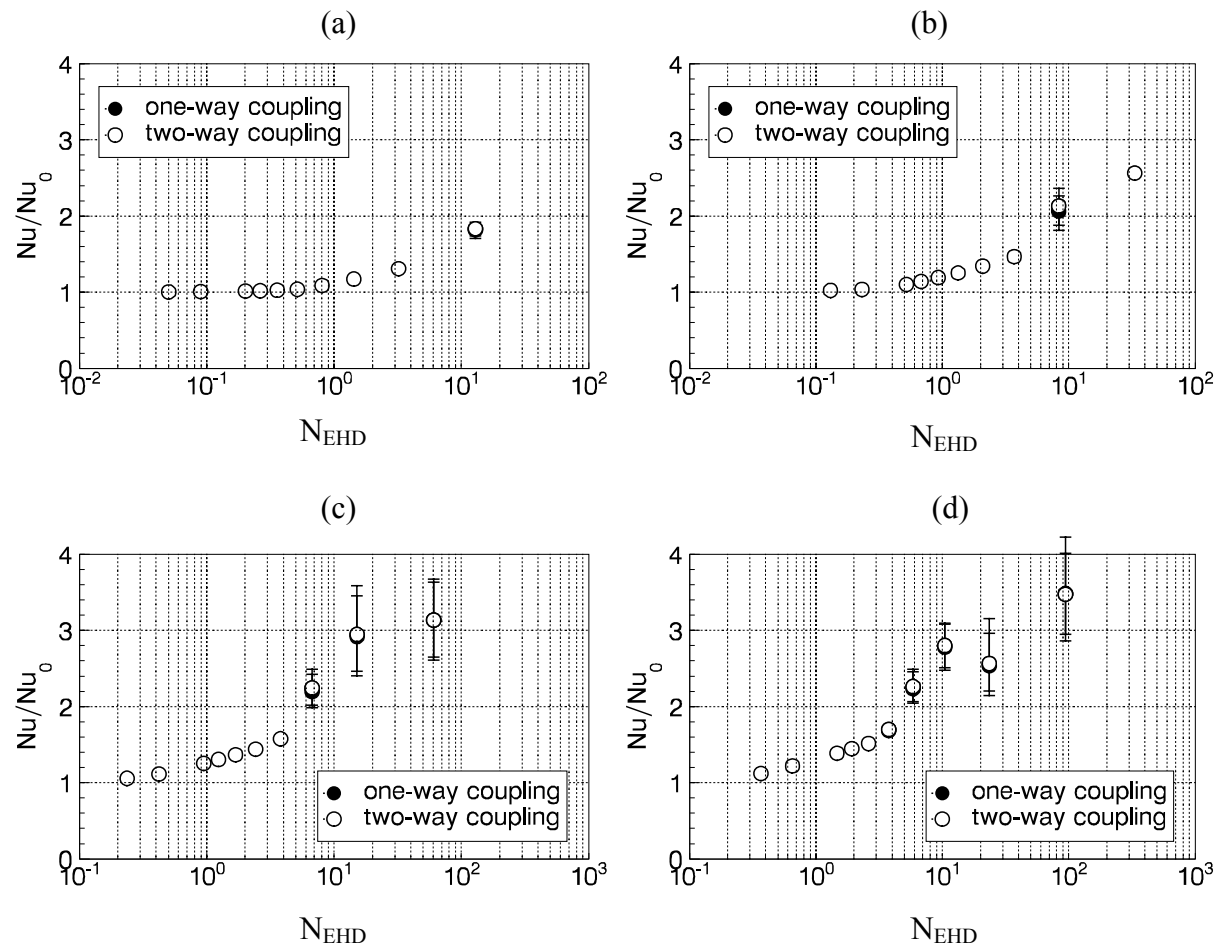


Figure 2.12 Heat transfer enhancement as a function of EHD number
 (a) $V_0 = 10.0$ kV, (b) $V_0 = 12.5$ kV, (c) $V_0 = 15.0$ kV, (d) $V_0 = 17.5$ kV.

2.3 EHD-enhanced Natural Convection with Joule Heating

The objective of this study is to evaluate the effect of Joule heating on the heat transfer enhancement in natural convection with the presence of electric field. For the present study, the electric field is established by charging a high, positive voltage to a wire electrode located at the mid-plane of the enclosure. The geometry considered is a two-dimensional cavity filled with air and with an aspect ratio of 5 (Figure 2.13). The two vertical walls are maintained at uniform temperatures, T_h and T_c ($T_h > T_c$), respectively. The top and bottom walls are electrically and thermally insulated. A wire electrode charged with a DC high voltage is placed in the enclosure at three different locations (1, 2, and 3 in Figure 2.13). Three voltages (12, 15, and 18 kV) are applied to the wire to create the electric field. A uniform grid (501×101) has been shown to produce satisfactory results [8]. A time step of 5×10^{-4} was shown to be adequate and was used in the present calculations [8].

The electric field is governed by equations (2.5) and (2.6). Their finite difference forms are given by equations (2.10) and (2.12). The results presented in the last section have verified that flow field has little effect on the electric field. That is, the assumption of one-way coupling is valid for most numerical analyses. Therefore, for the present study, only the influence of the electric field on the flow field is considered and not vice versa. That is, the velocity term in equations (2.6) and (2.12) is not considered. The corresponding boundary conditions for the electric field are

$$V = V_0. \quad \text{at the wire} \quad (2.53a)$$

$$V = 0. \quad \text{along the grounded walls} \quad (2.53b)$$

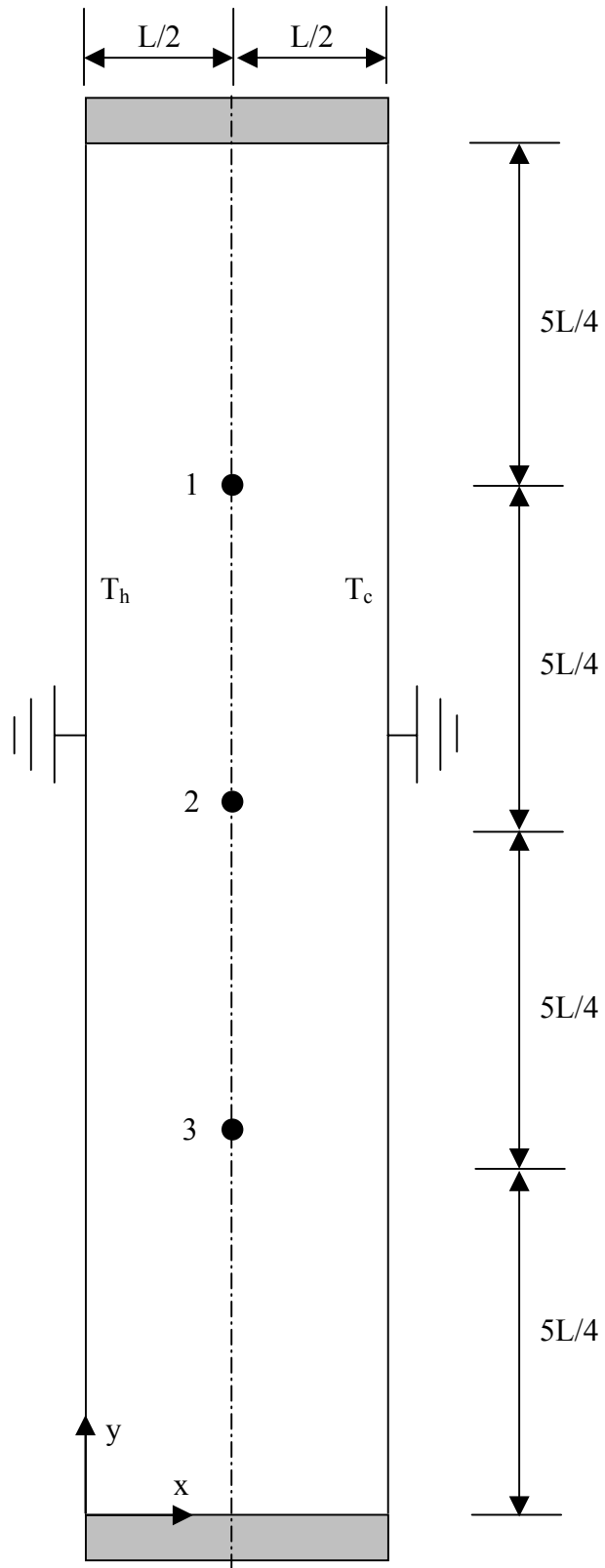


Figure 2.13 Wire positions in the two-dimensional enclosure ($L = 4$ inches)

$$\frac{\partial V}{\partial x} = 0. \quad \text{along the insulated walls} \quad (2.53c)$$

The corona currents used in this numerical study are measured in experiments reported by Tan and Lai [8], which are shown in Table 2.6.

2.3.1 Heat Generation for a Wire-plate System

The schematic diagram for a wire-plate system is shown as Figure 2.14. Heat generated by the electric field in this system includes Ohm heating and Joule heating.

Ohm heating is due to the current flowing in the wire. It can be determined by

$$Q_{\text{Ohm}} = RI^2 / L_p A_{\text{wire}} \quad (2.54)$$

where I is the current passing through the wire, L_p is the length of the wire, A_{wire} is the cross-sectional area of the wire, and R is the electrical resistance of the wire. In experiments reported by Tan and Lai [8], the copper wire has a diameter of 0.5 mm and a length of 10 inches. The electrical resistance can be determined as

$$R = \rho_e \frac{L_p}{A_{\text{wire}}} = \frac{1}{5.85(10)^7} \frac{(10)(0.0254)}{\frac{\pi}{4}(0.0005)^2} = 0.022 \Omega \quad (2.55)$$

where ρ_e is the electrical resistivity of copper, $\rho_e = 1/(5.85(10^7)) \Omega \text{ m}$.

Table 2.6 Corona currents produced by various wire locations in the enclosure studied [8]

Wire Position	Voltage (kV)	Current (A)
2	12	1.40×10^{-6}
	15	2.74×10^{-5}
	18	7.96×10^{-5}
1, 3	12	1.45×10^{-5}
	15	2.85×10^{-5}
	18	8.19×10^{-5}

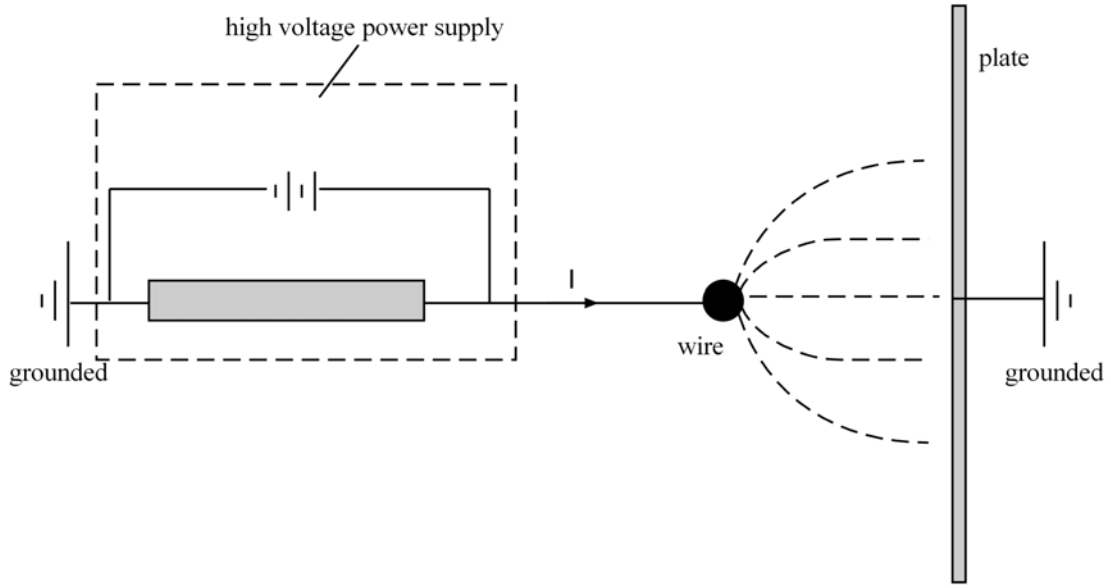


Figure 2.14 Electric diagram for a wire-plate system

Ohm heating is very small due to the small current and electrical resistance. For example, when $V_0 = 15$ kV, the current measured in the experiment [8] is $I = 2.74 \times 10^{-5}$ A, and the heat generation by the ohm heating from the wire is given by

$$Q_{\text{Ohm}} = \frac{0.022(2.74 \times 10^{-5})^2}{(10)(0.0254) \frac{\pi}{4} (0.0005)^2} = 3.33 \times 10^{-4} \text{ J/m}^3. \quad (2.56)$$

The existence of space charges in the electric field contributes the Joule heating. Due to the distribution of electric potential, Joule heating is produced very close to the wire. Joule heating is given as $b|\rho_c|E^2$ [36]. It needs to be considered when high current densities are present. For example, when $V_0 = 15$ kV, the heat generation by Joule heating in the electric field is calculated to be

$$Q_{\text{Joule}} = \sum \frac{b|\rho_c|E^2}{\rho c_p} = 1157.5 \text{ J/m}^3. \quad (2.57)$$

Clearly, Ohm heating can be neglected in this study because it is very small as compared with the Joule heating.

2.3.2 Governing Equations for Flow and Temperature Fields

The governing equations for the flow and temperature fields for the problem considered are the continuity equation, the Navier-Stokes equations in x and y directions, and the energy equation.

$$\frac{\partial u}{\partial x} + \frac{\partial v}{\partial y} = 0, \quad (2.58)$$

$$\frac{\partial u}{\partial t} + u \frac{\partial u}{\partial x} + v \frac{\partial u}{\partial y} = -\frac{1}{\rho} \frac{\partial p}{\partial x} + \nu \left(\frac{\partial^2 u}{\partial x^2} + \frac{\partial^2 u}{\partial y^2} \right) - \frac{\rho_c}{\rho} \frac{\partial V}{\partial x}, \quad (2.59)$$

$$\frac{\partial v}{\partial t} + u \frac{\partial v}{\partial x} + v \frac{\partial v}{\partial y} = -\frac{1}{\rho} \frac{\partial p}{\partial y} + \nu \left(\frac{\partial^2 v}{\partial x^2} + \frac{\partial^2 v}{\partial y^2} \right) + g\beta(T - T_c) - \frac{\rho_c}{\rho} \frac{\partial V}{\partial y}, \quad (2.60)$$

$$\frac{\partial T}{\partial t} + u \frac{\partial T}{\partial x} + v \frac{\partial T}{\partial y} = \alpha \left(\frac{\partial^2 T}{\partial x^2} + \frac{\partial^2 T}{\partial y^2} \right) + \frac{b\rho_c}{\rho c_p} \left(\left(\frac{\partial V}{\partial x} \right)^2 + \left(\frac{\partial V}{\partial y} \right)^2 \right). \quad (2.61)$$

The last term in the momentum equations (2.59) and (2.60) represents the electric body force while the third term on the right hand side of equation (2.60) is the thermal buoyancy. The existence of space charges in the fluid contributes the Joule heating, which is the last term in the energy equation (2.61). The governing equations can be non-dimensionalized by introducing the following dimensionless variables.

$$\begin{aligned} X &= \frac{x}{L}, & Y &= \frac{y}{L}, & \theta &= \frac{T - T_c}{T_h - T_c}, & \tau &= \frac{u_e t}{L}, & Pr &= \frac{\nu}{\alpha}, \\ U &= \frac{u}{u_e}, & V &= \frac{v}{u_e}, & \Omega &= \frac{\omega L}{u_e}, & \bar{V} &= \frac{V}{V_0}, & \bar{\rho}_c &= \frac{\rho_c}{\rho_{c0}}, \\ u_e &= \sqrt{\frac{\rho_{c0} V_0}{\rho}}, & U &= \frac{\partial \Psi}{\partial Y}, & V &= -\frac{\partial \Psi}{\partial X}, & Re_{EHD} &= \frac{u_e L}{\nu}. \end{aligned} \quad (2.62)$$

The above governing equations can be expressed in the dimensionless form in terms of the stream function and vorticity, and they are given by

$$\frac{\partial^2 \psi}{\partial X^2} + \frac{\partial^2 \psi}{\partial Y^2} = -\Omega, \quad (2.63)$$

$$\frac{\partial \Omega}{\partial \tau} + \frac{\partial \psi}{\partial Y} \frac{\partial \Omega}{\partial X} - \frac{\partial \psi}{\partial X} \frac{\partial \Omega}{\partial Y} = \frac{1}{\text{Re}_{\text{EHD}}} \left(\frac{\partial^2 \Omega}{\partial X^2} + \frac{\partial^2 \Omega}{\partial Y^2} \right) + \frac{\text{Ra Pr}}{\text{Pe}_{\text{EHD}}^2} \frac{\partial \theta}{\partial X} + \left(\frac{\partial \bar{V}}{\partial Y} \frac{\partial \bar{\rho}_c}{\partial X} - \frac{\partial \bar{V}}{\partial X} \frac{\partial \bar{\rho}_c}{\partial Y} \right), \quad (2.64)$$

$$\frac{\partial \theta}{\partial \tau} + \frac{\partial \psi}{\partial Y} \frac{\partial \theta}{\partial X} - \frac{\partial \psi}{\partial X} \frac{\partial \theta}{\partial Y} = \frac{1}{\text{Pe}_{\text{EHD}}} \left(\frac{\partial^2 \theta}{\partial X^2} + \frac{\partial^2 \theta}{\partial Y^2} \right) + \frac{b \rho_c V_0^2}{\rho c_p u_e L (T_h - T_c)} \left(\left(\frac{\partial \bar{V}}{\partial X} \right)^2 + \left(\frac{\partial \bar{V}}{\partial Y} \right)^2 \right). \quad (2.65)$$

The finite difference form of these governing equations can be obtained using the same approach outlined in the previous section, and the numerical procedures are also the same.

The corresponding boundary conditions for the flow and temperature fields are

$$X = 0, \quad \Omega = -\frac{\partial^2 \psi}{\partial X^2}, \quad \psi = 0, \quad \theta = 1. \quad (2.66a)$$

$$X = 1, \quad \Omega = -\frac{\partial^2 \psi}{\partial X^2}, \quad \psi = 0, \quad \theta = 0. \quad (2.66b)$$

$$Y = 0, \quad \Omega = -\frac{\partial^2 \psi}{\partial Y^2}, \quad \psi = 0, \quad \frac{\partial \theta}{\partial Y} = 0. \quad (2.66c)$$

$$Y = 5, \quad \Omega = -\frac{\partial^2 \psi}{\partial Y^2}, \quad \psi = 0, \quad \frac{\partial \theta}{\partial Y} = 0. \quad (2.66d)$$

2.3.3 Evaluation of Heat Transfer Results

To evaluate the heat transfer rate, the local heat transfer coefficient is expressed in terms of the local Nusselt number (Nu_x).

$$Nu_x = -\left(\frac{\partial\theta}{\partial X}\right)_{X=0,1}. \quad (2.67)$$

The average Nusselt number can then be determined from the local heat transfer coefficient by

$$Nu = \frac{1}{5} \int_0^5 Nu_x dY. \quad (2.68)$$

For periodic flows, the time-averaged Nusselt number is calculated by averaging the Nusselt number over a period of oscillation using equation (2.47). For non-periodic flows, the time-averaged Nusselt number is calculated by averaging the Nusselt number over a time span τ_1 using equation (2.48).

2.3.4 Code Validation

The numerical solutions begin with the calculation of the electric field. Then, the flow and temperature fields are solved simultaneously. The numerical code for the solutions of flow and temperature fields without electric field was validated against the correlation proposed by Berkovsky and Polevikov [37] for natural convection in a rectangular enclosure. The correlation proposed by them is given by

$$Nu_0 = 0.22 \left(\frac{5L}{L}\right)^{-0.25} \left(\frac{Pr}{0.2 + Pr} Ra\right)^{0.28}. \quad (2.69)$$

The Nusselt number obtained from the present study (Nu) and those from the above equation (Nu_0) for various Rayleigh number is listed in Table 2.7. The agreement between the results obtained from the correlation and those of present study is fairly good

Table 2.7 Comparison of Nusselt numbers obtained from correlation [37] and present study

Ra	Nu ₀	Nu	$\frac{ Nu - Nu_0 }{Nu} \times 100\%$
10 ⁴	1.809	2.023	10.57
10 ⁵	3.447	3.760	8.32
10 ⁶	6.569	6.681	1.68

in consideration of the uncertainty involved in the correlation itself.

2.3.5 Results and Discussion

Numerical solutions have been obtained for three wire positions (1, 2, and 3) and three applied voltages at the wire (12, 15, and 18 kV). Also, the Rayleigh number is varied from 10⁴, 10⁵ to 10⁶, for which the corresponding temperature differences between the two walls are in the order of 0.1, 1, and 10 °C, respectively. A Pentium 4 personal computer was used to perform this numerical simulation. It took 10.1 hours for calculations to advance 100 dimensionless time,. The same relative convergence criterion (as that in the previous study) was used in this simulation.

In general, the results obtained with the effects of Joule heating show the same trend as those without. That is, the heat transfer enhancement by electric field increases with the applied voltage, but decreases with the Rayleigh number. However, the two results differ quite significantly in their values, particularly at low Rayleigh numbers.

The present study shows that in many cases the flow and temperature fields become non-periodically oscillatory when Joule heating is included. For some cases, the flow and temperature fields may remain in the periodically oscillatory mode, but their profiles are very different from those without Joule heating. For example, this can be observed from the temperature fields shown in Figures 2.15 and 2.16 where the

temperature fields is going through one complete cycle (period) of oscillation. When Joule heating is neglected (Figure 2.16), the temperature field is only perturbed by the electric field near the wire location. The development of the thermal boundary layer is disrupted by the corona wind issued from the wire. When Joule heating is included (Figure 2.15), the temperature field is not only affected by the corona wind, but also by the thermal buoyancy produced from Joule heating. Although the added thermal energy from Joule heating is normally small, it is relatively large in comparison to the heat transferred between the walls when the Rayleigh number is small. As such, it produces additional thermal buoyancy from the wire. Since the distribution of space charge density is most concentrated near the wire, the effect of Joule heating is also most prominent at the wire (Figure 2.15). The combined effect of corona wind and added thermal buoyancy from Joule heating produces a very large temperature gradient at the cold wall directly opposite to the wire. From the observation above, one is certain that Joule heating can easily destabilize the flow and temperature fields at low Rayleigh numbers and leads to non-periodic oscillation. In contrast, the stability of flow and temperature fields is not affected by Joule heating when the Rayleigh number is large. This is evident from the periodic flows in which the period of oscillation is only modified slightly when Joule heating is included at a large Rayleigh number.

The differences in the flow and temperature fields obtained from these two approaches (with and without Joule heating) diminish when the Rayleigh number increases. These can be observed from Figures 2.17 and 2.18 when both flow and temperature fields become steady. The streamline contours show that the flow fields obtained from these two approaches are almost identical (Figure 2.17). For temperature

fields, the major difference appears only near the wire at $Ra = 10^5$ (Figure 2.18). This indicates that the thermal buoyancy produced by Joule heating becomes negligible when the Rayleigh number increases. The added thermal energy from Joule heating becomes only a small fraction of the energy transferred between the differentially heated walls when the Rayleigh number is greater than 10^5 , which corresponds to an equivalent temperature difference on the order of unity for the present study (i.e., $\Delta T = O(1)$).

To evaluate the heat transfer enhancement by electric field, the Nusselt numbers obtained are compared with those of pure natural convection and they are shown in Figures 2.19 and 2.20, respectively with and without Joule heating. Although both results show the same general trend that they increase with the applied voltage and decrease with the Rayleigh number, there is a large discrepancy in their values, particularly at a small Rayleigh number ($Ra = 10^4$). As discussed earlier, this is mainly due to the additional energy provided by the electric field through Joule heating. At this condition, the heat transfer enhancement cannot be totally credited to corona wind. The additional thermal buoyancy produced by Joule heating is mainly responsible for this dramatic increase in the heat transfer enhancement.

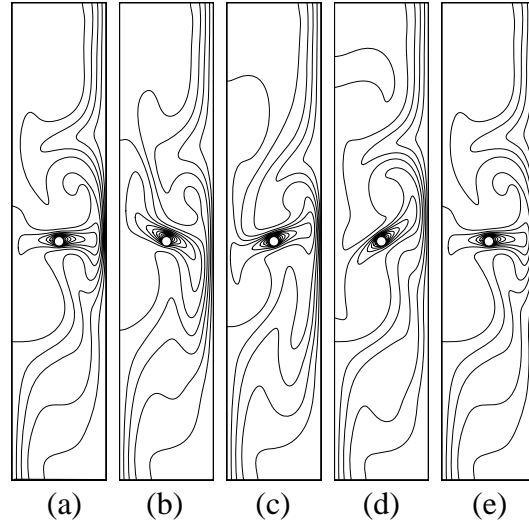


Figure 2.15 Temperature fields at the wire position 2

($V_0 = 12$ kV, $Ra = 10^4$, with Joule heating)

(a) $\tau = 656.1$, $\theta_{\max} = 1.0$, $\theta_{\min} = 0.0$, $\Delta\theta = 0.2$

(b) $\tau = 668.6$, $\theta_{\max} = 1.0$, $\theta_{\min} = 0.0$, $\Delta\theta = 0.2$

(c) $\tau = 681.1$, $\theta_{\max} = 1.0$, $\theta_{\min} = 0.0$, $\Delta\theta = 0.2$

(d) $\tau = 693.6$, $\theta_{\max} = 1.0$, $\theta_{\min} = 0.0$, $\Delta\theta = 0.2$

(e) $\tau = 705.8$, $\theta_{\max} = 1.0$, $\theta_{\min} = 0.0$, $\Delta\theta = 0.2$

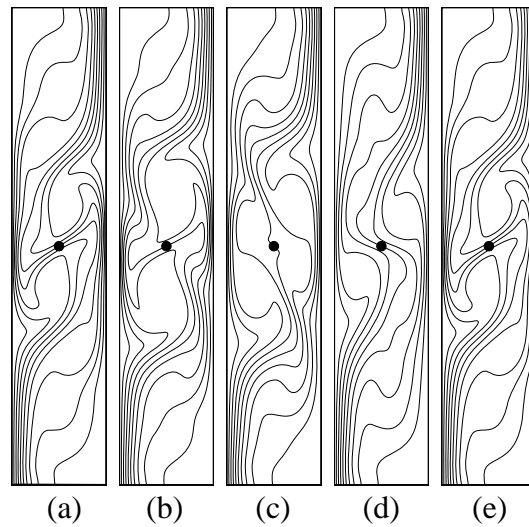


Figure 2.16 Temperature fields at the wire position 2

($V_0 = 12$ kV, $Ra = 10^4$, without Joule heating)

(a) $\tau = 611.9$, $\theta_{\max} = 1.0$, $\theta_{\min} = 0.0$, $\Delta\theta = 0.1$

(b) $\tau = 623.9$, $\theta_{\max} = 1.0$, $\theta_{\min} = 0.0$, $\Delta\theta = 0.1$

(c) $\tau = 635.9$, $\theta_{\max} = 1.0$, $\theta_{\min} = 0.0$, $\Delta\theta = 0.1$

(d) $\tau = 647.9$, $\theta_{\max} = 1.0$, $\theta_{\min} = 0.0$, $\Delta\theta = 0.1$

(e) $\tau = 660.9$, $\theta_{\max} = 1.0$, $\theta_{\min} = 0.0$, $\Delta\theta = 0.1$

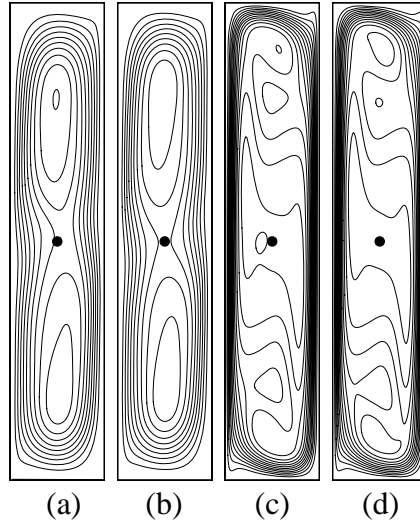


Figure 2.17 Flow fields at the wire position 2 ($V_0 = 12$ kV)

(a) $Ra = 10^5$, with Joule heating, $\Psi_{\max} = 0.0$, $\Psi_{\min} = -0.050$, $\Delta\Psi = 0.005$
 (b) $Ra = 10^5$, without Joule heating, $\Psi_{\max} = 0.0$, $\Psi_{\min} = -0.050$, $\Delta\Psi = 0.005$
 (c) $Ra = 10^6$, with Joule heating, $\Psi_{\max} = 0.0$, $\Psi_{\min} = -0.070$, $\Delta\Psi = 0.005$
 (d) $Ra = 10^6$, without Joule heating, $\Psi_{\max} = 0.0$, $\Psi_{\min} = -0.070$, $\Delta\Psi = 0.005$

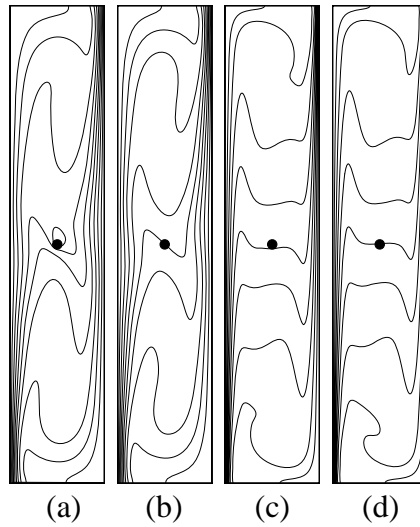
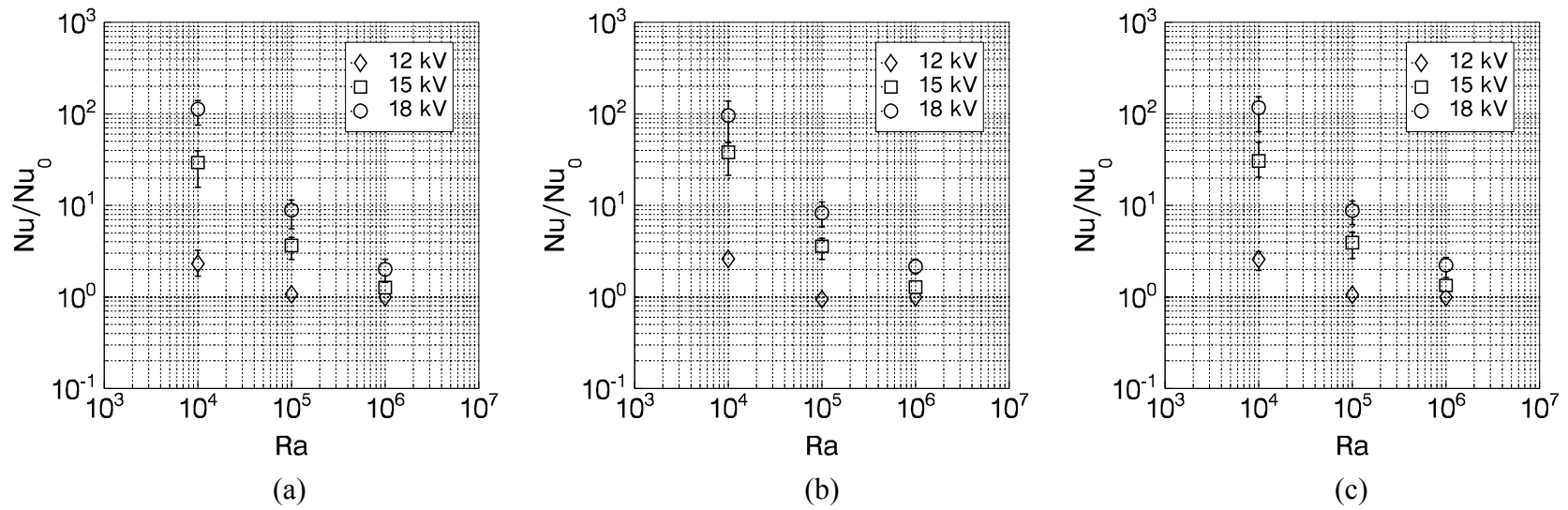


Figure 2.18 Temperature fields at the wire position 2 ($V_0 = 12$ kV)

(a) $Ra = 10^5$, with Joule heating, $\theta_{\max} = 1.0$, $\theta_{\min} = 0.0$, $\Delta\theta = 0.1$
 (b) $Ra = 10^5$, without Joule heating, $\theta_{\max} = 1.0$, $\theta_{\min} = 0.0$, $\Delta\theta = 0.1$
 (c) $Ra = 10^6$, with Joule heating, $\theta_{\max} = 1.0$, $\theta_{\min} = 0.0$, $\Delta\theta = 0.1$
 (d) $Ra = 10^6$, without Joule heating, $\theta_{\max} = 1.0$, $\theta_{\min} = 0.0$, $\Delta\theta = 0.1$



**Figure 2.19 Heat transfer enhancement with the effect of Joule heating
(a) position 1, (b) position 2, (c) position 3.**

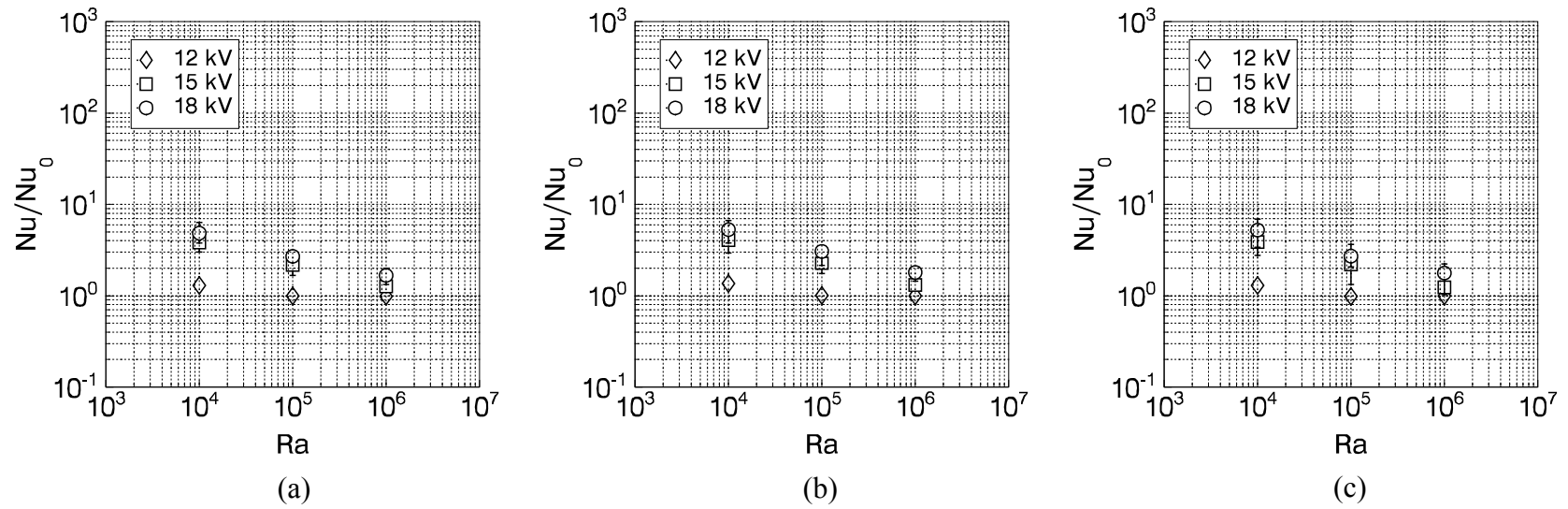


Figure 2.20 Heat transfer enhancement without the effect of Joule heating
 (a) position 1, (b) position 2, (c) position 3.

CHAPTER THREE

EHD-ENHANCED MASS TRANSFER

In this chapter, the study of EHD-enhanced water evaporation is presented. Experiments were first conducted to obtain a correlation between the evaporation rate and the electric conditions, then numerical simulation was followed and the results obtained from both approaches were compared.

3.1 Experiment Study

All experiments reported in this study were conducted in the Heat Transfer Laboratory at the University of Oklahoma.

3.1.1 Experiment Setup

A schematic diagram of the experimental setup is shown in Figure 3.1. A rectangular horizontal channel constructed using a half-inch-thick Plexiglas is used as the test section. It is seventy-two inches in length, five inches in height, and nine inches in width. A square opening with a width of six and half inches is located on the bottom wall of the test section, and it is fifty five inches away from the inlet of the channel, where a blower is attached to a converging nozzle to supply cross-flow in the test section. A stack of straws is placed in the inlet of the channel to help creating a uniform airflow in the test section. A copper wire with a diameter of 0.5 mm, suspended one inch above the channel bottom wall, is used as an emitting electrode to create the electric field in the channel. A high DC voltage is applied to the wire from a high voltage power supply.

Two containers, each with the dimensions of six inches in length, six inches in width and one and half inches in height, are used to hold water. The sidewalls of the

containers are made of Plexiglas while the bottom wall is made of copper plate. These containers are placed separately on top of two digital balances. One of the containers with a digital balance is placed underneath the wire in the test section. A digital multimeter is used to measure the corona current on the bottom plate of this container. Another container with a digital balance is exposed to ambient air. Both digital balances are connected to a personal computer and the drying rate in terms of the weight loss of water with time is monitored. Also, the ambient temperature and humidity in the laboratory are also monitored throughout the experiment by a temperature/humidity data logger.

3.1.2 Experimental Apparatus

The instruments and equipment used in the experiments include a blower, a high-voltage power supply, two digital balances, a temperature/humidity data logger, a van velocimeter, and a digital multimeter. Their functions and capabilities are described below.

Blower

A blower of type C, manufactured by Fasco, is used to supply airflow through the test channel. It is operated by electricity at 60 Hz and 0.6 Amp. The operating voltage is between 208 V and 230 V. This blower can deliver an air stream with a maximum velocity of 2.2 m/s.

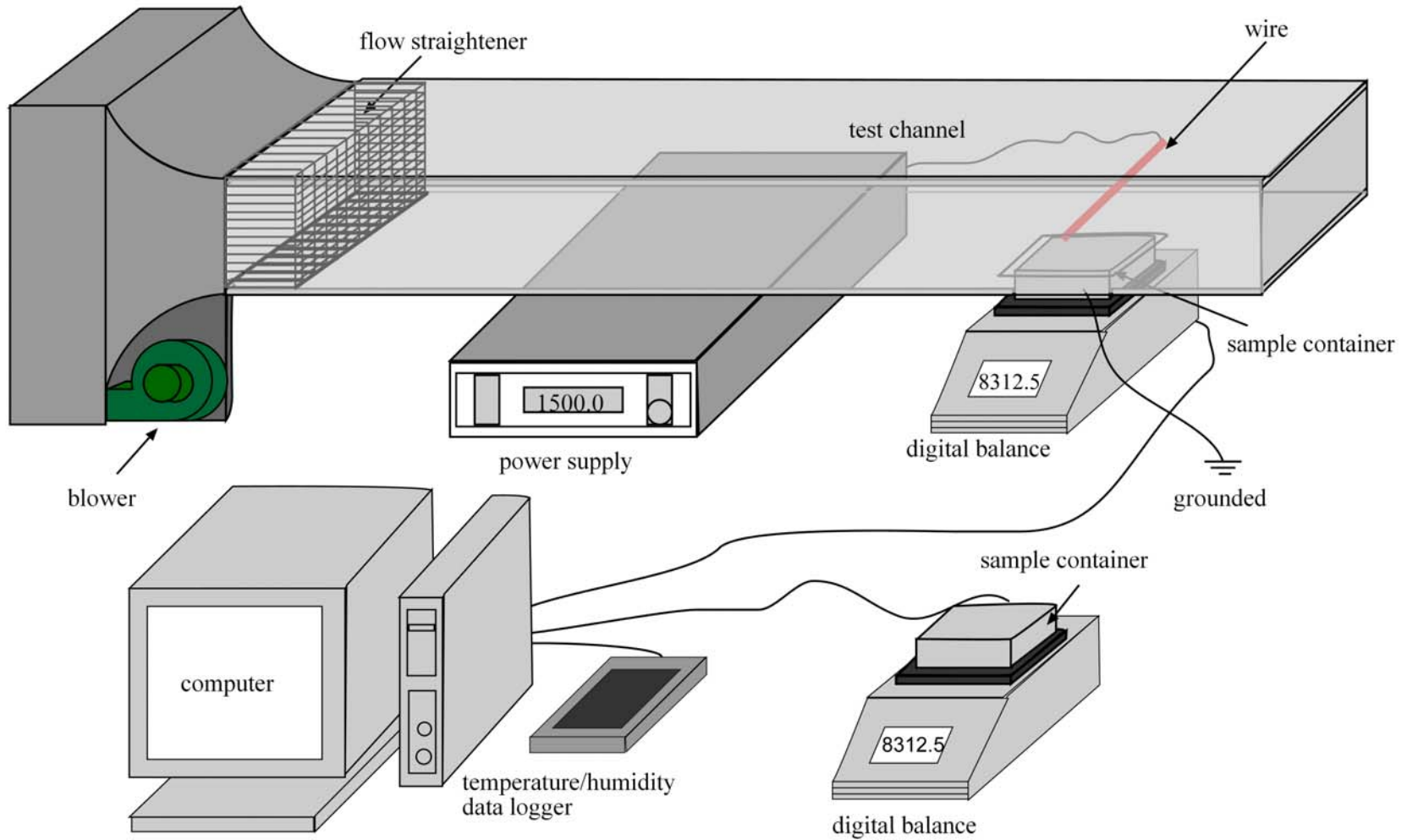


Figure 3.1 Experiment setup



Figure 3.2 Blower

High-Voltage Power Supply

The voltage applied to the wire electrode is provided by a high-voltage power supply manufactured by Bertan Associates, Inc. (Series 205B-30R). This power supply can provide voltage up to 30 kV and can operate on both polarities. The resolution of the power supply is 0.2% of maximum. The accuracy of the front panel meter is $\pm 0.1\%$ of reading + 0.1% of maximum for voltage, and $\pm 0.25\%$ of reading + 0.25% of maximum for current.

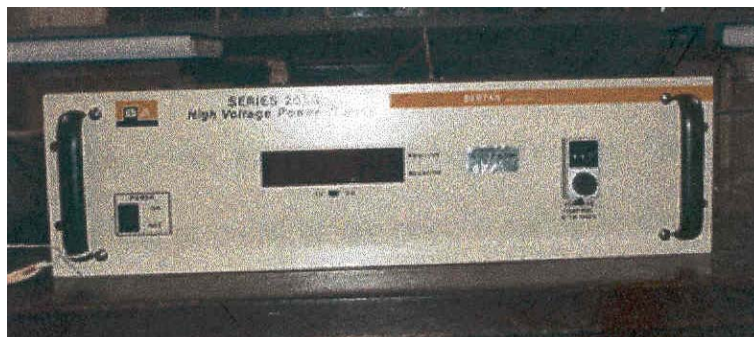


Figure 3.3 High-voltage power supply

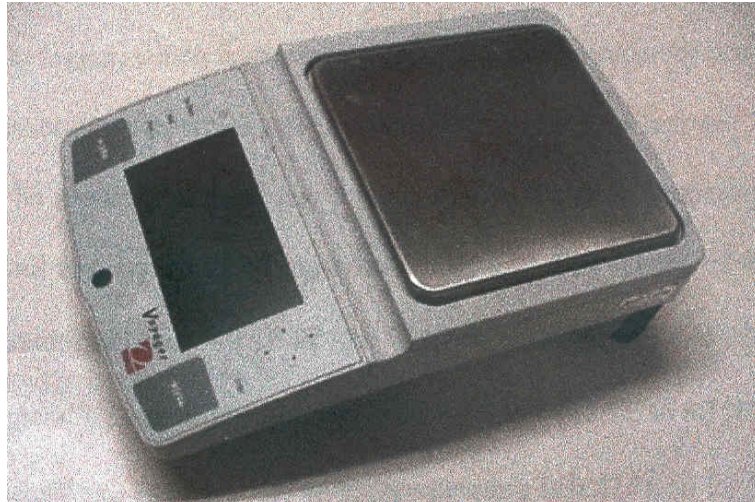


Figure 3.4 Digital balance

Digital Balance

Two digital balances manufactured by Ohaus (Voyager, V1RW60) have been used in the experiments to measure the weight loss of water from both containers. The capacity of these digital balances ranges from 1000 grams to 4100 grams and the readability in these ranges is 0.01 g and 0.1 g, respectively. The operating temperature is 10 °C to 50 °C. The balances are set up to communicate with a personal computer through HyperTerminal. HyperTerminal is used to collect and store the data recorded by the digital balances during the experiments.

Temperature/Humidity Data Logger

The temperature/humidity data logger manufactured by Dickson (D200) is a completely self-contained unit. It can measure both temperature and humidity with its internal sensors. The ranges of temperature and humidity measurement are - 40 °C – 80 °C, and 10% RH – 95% RH. The ambient operating temperature is - 40 °C – 80 °C, and the ambient operating humidity is 0 RH – 95% RH. The accuracy of the temperature

measurement is $0.15\text{ }^{\circ}\text{C}$ at $25\text{ }^{\circ}\text{C}$, and $0.25\text{ }^{\circ}\text{C}$ over the range of $-40\text{ }^{\circ}\text{C} - 70\text{ }^{\circ}\text{C}$. The accuracy of the humidity measurement is $\pm 2\%$ over the range of $10\% \text{ RH} - 95\% \text{ RH}$ at $25\text{ }^{\circ}\text{C}$ and is $\pm 4\%$ over the range of $10\% \text{ RH} - 95\% \text{ RH}$ at the temperature range of $-40\text{ }^{\circ}\text{C} - 80\text{ }^{\circ}\text{C}$. The data recorded by the logger is transferred to a personal computer using the software Dickson Wave provided by the manufacturer. Dickson Ware provides the distribution curves of temperature and humidity (Figure 3.6) as well as the statistical data such as average, maximum and minimum of the temperature and humidity over the measurement time period (Figure 3.7).



Figure 3.5 Temperature/Humidity data logger

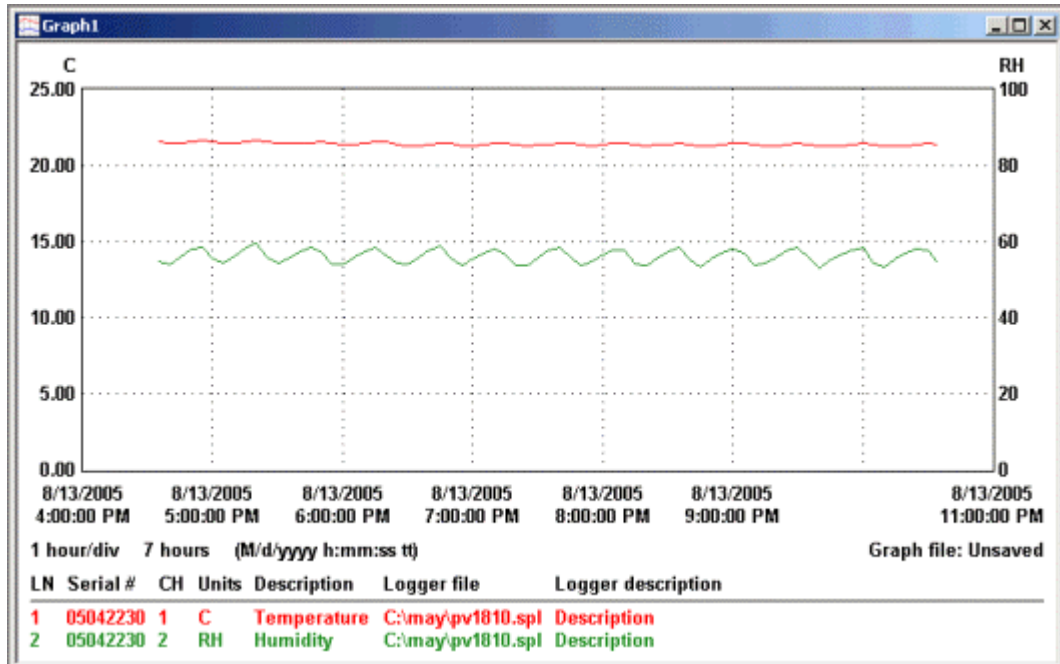


Figure 3.6 Variation of ambient temperature and humidity recorded by the data logger

	Channel 1 Temperature	Channel 2 Humidity
Description:		
Maximum Value:	21.66 C	59.8 RH
Average Value:	21.46 C	56.3 RH
Minimum Value:	21.33 C	53.3 RH
8/13/2005 4:35:00 PM	21.58 C	54.8 RH
8/13/2005 4:40:00 PM	21.50 C	54.2 RH
8/13/2005 4:45:00 PM	21.50 C	56.1 RH
8/13/2005 4:50:00 PM	21.58 C	58.4 RH
8/13/2005 4:55:00 PM	21.66 C	58.6 RH
8/13/2005 5:00:00 PM	21.58 C	55.6 RH
8/13/2005 5:05:00 PM	21.48 C	54.7 RH
8/13/2005 5:10:00 PM	21.48 C	56.3 RH
8/13/2005 5:15:00 PM	21.58 C	58.6 RH
8/13/2005 5:20:00 PM	21.66 C	59.8 RH
8/13/2005 5:25:00 PM	21.60 C	56.1 RH
8/13/2005 5:30:00 PM	21.48 C	54.5 RH
8/13/2005 5:35:00 PM	21.48 C	55.8 RH
8/13/2005 5:40:00 PM	21.48 C	57.6 RH
8/13/2005 5:45:00 PM	21.56 C	58.8 RH

Figure 3.7 Statistical data recorded by the data logger



Figure 3.8 Van velocimeter

Van Velocimeter

A van velocimeter is used to measure the airflow velocity at the outlet of the test section. This velocimeter has four measuring scales: mile per hour, meter per second, feet per minute, and knots. The range of measurement for each scale is 0 – 99.9 MPH, 0 – 44.8 m/s, 0 – 8790 FPM, and 0 – 97.9 knot, respectively. The accuracy of the measurement for each scale is ± 1 MPH, ± 1 m/s, \pm FPM and ± 1 knot, respectively.

3.1.3 Experiment Procedure

The experiments have been conducted using both positive and negative corona discharge. Various voltages (14 kV – 20 kV) have been applied in each polarity. The wire is held one inch above the water surface. The experiment procedure is listed below.

1. Digital balances are carefully calibrated to ensure their accuracy. One container is placed under the opening of the test section, on top of a digital balance but

underneath the electrode. Another container is placed in the ambient and on top of another digital balance.

2. Set the distance between the wire and the surface of the container to one inch.
3. Set the high-voltage power supply to positive polarity.
4. Leave the blower off.
5. Record the weight of the two containers used in the experiment.
6. Water is slowly added to these two containers. The amount of water added and the total weight of the container are recorded.
7. Charge the electrode. The applied voltage is initially set to 14 kV.
8. The bottom plate of the container underneath the wire is grounded.
9. The weights of the two containers with water are recorded with a sampling rate of ten seconds through a personal computer.
10. The temperature and humidity of the ambient air are measured every ten seconds. The variation of temperature and humidity as a function of time is monitored using the Dickson Ware software through a personal computer.
11. Each set of experiment is continued for at least 5 hours. The voltage is increased to 20 kV with an increment of 1 kV. For each voltage, repeat step four to step ten.
12. Turn the blower on to provide an additional airflow through the channel. Repeat step five to step eleven.
13. Set the high-voltage power supply to negative polarity. Repeat step four to twelve.

The voltage for corona onset and spark over has been determined before the experiments. Initially, when the applied voltage is lower than 14 kV, the multimeter can measure no current. Only when the applied voltage is 14 kV and above, a hissing sound appears and some current can be detected in the grounded plate by the multimeter, which marks the onset of corona discharge. When the applied voltage is higher than 21 kV, there is a cracking sound originating from the wire due to spark over. When the voltage is over 23 kV, the spark over can be visually observed in the dark room. Therefore, in each series of experiments, the range of applied voltage is selected from 14 to 20 kV with 1 kV increments.

3.1.4 Data Analysis

Water Evaporation Data Analysis

The experimental data collected by the computer are used to plot the evaporation curves. These data points usually can be best fitted with a linear curve and the slope of the curve is determined. Figure 3.9 shows a typical evaporation curve resulting from applying a positive voltage of 16 kV without cross-flow. The lower curve and data points represent the results obtained in the test section and the upper curve and points represent the results obtained in ambient. The slope of the curve is defined as the evaporation rate of the experiment, and the evaporation enhancement is defined as the ratio of the evaporation rate of the test section to that of the ambient air. For this particular case, the water evaporation rate with electric field is -0.0177 g/s and that from the ambient is -0.006 g/s. They are negative since the total weight of water decrease over time. With the above definition, the evaporation enhancement is calculated to be 2.95, which means that the evaporation rate increases 295% with the application of electric field.

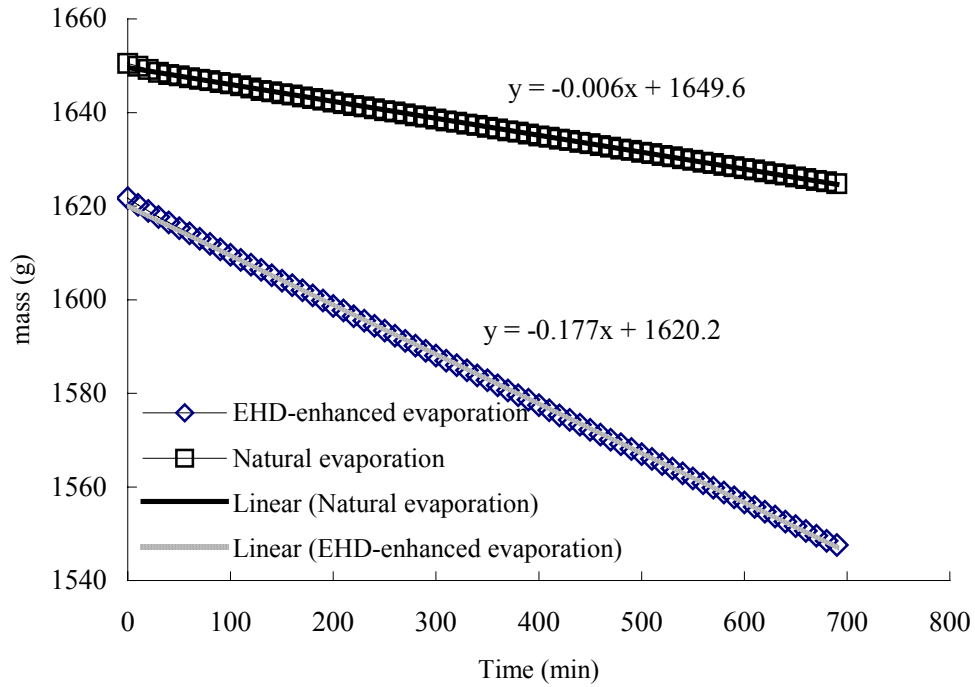


Figure 3.9 Typical experimental results with an applied voltage of 16 kV without cross-flow

Ambient Conditions

The ambient temperature and humidity have been recorded by the temperature/humidity data logger. The average temperature and humidity is then calculated and used in the analysis of experiment results (Figure 3.7).

3.1.5 Calculation of Sherwood Number

The Sherwood number, which is a dimensionless mass transfer coefficient, can be defined based on the diameter of the wire as [33]

$$Sh = \frac{\alpha_D d}{D}. \quad (3.1)$$

Since the mass transfer rate at the water surface is given by

$$\dot{m} = \alpha_D A_c (c_w - c_\infty), \quad (3.2)$$

then the mass transfer coefficient α_D can be written as

$$\alpha_D = \dot{m} / A_c (c_w - c_\infty). \quad (3.3)$$

The Sherwood number thus becomes

$$Sh = \frac{\alpha_D d}{D} = \frac{\dot{m} d}{D A_c (c_w - c_\infty)}. \quad (3.4)$$

To calculate the Sherwood number, the mass transfer rate can be measured directly from the experiment. However, diffusion coefficient (D), water vapor concentration at the water surface (c_w), and that at the ambient air (c_∞) need to be determined before the calculation of Sherwood number.

Diffusion Coefficient (D)

The diffusion coefficient (D) can be found from literature [38, 39] for some specific temperatures and pressures (T_0 and P_0). A semi-empirical correlation has developed to predict the diffusion coefficient at any given temperature T and pressure P.

For binary mixtures, the correlation is given by

$$D \cong D_0 \frac{P_0}{P} \left(\frac{T}{T_0} \right)^{1.75}. \quad (3.5)$$

For water vapor diffusing to dry air, the reference values are

$$P_0 = 101325 \text{ Pa}, T_0 = 298 \text{ K}, \text{ and } D_0 = 2.6\text{e-}5 \text{ m}^2/\text{s}.$$

Water Vapor Concentration in the Ambient Air (c_∞)

The ambient temperature (T_∞) and relative humidity (ϕ) were measured using the temperature/humidity data logger in the experiments. The specific humidity (ω_∞) can be obtained from [40]

$$\omega_{\infty} = \frac{0.622\phi P_g}{P - \phi P_g}, \quad [\text{g water/kg air}] \quad (3.6)$$

where P_g is the saturated vapor pressure at temperature T_{∞} .

The specific humidity (ω_{∞}) can be converted to water vapor concentration (c_{∞}) using the following equation.

$$c_{\infty} = \frac{\omega_{\infty} \rho_{\text{air}}}{\left(1 + \frac{\omega_{\infty}}{1000}\right)}. \quad [\text{g/m}^3] \quad (3.7)$$

Water Vapor Concentration at the Sample Surface (c_w)

At the water surface, the relative humidity equals 100% ($\phi = 1$). Assuming the temperature and pressure at the water surface are the same as the ambient air, the concentration of water vapor at the water surface can be determined using the same approach outlined earlier for the ambient air.

$$\omega_w = \frac{0.622P_g}{P - P_g}, \quad [\text{g water/kg air}] \quad (3.8)$$

$$c_w = \frac{\omega_w \rho_{\text{air}}}{\left(1 + \frac{\omega_w}{1000}\right)}. \quad [\text{g/m}^3] \quad (3.9)$$

3.1.5 Results and Discussion

In both polarities (positive and negative), two series of experiments have been conducted, one is without cross-flow, and another one is with cross-flow. Which means that there are four series of experiments that have been conducted.

- Series one: Positive corona discharge, without cross-flow
- Series two: Positive corona discharge, with cross-flow ($u_i = 2.2$ m/s)
- Series three: Negative corona discharge, without cross-flow

- Series four: Negative corona discharge, with cross-flow ($u_i = 2.2$ m/s)

For all the experiments conducted, the wire is being held at one inch above the water surface. The weight loss of water, ambient temperature and humidity were measured at a ten-second interval. In addition, the corona current has been recorded, which is used in the numerical simulation in the next section. It should be noted that the variation of ambient temperature during the experiment was generally small as the lab was under well temperature control. However, it was noticed that the variation of humidity in some cases was significant, which might have contributed to the scattering of data reported in the results.

Figure 3.10 shows the results of water evaporation without cross-flow for both positive and negative corona discharge. It can be observed that the corona wind enhances the evaporation process since the enhancement is increased linearly with the applied voltage. The evaporation rate was enhanced from 179% to 406% when the applied voltage increased from 14 kV to 20 kV for positive corona discharge and from 156% to 352% for negative corona discharge over the same range in applied voltage. The evaporation enhancement with the cross-flow (2.2 m/s) (Figure 3.11) remained almost the same throughout the entire range of applied voltage. This is because the cross-flow dominated the flow field and the secondary flow induced by the corona wind was suppressed. Therefore, the corona wind produced insignificant effect on the enhancement of water evaporation. For this case, the average evaporation enhancement is 353% for positive corona discharge and 278% for negative corona discharge.

The above analysis did not consider the effect of ambient conditions. It should be noticed that the ambient conditions for each experiment were different. To generalize the

results obtained, the experimental data are expressed in terms of dimensionless governing parameters. Sherwood number based on the diameter of the wire has been defined in equation (3.1), which has a maximum uncertainty of 8%. Another two dimensionless parameters are the EHD Reynolds number (Re_{EHD}) and the EHD number (N_{EHD}), which are defined separately below [35].

$$Re_{EHD} = \frac{u_e d}{\nu} = \left[\sqrt{\frac{I_s}{\rho b A_p}} \right] \frac{d}{\nu}, \quad (3.10)$$

$$N_{EHD} = \frac{u_e}{u_i}. \quad (3.11)$$

where u_e is the characteristic corona wind velocity. Since u_e is difficult to measure directly and accurately without a special instrument [41], its representative value is calculated based on the measured corona current (I). The maximum uncertainties for the EHD Reynolds and EHD numbers were calculated to be 17%. The high uncertainty is mainly due to the measurements of corona current, particularly at voltages close to the threshold voltage.

For experiments conducted in the absence of cross-flow, the evaporation enhancement by electric field can be expressed in terms of the Sherwood number as a function of the EHD Reynolds number. Since the corona current increases with the applied voltage, it is clear that the EHD Reynolds number also increases with the applied voltage. The results are presented in Figure 3.12 for experiments conducted in the absence of cross-flow for both positive and negative corona discharges. It can be observed from this figure that Sherwood number increases linearly with the applied

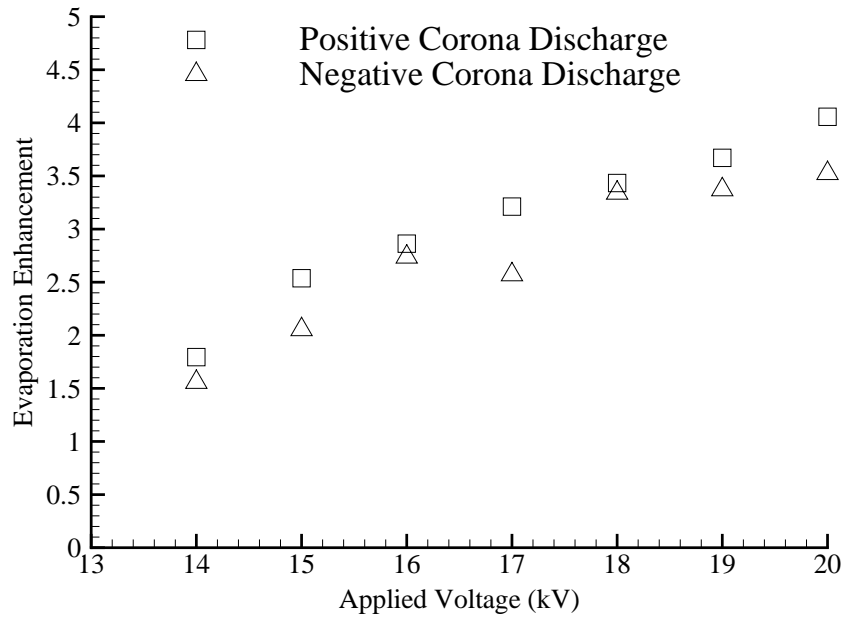


Figure 3.10 Water evaporation enhancement without cross-flow for both positive and negative corona discharge

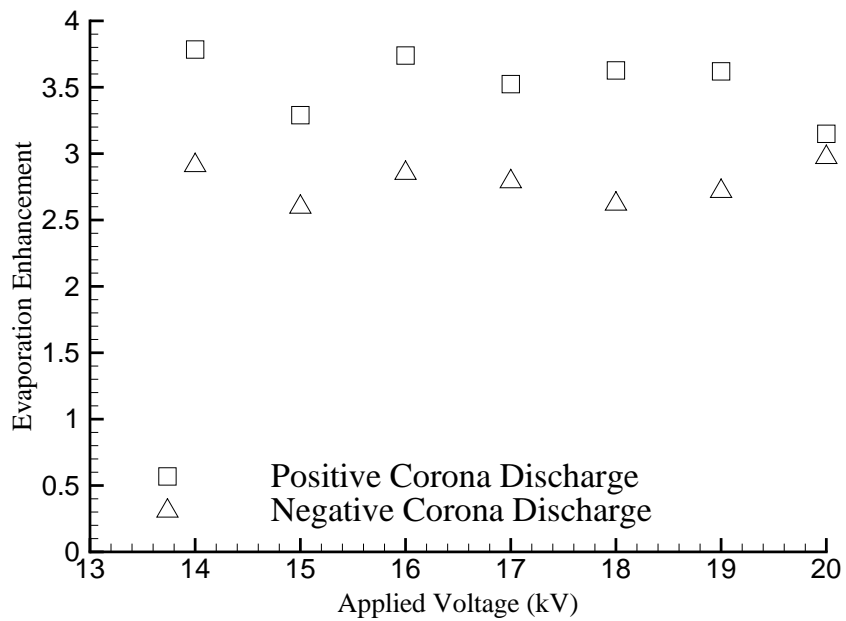


Figure 3.11 Water evaporation enhancement with cross-flow for both positive and negative corona discharge ($u_i = 2.2$ m/s)

voltage. The Sherwood number increases from 0.099 to 0.168 for positive corona discharge and from 0.057 to 0.172 for negative corona discharge when applied voltage is increased from 14 kV to 20 kV. This linear relationship is similar to the evaporation enhancement shown in Figure 3.10. Also, from the figure, it shows that the Sherwood number is greater with the negative corona discharge than that of positive corona. This may first seem to be in contradiction to the earlier observation from Figure 3.10. However, for the same applied voltage, a higher EHD Reynolds number is obtained for positive corona discharge than that for negative discharge. One can see from the definition of the EHD Reynolds number (equation 3.10) that it is influenced by the ambient condition since the corona current, the air density, and the viscosity of air all change with the ambient conditions. Therefore, EHD Reynolds number is more appropriate than the voltage alone to represent the electric field for experiments conducted in varying ambient conditions.

To further eliminate the influence caused by the variation of ambient conditions, the Sherwood numbers presented above are compared with those obtained from experiments conducted under the open air with the same ambient conditions but without the electric field (Figure 3.13). One can observe from Figure 3.13 that the enhancement in the evaporation rate increases linearly with the EHD Reynolds number. The results can be best correlated using the following functional form.

$$\frac{Sh}{Sh_0} = 1 + a Re_{EHD}, \quad (3.12)$$

where a is a constant. In this form, the enhancement in water evaporation reduces to unity when the electrical field is not present (i.e., $Re_{EHD} = 0$). A larger value of the

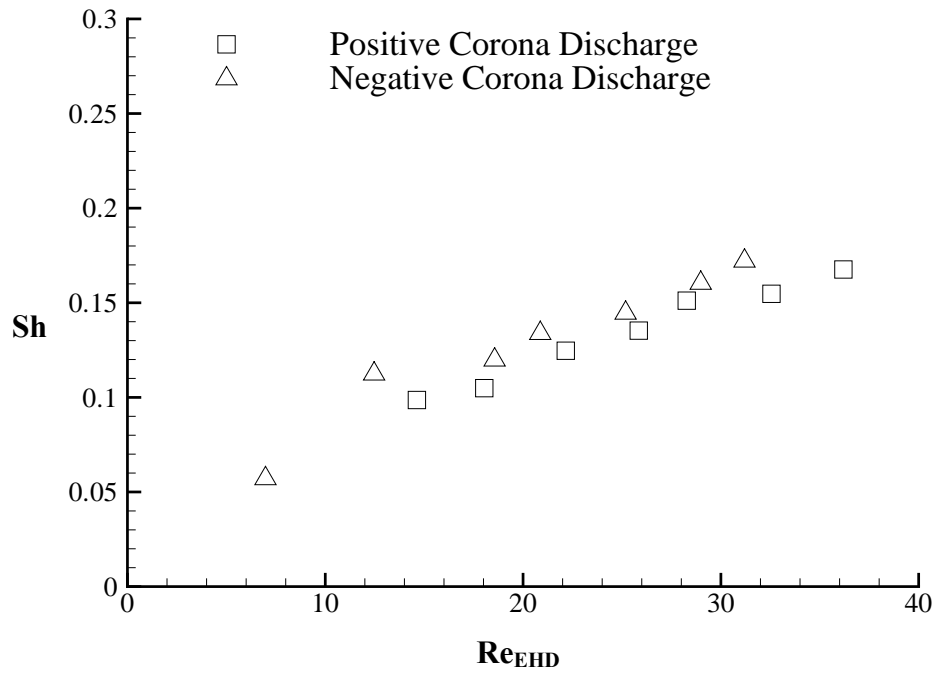


Figure 3.12 Variation of Sherwood number with EHD Reynolds number in the absence of cross-flow

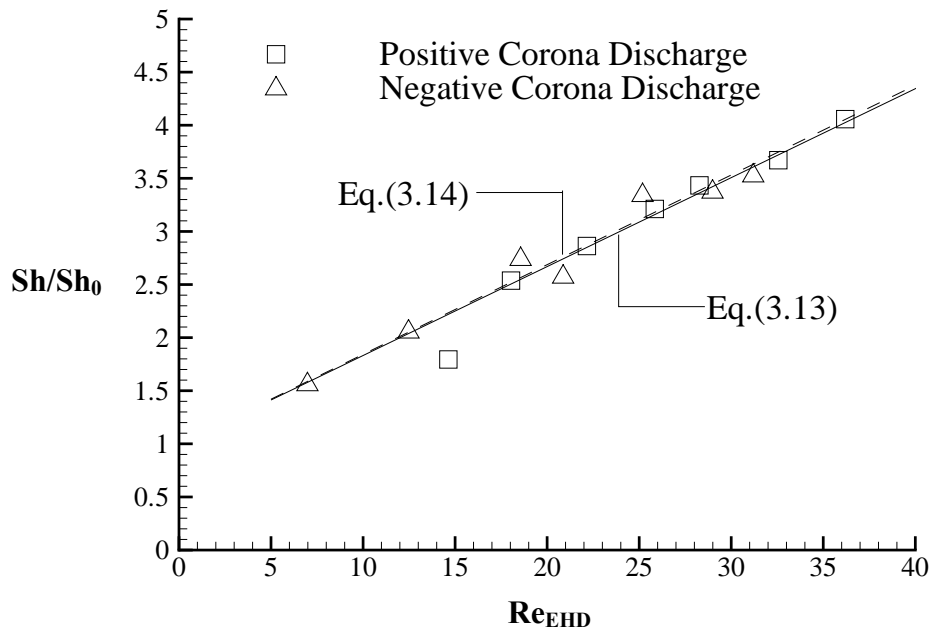


Figure 3.13 Water evaporation enhancement in the absence of cross-flow

coefficient a implies that the enhancement in water evaporation is greater. The correlations for positive and negative corona discharges are given separately below.

$$\text{Positive Corona Discharge: } \frac{Sh}{Sh_0} = 1 + 0.0826 Re_{EHD}, \quad (3.13)$$

$$\text{Negative Corona Discharge: } \frac{Sh}{Sh_0} = 1 + 0.0841 Re_{EHD}. \quad (3.14)$$

With the simultaneous presence of electric field and cross-flow, the results are presented as a function of the Sherwood number and EHD number (Figure 3.14). The EHD number has a value of zero when there is no electric field applied and infinity when there is no cross-flow of air over the water surface. A large EHD number implies that the electric body force is dominant over the flow inertia and on the other hand, a small EHD number indicates that the flow inertial force is dominant over the electric body force. From Figure 3.14 one can observe that the evaporation rates in terms of the Sherwood number have an average value that is nearly independent of the EHD number. The reason why the evaporation rate becomes independent of the EHD number is because the effect of corona wind is largely suppressed by the high air velocity ($u_i = 2.2$ m/s).

To evaluate the enhancement in the evaporation rate due to both electric field and cross-flow, the results are again compared with those obtained from the companion experiments. The results are presented in Figure 3.15. As observed, there is no significant variation in the enhancement of water evaporation for the range of the EHD number considered. The average enhancement in water evaporation using a wire electrode with positive corona is 353% while that of negative corona is only 278%. As explained earlier, the evaporation rate in this range of the EHD number is mainly controlled by the inertial force (i.e., the bulk airflow). The effect of corona wind

becomes insignificant and therefore the results are independent of the EHD number. To support the above statement, a separate experiment was carried out with the airflow alone. The average enhancement in water evaporation by airflow alone was found to be 263%, which supports the earlier observation that the secondary flow induced by corona wind is suppressed and confined to a smaller region near the wall when the velocity of cross-flow increases.

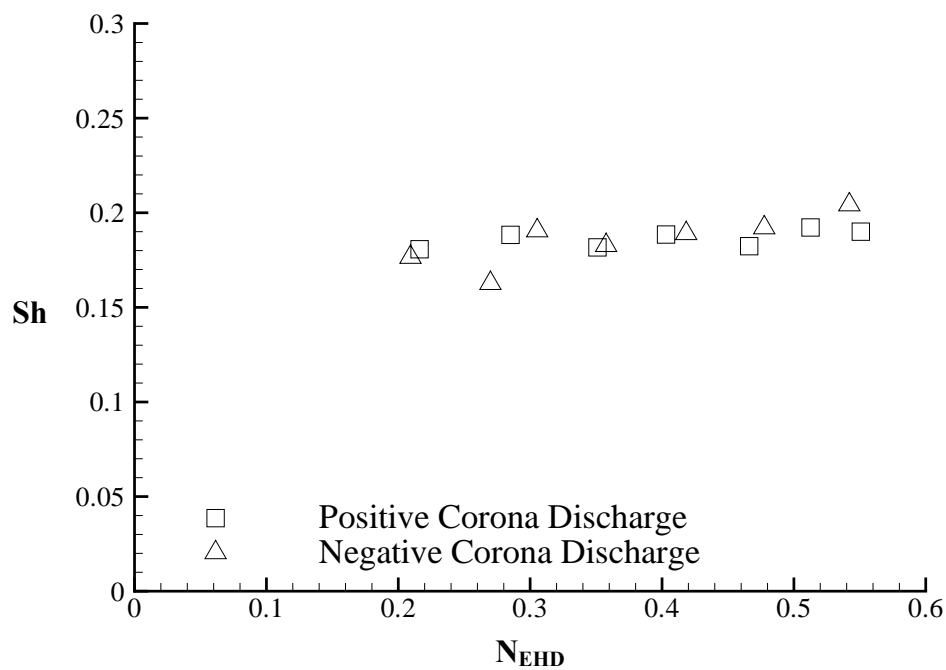


Figure 3.14 Variation of Sherwood number with the EHD number in the presence of cross-flow

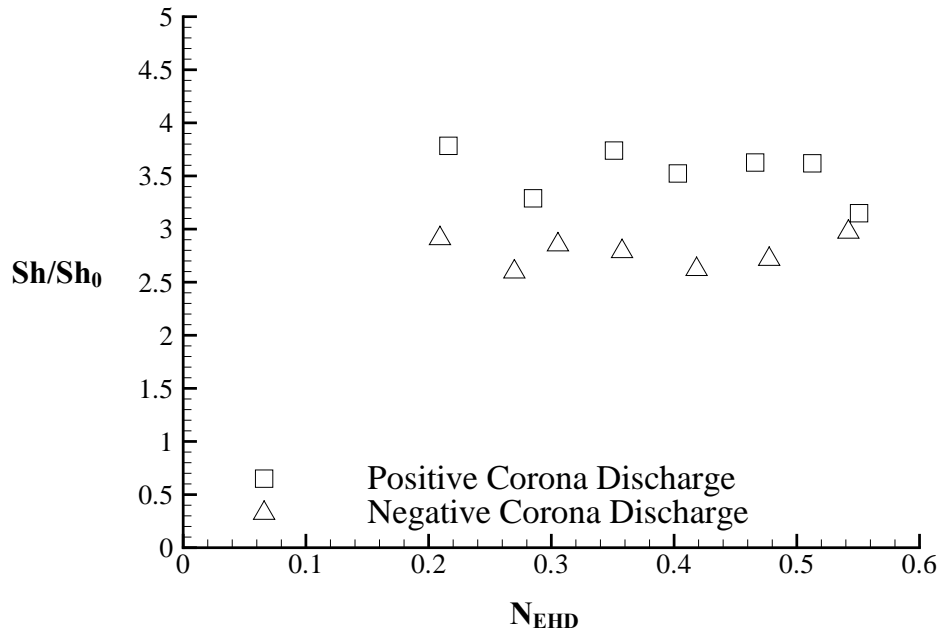


Figure 3.15 Water evaporation enhancement in the presence of cross-flow

3.2 Numerical Simulation

This section presents the numerical verification of the experimental study discussed in the previous section. The configuration of the actual experimental setup is simplified to a two-dimensional channel as shown in Figure 3.16. A wire is suspended one inch above the sample container, which is filled with water and is placed underneath the bottom wall of the channel. A blower delivers air through the channel to provide a uniform cross-flow.

3.2.1 Electric Field

The study presented in the previous section has verified that cross-flow has negligible effect on the electric field, and Joule heating is not a main source of heat for most applications. Therefore, in this numerical study, the electric field is assumed one-way coupled to the flow field and the effect of Joule heating is negligible. For one-way

coupling, the algorithm used to calculate the electric field is the same as that outlined in Chapter two. Recall that the governing equations are given by

$$\nabla^2 V = -\frac{\rho_c}{\epsilon}, \quad (3.15)$$

$$\nabla \rho_c \cdot (\mathbf{E}) + \frac{\rho_c^2}{\epsilon} = 0. \quad (3.16)$$

Previous researches [7-9, 12-13] have shown that corona wind is only concentrated around the electrode. To save the computational time and effort, a symmetric channel shown in Figure 3.17 is used for the simulation of the electric field. The left half of the channel (shaded area) is used as the computational domain. Since evaporation takes place between the air in the channel and the water in the container, an interface is involved in the computation of electric field.

Boundary and Interface Conditions

For experiments conducted in section 3.1, the wire was suspended one inch above the water surface. One end of the wire was connected to the high-voltage power supply. The channel walls were electrically insulated. The container walls were also insulated except for the bottom wall, which was grounded. Thus, the boundary conditions for the electric field are

$$V = V_0, \quad \text{at wire} \quad (3.17a)$$

$$V = 0, \quad \text{along the bottom wall of the container} \quad (3.17b)$$

$$\frac{\partial V}{\partial y} = 0, \quad \text{along the channel walls} \quad (3.17c)$$

$$\frac{\partial V}{\partial x} = 0, \quad \text{along the side walls of the water container} \quad (3.17d)$$

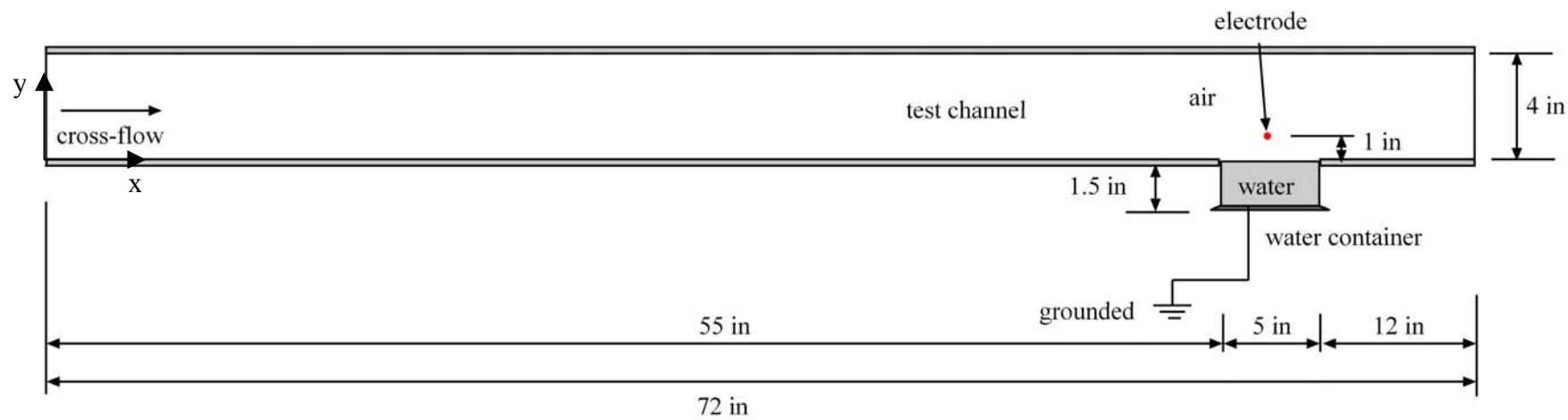


Figure 3.16 A two-dimensional channel with a pool of water in the bottom wall

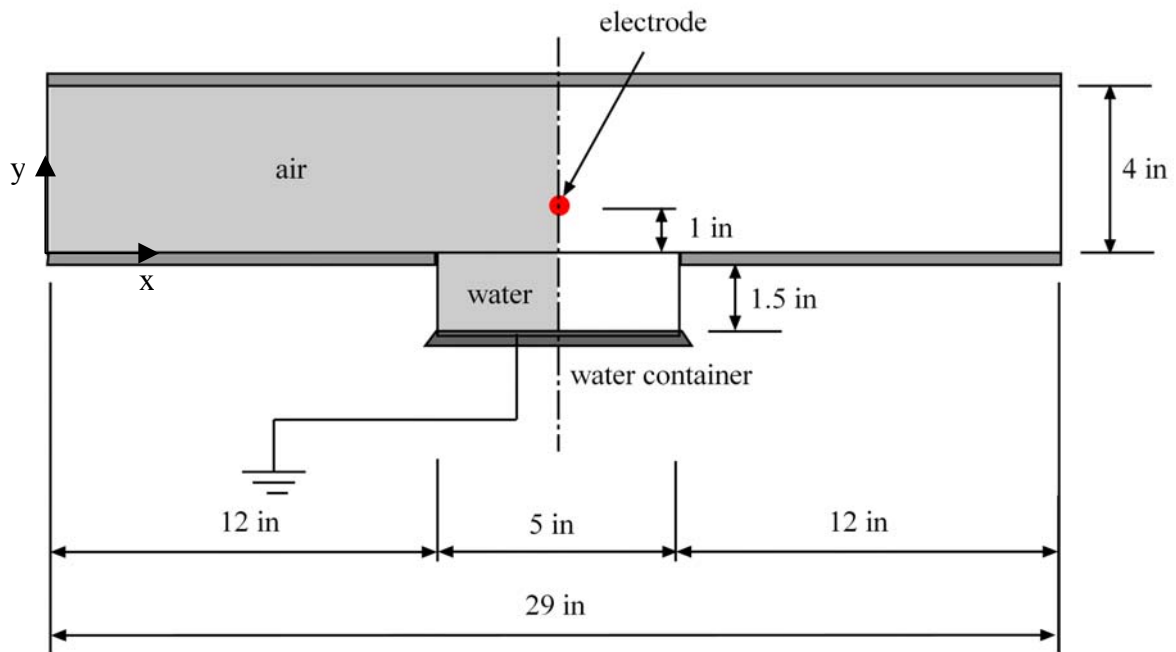


Figure 3.17 The symmetric geometric channel for electric field numerical simulation

$$\frac{\partial V}{\partial x} = 0, \quad \text{at the inlet and exit of the channel} \quad (3.17e)$$

$$\frac{\partial V}{\partial x} = 0. \quad \text{along the symmetric line} \quad (3.17f)$$

When more than one dielectric material is involved in the calculation of the electric field, for example, air and water in this study, one must know the interface conditions across the material discontinuities. This means that electric field and charge density must satisfy certain conditions at the interface [42-44]. First consider the normal components of \mathbf{E} and \mathbf{D} at the interface using the incremental volume represented by the cylinder shown in Figure 3.18. Let the height of the cylinder approaches zero so that no flux leaves the cylinder through the peripheral surface. If subscript n denotes the normal component of the flux density and the positive direction is pointed from water region to air region, then one has

- The flux leaving the top surface = $D_{na} S$
- The flux leaving the bottom surface = $-D_{nw} S$
- Charge density in the cylinder = $\rho_s S$

where S is the area of the top or bottom surface, ρ_s is the surface charge density (C/m^2), which will be determined later. From Gauss's law, the total flux leaving the volume through the top and bottom surface on the cylinder is equal to the charges enclosed in the cylinder. Therefore, the relation between the flux and the charge density is given by

$$D_{n,a} - D_{n,w} = \rho_s. \quad (3.18)$$

Substitute the relation between \mathbf{D} and \mathbf{E} (equation (2.4)) to equation (3.18), one yields

$$\epsilon_a E_{n,a} - \epsilon_w E_{n,w} = \rho_s. \quad (3.19)$$

Equation (3.19) is the first interface condition between two dissimilar dielectrics.

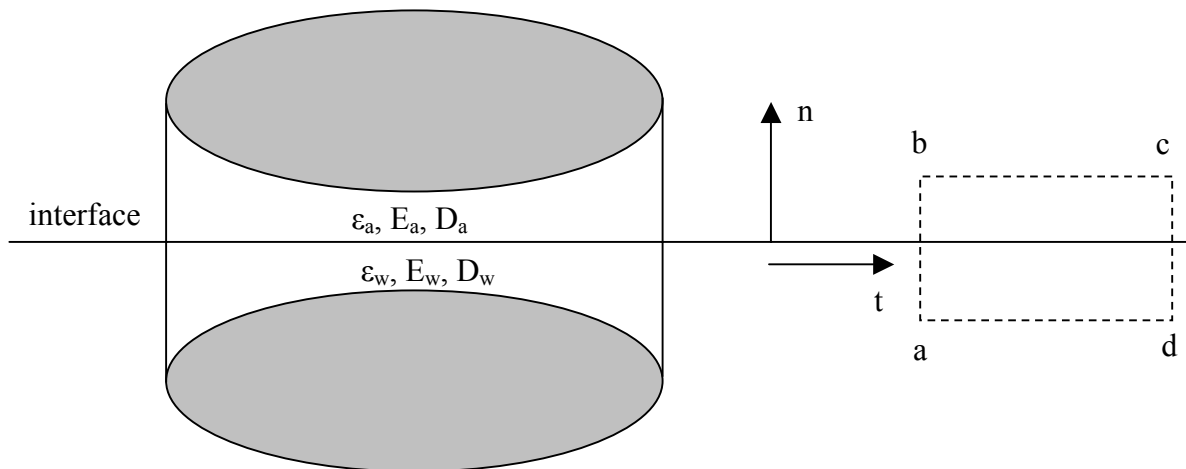


Figure 3.18 The surface and contour used to determine the boundary conditions at the interface between two dissimilar dielectrics

The second interface condition comes from the behavior of the tangential components of \mathbf{E} and \mathbf{D} at the interface using the rectangular path “abcd” in Figure 3.18. When the height of the rectangular path goes to zero, the contributions from the left and right branches of the path become negligible. If subscript t denotes the tangential component of the electric field, the conservative property of \mathbf{E} around the closed path “abcd” gives

$$a \rightarrow b: E_w \cdot d\vec{l} = E_{t,w} l_{ab},$$

$$b \rightarrow c: 0,$$

$$c \rightarrow d: \vec{E}_a \cdot d\vec{l} = -E_{t,a} l_{cd},$$

$$d \rightarrow a: 0,$$

$$\oint \vec{E} \cdot d\vec{l} = 0 \rightarrow E_{t,w} = E_{t,a}. \quad (3.20)$$

This condition shows the tangential components of \mathbf{E} are always continuous across a dielectric interface. Since $\mathbf{E} = -\nabla V$, the tangential component of the electric field is continuous also. That is

$$V_{P,a} = V_{P,w} = V_P. \quad \text{at the interface} \quad (3.21)$$

This is the second interface condition between two dissimilar dielectrics. The first and second interface conditions together can determine the electric potential distribution at the interface.

At the interface between two media that have nonzero conductivities, the law of current continuity places one more constraint on the fields, which is the third interface condition. For the steady state case, the integral form of the continuity equation becomes

$$\oint \mathbf{J} \cdot d\mathbf{s} = 0. \quad (3.22)$$

Evaluating this integral around the cylinder shown in Figure 3.18 yields the following relationship between the normal components of \mathbf{J} on each side of the interface.

$$J_{n,a} = J_{n,w}. \quad (3.23)$$

$$\text{Since } J_n = \sigma E_n = -\sigma \frac{\partial V}{\partial n}, \quad \sigma = \rho_{cP} b, \quad (3.24)$$

equation (3.24) becomes

$$\rho_{cP,a} b_a \frac{\partial V}{\partial y} \Big|_a = \rho_{cP,w} b_w \frac{\partial V}{\partial y} \Big|_w. \quad (3.25)$$

The subscript ‘‘a’’ represents air and ‘‘w’’ represents water. The above equation gives the relation between the charge densities at the two sides of the interface, which is the third interface condition.

After introducing the third interface condition, the surface charge density in equation (3.19) can be determined by substituting equation (3.24) into equation (3.19).

$$\left. \begin{array}{l} \varepsilon_a E_{n,a} - \varepsilon_w E_{n,w} = \rho_s \\ E_n = \frac{J_n}{\sigma}, \quad J_{n,a} = J_{n,w} = J_n \end{array} \right\} \rightarrow \rho_s = J_n \left(\frac{\varepsilon_a}{\sigma_a} - \frac{\varepsilon_w}{\sigma_w} \right) = J_n \left(\frac{\varepsilon_a}{\rho_{cP,a} b_a} - \frac{\varepsilon_w}{\rho_{cP,w} b_w} \right). \quad (3.26)$$

To implement the interface conditions in numerical simulation, a method involving the use of imaginary nodal points is used.

Imaginary Nodal Points

The first two interface conditions introduced above (equation (3.19) and (3.21)) are implemented through the use of imaginary nodal points [44], shown in Figure 3.19, to determine the electric potential distribution at the interface in the computational domain. The solid circles refer to the actual nodal points whereas the hollow circles represent the imaginary nodal points. Because of the difference in the permittivity and ion mobility in

air and water, the electric potential at the interface can no longer be expressed directly using the formulations derived in the previous section. The electric potential at the interface can be represented by two distinct expressions depending on which region is involved. When applying the relation between \mathbf{E} and V to equation (3.19), one yields

$$-\varepsilon_a \left. \frac{dV}{dy} \right|_a + \varepsilon_w \left. \frac{dV}{dy} \right|_w = \rho_s. \quad (3.27)$$

With the central difference approximation, the above equation can be rewritten as

$$\varepsilon_w \frac{V_{Na} - V_S}{2\Delta} - \varepsilon_a \frac{V_N - V_{Sa}}{2\Delta} = \rho_s. \quad (3.28)$$

Two charge densities are involved at the interface nodes. While one is assumed the entire domain is filled with air ($\rho_{cP,a}$), the other is assumed the entire domain is filled with water ($\rho_{cP,w}$). First, assume the entire domain is filled with air, with the first interface condition, V_{Sa} can be determined as follows.

$$V_{P,a} = \frac{1}{4} \left(V_E + V_W + V_N + V_{Sa} + \frac{\rho_{cP,a} \Delta^2}{\varepsilon_a} \right), \quad (3.29)$$

$$V_{Sa} = 4V_{Pa} - \left(V_E + V_W + V_N + \frac{\rho_{cP,a} \Delta^2}{\varepsilon_a} \right).$$

Next, assume the entire domain is filled with water, V_{Na} can be determined in a similar manner.

$$V_{P,w} = \frac{1}{4} \left(V_E + V_W + V_{Na} + V_S + \frac{\rho_{cP,w} \Delta^2}{\varepsilon_w} \right), \quad (3.30)$$

$$V_{Na} = 4V_{Pw} - \left(V_E + V_W + V_S + \frac{\rho_{cP,w} \Delta^2}{\varepsilon_w} \right).$$

The second interface condition dictates that $V_{P,a} = V_{P,w} = V_P$. Therefore

$$V_{Sa} = 4V_P - \left(V_E + V_W + V_N + \frac{\rho_{cP,a} \Delta^2}{\epsilon_a} \right), \quad (3.31)$$

$$V_{Na} = 4V_P - \left(V_E + V_W + V_S + \frac{\rho_{cP,w} \Delta^2}{\epsilon_w} \right).$$

Substituting V_{Na} and V_{Sa} to equation (3.28) gives,

$$V_P = \frac{1}{4\epsilon_w + 4\epsilon_a} [(\rho_{cP,a} + \rho_{cP,w}) \cdot \Delta^2 + 2\rho_s \cdot \Delta + \epsilon_w (V_E + V_W + 2V_S) + \epsilon_a (V_E + V_W + 2V_N)]. \quad (3.32)$$

The dielectric properties, like specific permittivity and ion mobility for air and water, can be found from handbooks [36, 45-46]. The specific permittivity of air is 1 and that of water is 80.1 at 293.2 K. The ion mobility in air at 0 °C and 760 Torr is 1.36×10^{-4}

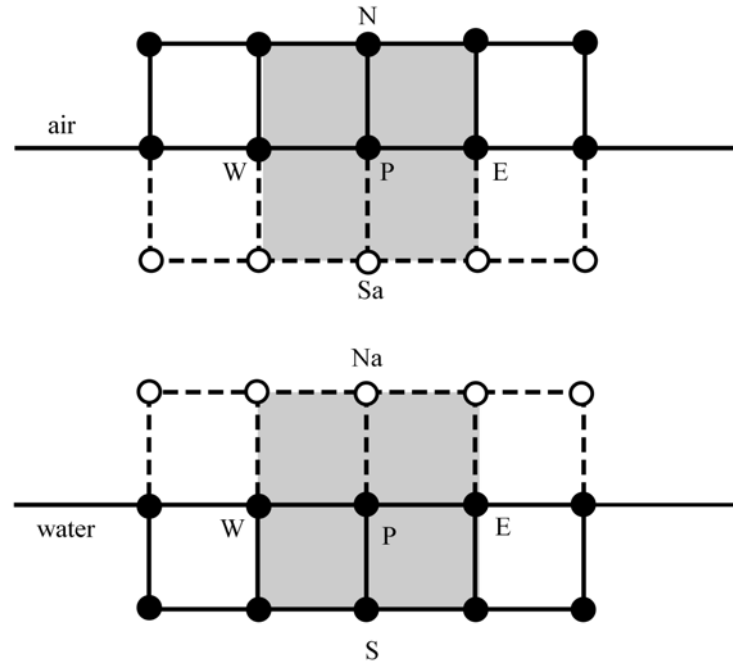


Figure 3.19 Imaginary nodal points

$\text{m}^2/\text{V}\cdot\text{s}$. The ion mobility in water can be estimated from the following equation [1].

$$b_w = \sqrt{\frac{\varepsilon}{\rho}} = \sqrt{\frac{80.1(8.854 \times 10^{-12})}{1000}} = 8.421 \times 10^{-7} \text{ m}^2 / \text{V} \cdot \text{s}.$$

Numerical Procedure

Since the charge density at the interface is not continuous, two sets of charge density at the interface are defined. The numerical procedures to determine the electric potential (V) and charge density (ρ_{cP}) are listed below.

1. Assume that no charge density exists in the entire domain and the surface charge density at the interface equals to zero.
2. Solve the governing equation (3.15) for electric potential in the air region.
3. Solve the interface electric potential from equation (3.32).
4. Solve the governing equation (3.15) for electric potential in the water region.
5. Assume that the interface properties equals to the properties of air, solve the charge density in the air region by governing equation (3.16). The charge density at the interface node ($\rho_{cP,a}$) is thus determined.
6. Determine $\rho_{cP,w}$ using equation (3.25) and $\rho_{cP,a}$ obtained above.

$$\rho_{cP,a} b_a \frac{V_N - V_P}{\Delta} = \rho_{cP,w} b_w \frac{V_P - V_S}{\Delta}, \quad (3.33)$$

$$\rho_{cP,w} = \frac{V_N - V_P}{V_P - V_S} \frac{b_a}{b_w} \rho_{cP,a}.$$

7. Assume that the charge density at the interface equals to $\rho_{cP,w}$, solve the charge density at the water region by equation (3.16).
8. Determine the surface charge density (ρ_s) using equation (3.26).
9. Assume that the charge density at the interface equals to $\rho_{cP,a}$, go back to step two.

10. Repeat step two to step nine till solutions converged.

A typical electric potential and charge density distribution obtained from the present numerical simulation is shown in Figure 3.20.

3.2.2 Flow and Concentration Fields

To simplify the numerical calculations, some assumptions have been made.

1. The water surface is assumed to maintain the same height as the bottom surface of the channel. In this case, the water container is implemented as a boundary condition in the simulation of flow and concentration fields, and the computational domain only consist a channel filled with air and has a water boundary at the bottom (Figure 3.21).
2. The water vapor concentrations in the water surface and ambient air are assumed to maintain constant during the entire drying process.
3. Energy equation is not involved in this study.
4. All properties are assumed constant, and they are evaluated at the average ambient temperature.

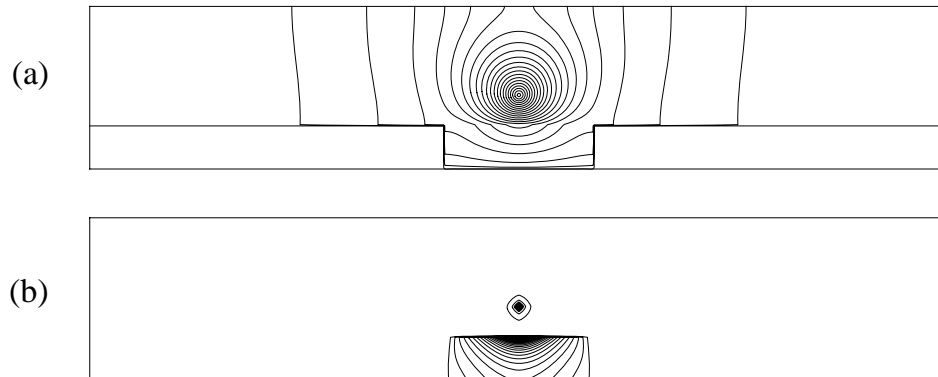


Figure 3.20 Electric field in a two-dimensional channel with a pool of water in the bottom wall ($V_0 = 18$ kV), (a) electric potential (b) charge density

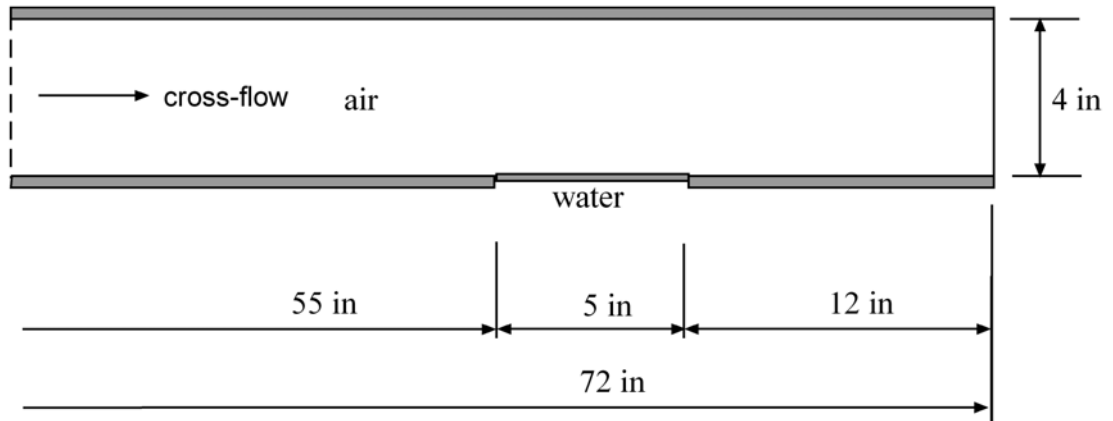


Figure 3.21 Computational domain for the simulation of flow and concentration fields

Based on the above assumptions, the governing equations for the flow and concentration fields are the continuity equation, the Navier-Stokes equations in x and y directions, and the concentration equation.

$$\frac{\partial u}{\partial x} + \frac{\partial v}{\partial y} = 0, \quad (3.34)$$

$$\frac{\partial u}{\partial t} + u \frac{\partial u}{\partial x} + v \frac{\partial u}{\partial y} = -\frac{1}{\rho} \frac{\partial p}{\partial x} + \nu \left(\frac{\partial^2 u}{\partial x^2} + \frac{\partial^2 u}{\partial y^2} \right) + \frac{\rho_c}{\rho} E_x, \quad (3.35)$$

$$\frac{\partial v}{\partial t} + u \frac{\partial v}{\partial x} + v \frac{\partial v}{\partial y} = -\frac{1}{\rho} \frac{\partial p}{\partial y} + \nu \left(\frac{\partial^2 v}{\partial x^2} + \frac{\partial^2 v}{\partial y^2} \right) + \frac{\rho_c}{\rho} E_y, \quad (3.36)$$

$$\frac{\partial c}{\partial t} + u \frac{\partial c}{\partial x} + v \frac{\partial c}{\partial y} = D \left(\frac{\partial^2 c}{\partial x^2} + \frac{\partial^2 c}{\partial y^2} \right). \quad (3.37)$$

The last term in the momentum equations, equations (3.35) and (3.36) represents the electric body force, which provides the coupling from the electric field to the flow field. The governing equations can be non-dimensionalized by introducing the following dimensionless variables.

$$\begin{aligned}
X &= \frac{x}{H}, & Y &= \frac{y}{H}, & C &= \frac{c - c_\infty}{c_w - c_\infty}, & \tau &= \frac{u_e t}{H}, & \text{Pr} &= \frac{\nu}{\alpha}, & \text{Le} &= \frac{\alpha}{D}, \\
U &= \frac{u}{u_e}, & V &= \frac{v}{u_e}, & \Omega &= \frac{\omega H}{u_e}, & \bar{V} &= \frac{V}{V_0}, & \bar{\rho}_c &= \frac{\rho_c}{\rho_{c0}}, & & (3.38) \\
u_e &= \sqrt{\frac{\rho_{c0} V_0}{\rho}}, & U &= \frac{\partial \Psi}{\partial Y}, & V &= -\frac{\partial \Psi}{\partial X}, & \text{Re}_{\text{EHD}} &= \frac{u_e H}{\nu}.
\end{aligned}$$

The dimensionless governing equations in terms of the stream function and vorticity are given by

$$\frac{\partial^2 \Psi}{\partial X^2} + \frac{\partial^2 \Psi}{\partial Y^2} = -\Omega, \quad (3.39)$$

$$\frac{\partial \Omega}{\partial \tau} + \frac{\partial \Psi}{\partial Y} \frac{\partial \Omega}{\partial X} - \frac{\partial \Psi}{\partial X} \frac{\partial \Omega}{\partial Y} = \frac{1}{\text{Re}_{\text{EHD}}} \left(\frac{\partial^2 \Omega}{\partial X^2} + \frac{\partial^2 \Omega}{\partial Y^2} \right) + \left(\frac{\partial \bar{\rho}_c}{\partial Y} \frac{\partial \bar{V}}{\partial X} - \frac{\partial \bar{\rho}_c}{\partial X} \frac{\partial \bar{V}}{\partial Y} \right), \quad (3.40)$$

$$\frac{\partial C}{\partial \tau} + \frac{\partial \Psi}{\partial Y} \frac{\partial C}{\partial X} - \frac{\partial \Psi}{\partial X} \frac{\partial C}{\partial Y} = \frac{1}{\text{Pr Re}_{\text{EHD Le}}} \left(\frac{\partial^2 C}{\partial X^2} + \frac{\partial^2 C}{\partial Y^2} \right). \quad (3.41)$$

The corresponding boundary conditions for the flow and concentration fields with cross-flow are

$$X = 0, \quad \Omega = 0, \quad \Psi = \frac{u_i}{u_e} Y, \quad C = 0. \quad (3.42a)$$

$$X = \frac{L}{H}, \quad \frac{\partial \Omega}{\partial X} = 0, \quad \frac{\partial \Psi}{\partial X} = 0, \quad \frac{\partial C}{\partial X} = 0. \quad (3.42b)$$

$$Y = 1, \quad \Omega = -\frac{\partial^2 \Psi}{\partial^2 Y}, \quad \Psi = u_i / u_e, \quad \frac{\partial C}{\partial Y} = 0. \quad (3.42c)$$

$$\begin{aligned}
Y = 0, \quad \Omega = -\frac{\partial^2 \Psi}{\partial^2 Y}, \quad \Psi = 0, \quad \frac{\partial C}{\partial Y} = 0, \quad \text{channel wall} \\
C = 1, \quad \text{water surface}
\end{aligned} \quad (3.42d)$$

The numerical procedures are similar to those for the EHD-enhanced heat transfer introduced in Chapter two.

3.2.3 The Sherwood Number

Since the concentration equation is similar to the energy equation, some features of the concentration field can be examined from the temperature field by analogy. Similar to the analysis presented in Chapter two, one learns that the flow field is developing through the entire channel and the concentration boundary layer is still thin (less than the channel height) at the end of the channel. Thus, the mass transfer rate (i.e., the evaporation rate) at the water surface can be calculated based on the difference in water vapor concentration between the water surface and ambient air.

$$\dot{m} = -D \frac{dc}{dy} = \alpha_D (c_w - c_\infty). \quad (3.43)$$

The mass transfer coefficient α_D can then be determined as

$$\alpha_D = \frac{1}{c_w - c_\infty} \left(-D \frac{dc}{dy} \right). \quad (3.44)$$

The average mass transfer coefficient based on the length of the water surface L_w is given by

$$\bar{\alpha}_D = \frac{1}{L_w} \int_{x_{w1}}^{x_{w2}} \frac{-D}{c_w - c_\infty} \frac{dc}{dy} dx. \quad (3.45)$$

In the dimensionless form, it is given by

$$\bar{\alpha}_D = \frac{1}{L_w} \int_{X_{w1}}^{X_{w2}} -D \frac{dC}{dY} dX. \quad (3.46)$$

Substitute the average mass transfer coefficient to the definition of the average Sherwood number, it gives

$$Sh = \frac{\bar{\alpha}_D L_w}{D} = \int_{X_{w1}}^{X_{w2}} -\frac{dC}{dY} dX. \quad (3.47)$$

3.2.4 Code Validation

Due to the scarcity of numerical and analytic data for mass transfer, and the similarity of the governing equations between heat and mass transfer, forced convection heat transfer is chosen to validate the code. By analogy, the physic model of heat transfer is shown in Figure 3.22.

The thermal and hydrodynamic entrance lengths can be calculated using equations (2.49) and (2.50). For this case, the hydrodynamic entrance length is calculated to be 3.43 m and the thermal entrance length 17.64 m. The total length of the channel is 72 inches (1.83 m), which is smaller than both entrance lengths. This means the flow is both thermally and hydrodynamically developing.

Only laminar flow is considered. To choose a proper empirical correlation for this model, the thickness of the hydrodynamic boundary layer at the end of the channel is calculated.

$$\delta = 4.64 \sqrt{\frac{\nu x}{u_{\infty}}} = 4.64 \sqrt{\frac{15.11 \times 10^{-6} (72)(0.0254)}{0.25}} = 0.0469 \text{ m} \quad (3.48)$$

The height of the channel is 4 inches (0.1016 m). This means at the end of the channel, the hydrodynamic boundary layers developed from the top and bottom surfaces have not merged yet. Thus, for analytic solutions, the channel can be simplified to a flat plate with unheated sections at both ends as shown in Figure 3.23. The Reynolds number and the thickness of the thermal boundary layer at the end of the heat source are

$$\begin{aligned} \text{Re}_x &= \frac{u_{\infty} x}{\nu} = \frac{0.25(60)(0.0254)}{15.11 \times 10^{-6}} = 2.52 \times 10^4 < 5 \times 10^5, \\ \frac{\delta_T}{\delta} &= \frac{0.976}{\sqrt[3]{\text{Pr}}} \left[1 - \left(\frac{x}{x_0} \right)^{-3/4} \right]^{1/3} = \frac{0.976}{\sqrt[3]{0.713}} \left[1 - \left(\frac{1.524}{1.397} \right)^{-3/4} \right]^{1/3} = 0.625 < 1. \end{aligned} \quad (3.49)$$

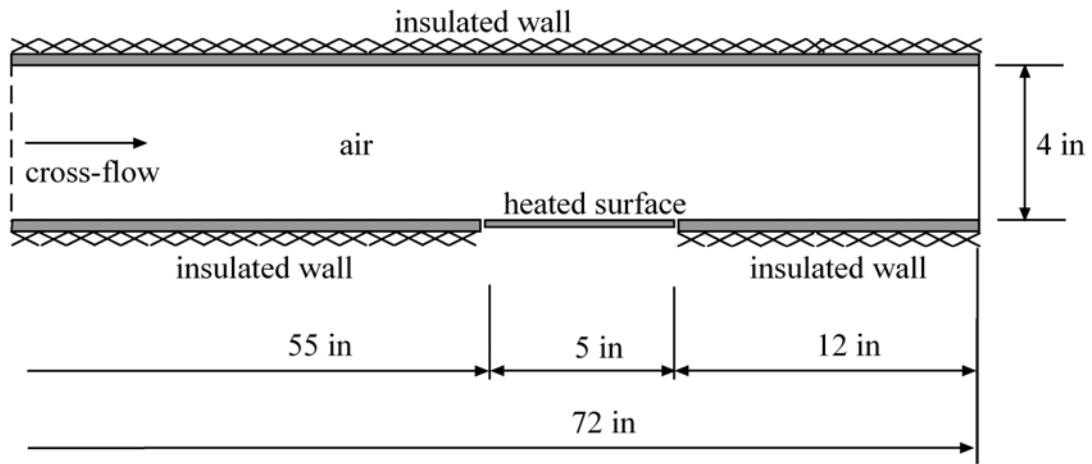


Figure 3.22 The physic model of heat transfer by forced convection

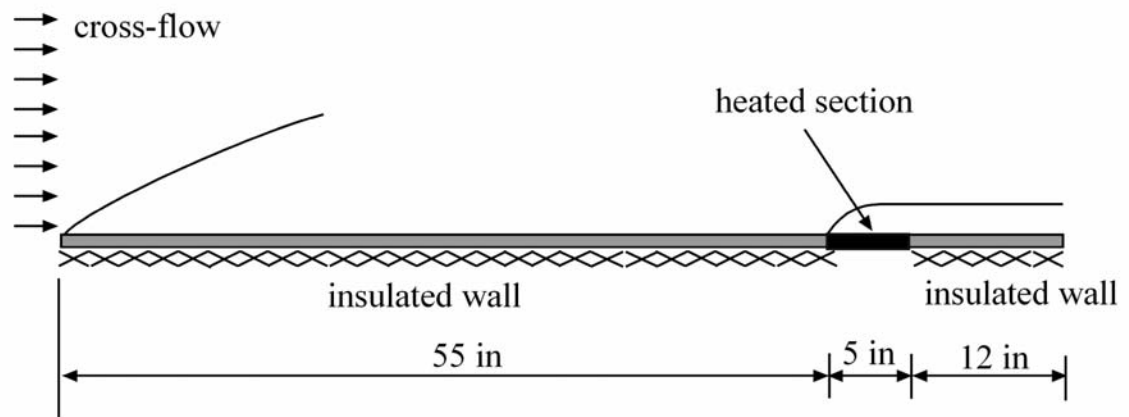


Figure 3.23 Heat transfer from a flat plate with unheated sections

The local heat transfer coefficient along the heated section is given by [32]

$$h_x = 0.331 \frac{k}{x} \text{Pr}^{1/3} \text{Re}^{1/2} \left[1 - \left(\frac{x}{x_0} \right)^{-3/4} \right]^{-1/3} \quad (3.50)$$

Then the average heat transfer coefficient can be determined as

$$\begin{aligned}\bar{h} &= \frac{1}{L_w} \int_{x_{w1}}^{x_{w2}} 0.331 \frac{k}{x} \text{Pr}^{1/3} \text{Re}^{1/2} \left[1 - \left(\frac{x}{x_0} \right)^{-3/4} \right]^{-1/3} dx \\ &= \frac{k}{L_w} 0.331 \text{Pr}^{1/3} \left(\frac{u_\infty}{\nu} \right)^{1/2} \int_{x_0}^{x_1} \frac{\left[1 - \left(\frac{x}{x_0} \right)^{-3/4} \right]^{-1/3}}{x^{1/2}} dx\end{aligned}\quad (3.51)$$

Thus, the average Nusselt number based on the length of the heated section is given by

$$\text{Nu}_{\text{analysis}} = \frac{\bar{h}L}{k} = 0.331 \text{Pr}^{1/3} \left(\frac{u_\infty}{\nu} \right)^{1/2} \int_{x_0}^{x_1} \frac{\left[1 - \left(\frac{x}{x_0} \right)^{-3/4} \right]^{-1/3}}{x^{1/2}} dx. \quad (3.52)$$

The Nusselt numbers for various cross-flow velocities (from 0.1 m/s to 0.25 m/s) are listed in Table 3.1. Note that all the properties of air are evaluated at 20 °C.

For numerical validation, the physical model is shown in Figure 3.22. The energy equation is given by

$$\frac{\partial T}{\partial \tau} + \frac{\partial \Psi}{\partial Y} \frac{\partial T}{\partial X} - \frac{\partial \Psi}{\partial X} \frac{\partial T}{\partial Y} = \frac{1}{\text{Pr Re}} \left(\frac{\partial^2 T}{\partial X^2} + \frac{\partial^2 T}{\partial Y^2} \right), \quad (3.53)$$

which can be obtained by setting $\text{Le} = 1$ in the concentration equation (equation 3.41).

The boundary conditions of the temperature field used in the numerical solution are

$$X = 0, \quad \theta = 0. \quad (3.54a)$$

$$\left. \begin{array}{l} Y = 0, \\ X < X_{w1} \text{ and } X > X_{w2}, \end{array} \right\} \frac{\partial \theta}{\partial Y} = 0, \quad \left. \begin{array}{l} Y = 0, \\ X_{w1} \leq X \leq X_{w2}, \end{array} \right\} \theta = 1. \quad (3.54b)$$

$$Y = 1, \quad \frac{\partial \theta}{\partial Y} = 0. \quad (3.54c)$$

Table 3.1 Comparison of Nusselt numbers for forced convection

Inlet velocity (m/s)	Nu _{analytic}	Nu _{numerical}	Err = $\frac{Nu_{numerical} - Nu_{analytic}}{Nu_{numerical}}$
0.1	9.42	11.21	16%
0.15	11.54	13.26	13%
0.2	13.32	15.13	12%
0.25	14.89	16.55	10%

$$X = \frac{L}{H}, \quad \frac{\partial \theta}{\partial X} = 0. \quad (3.54e)$$

The governing equations and boundary conditions for the flow field is the same as equations (3.39), (3.40), and (3.42). The numerical results for cross-flow velocity varied from 0.1 m/s to 0.25 m/s are listed in Table 3.1 for comparison. The discrepancies found vary from 10 to 16 percent, depending on the Reynolds number, which are acceptable in the consideration of that the analytic result is derived from the integral solution for a flat plate and the numerical result is obtained from computer simulation of a two-dimensional channel.

To verify that a two-dimensional model is adequate for the present numerical study, the present results are compared with those obtained by commercial CFD code Fluent for forced convection mass transfer. For two-dimensional and three-dimensional models in Fluent, when the cross-flow velocity is fixed at 2.2 m/s, the Sherwood number is 51.21 and 47.48 respectively while the result from the present code is 49.90. This shows that the present two-dimensional model is appropriate for the problem considered and it can be used to obtain further results for the study.

3.2.5 Results and Discussion

Uniform grid of (1729 × 97) and a time step of 5×10^{-4} were used for this numerical simulation. It had been tested that numerical results were independent of the grid size and time step. The numerical results were obtained using Boomer Supercomputer in the University of Oklahoma. It took 96 hours to complete the calculation for each case.

Water evaporation under positive corona discharge with cross-flow ($u_i = 1.0$ and 2.2 m/s) has been numerically studied. First, the electric field is calculated; followed by the flow and concentration fields. For the convenience to compare with the experimental results, the Sherwood numbers obtained from the previous experiments are re-calculated to base on the length of water surface as

$$Sh_{\text{exp}} = \frac{Sh L_w}{d}. \quad (3.55)$$

Table 3.2 lists the Sherwood number obtained from this numerical simulation for cross-flow with a velocity of 2.2 m/s. The experimental results are also listed in this table for comparison. The discrepancies between these two results vary from one to eight percent. Recall that the electric field calculation was based on the corona current measured in the experiments. Also, the ambient conditions although were well controlled in the lab, there were still some variations. For example, the temperature and humidity varied from 26.4 °C to 27.2 °C, and 27.4% to 37.8% , respectively during experiments. When considering all these factors, this discrepancy is acceptable. Again, one observes that there is no significant variation in the enhancement of water evaporation for the range of the applied voltage considered. This is because the cross-flow dominates the flow field.

Figure 3.24 shows the variation of flow field with the applied voltage when the cross-flow velocity is fixed at 2.2 m/s. To have a better observation of the change in the flow field due to electric field, the figures shown in Figure 3.24 is only centered on the region near the wire and water surface. One can observe from the contour plots of stream function that the effect of electric body force is only confined to a small region between the wire and the water surface. Also, there is no significant change in the flow field when the applied voltage increases. This is because the cross-flow is dominant and the secondary flow induced by the corona wind is suppressed. Even though, one can still observe the appearance of secondary flow directly between the water surface and wire. When the applied voltage is low, the recirculating cell driven by the secondary flow is small. However, when the applied voltage increases, the recirculating cell grows slightly. That also can be confirmed from the variation of Sherwood number, which increases from 48.08 to 52.10 when the applied voltage increases from 14 kV to 20 kV. The concentration fields exhibit the same trend (Figure 3.25). Since the velocity of the cross-flow is large, water vapor is confined to a relatively narrow region between the water

Table 3.2 Comparison of Sherwood numbers (positive discharge, $u_i = 2.2$ m/s)

Voltage (kV)	Sh_{num}	Sh_{exp}	$Err = \frac{ Sh_{num} - Sh_{exp} }{Sh_{num}} 100\%$
14	48.08	45.90	4.53
15	47.85	47.83	0.38
16	48.46	46.15	4.76
17	49.28	47.88	2.84
18	50.01	46.32	7.56
19	51.06	48.82	4.38
20	52.10	48.26	7.37

surface and airflow above. Also, water vapor is washed away by the cross-flow so quickly that it does not have the opportunity to diffuse to other parts of the channel.

To further examine the effect of cross-flow on the EHD-enhanced water evaporation, numerical simulations and experiments are also performed for the cross-flow with a velocity of 1.0 m/s, and the applied voltage ranging from 14 kV to 20 kV. For this case, both inertial force and electric body force have effects on the flow motion. The Sherwood numbers obtained are listed in Table 3.3. The discrepancies between these two results vary from five to eleven percent. When consider the uncertainty involved in the measurements of the corona current, cross-flow velocity, as well as the variation of ambient conditions in the experiments, and the numerical simulation errors, the discrepancies although slightly higher than the previous case, are still considered acceptable.

One can observe from Table 3.3 that the Sherwood number basically increases with the applied electric voltage. To evaluate the evaporation enhancement by electric field, the Sherwood numbers obtained are also compared with that by forced convection alone, which has a Sherwood number of 31.23. Clearly, the evaporation enhancement is significant when the applied voltage is high. This is due to the impingement of corona wind on the water surface, which disturbs the concentration boundary layer. Since both inertial force and electric body force act simultaneously, their contribution to the evaporation enhancement varies when the applied voltage increases from 14 kV to 20 kV, depending on which force is dominant. When the applied voltage is low (< 16 kV), the electric body force is considerably weak, compared with the cross-flow inertial force. Thus, the evaporation enhancement is mainly contributed by the flow inertia. As such,

Table 3.3 Comparison of Sherwood numbers (positive discharge, $u_i = 1.0$ m/s)

Voltage (kV)	Sh_{num}	Sh_{exp}	$Err = \left \frac{Sh_{num} - Sh_{exp}}{Sh_{num}} \right 100\%$
14	31.81	30.35	4.58
15	34.72	31.38	9.61
16	40.52	36.34	10.32
17	42.29	38.54	8.86
18	44.11	40.49	8.21
19	47.34	43.53	8.04
20	51.09	46.41	9.15

the Sherwood numbers are close to that by the forced convection. With an increase in the applied voltage ($V_0 \geq 16$ kV), the electric body force becomes stronger to overcome the dominance of the flow inertia, the evaporation enhancement starts to increase linearly with the applied voltage. This trend is similar to that observed from the experimental study with the absence of cross-flow.

The interaction between the corona wind and primary flow can also be observed from the flow fields (Figure 3.26). When the applied voltage is low, the secondary flow is insignificant and the streamlines are nearly parallel. When the applied voltage is increases, the secondary flow becomes stronger, and a recirculating cell appears between the wire and water surface. When the applied voltage is increased further, the recirculating cell extends over the entire water surface and results in a large evaporation enhancement.

The concentration fields (Figure 3.27) also show the growing effects of the secondary flow with an increase in the applied voltage. When the electric body force is weak, the water vapor is confined to the boundary layer. When a higher voltage is applied, the boundary layer is disturbed, which generate a large concentration gradient

between the water surface and the air above. This leads to a large Sherwood number. Since the electric field strength is mostly centered at the wire, the cross-flow becomes dominant in the downstream region of the channel, and the water vapor is washed away before it has the opportunity to diffuse to air in the upper part of the channel.

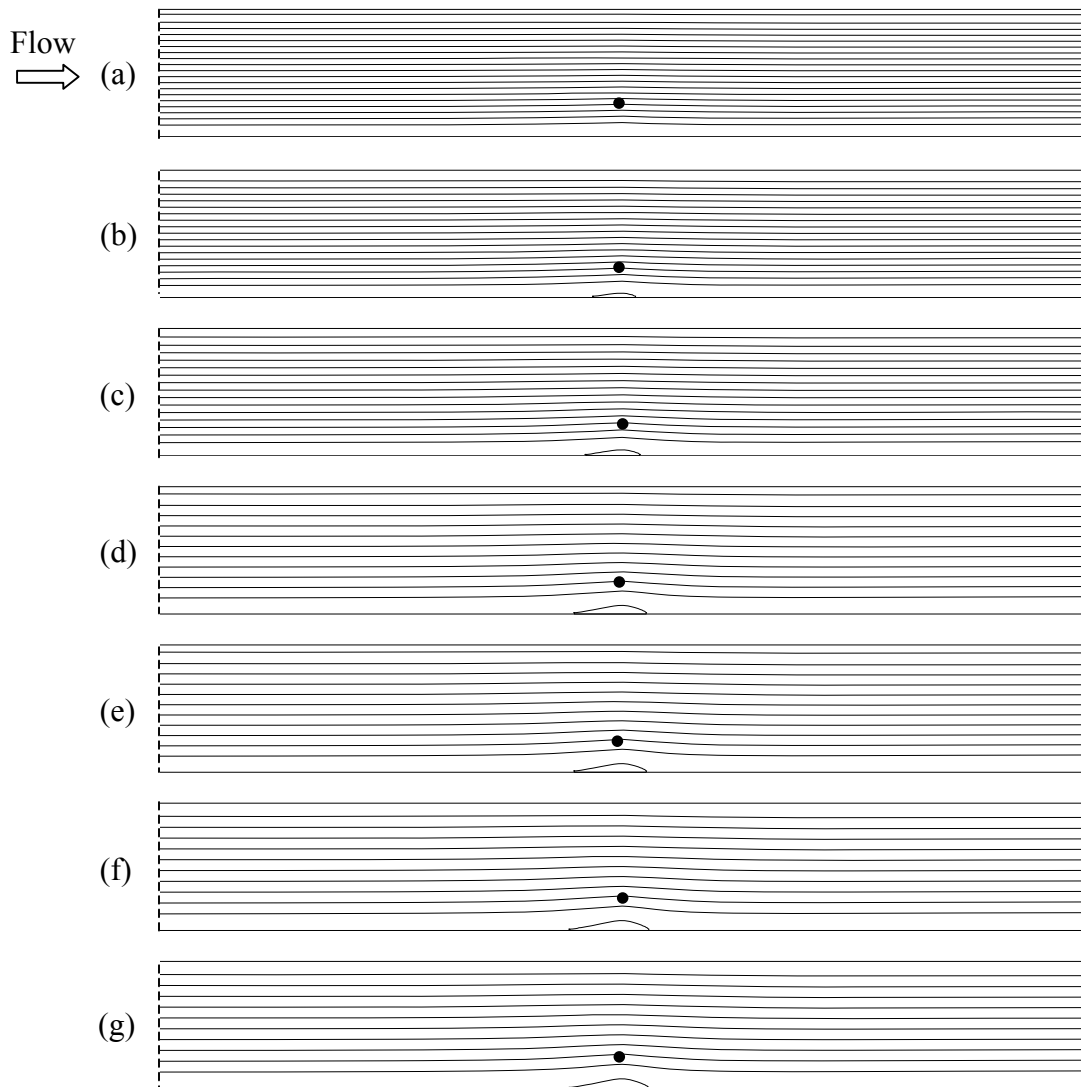


Figure 3.24 Variation of flow fields with applied voltage ($u_i = 2.2$ m/s)

- (a) $V = 14$ kV, $\Psi_{\max} = 0.55$, $\Psi_{\min} = 0.0$, $\Delta \Psi = 0.0275$
- (b) $V = 15$ kV, $\Psi_{\max} = 0.20$, $\Psi_{\min} = 0.01$, $\Delta \Psi = 0.0100$
- (c) $V = 16$ kV, $\Psi_{\max} = 0.16$, $\Psi_{\min} = 0.0$, $\Delta \Psi = 0.0100$
- (d) $V = 17$ kV, $\Psi_{\max} = 0.12$, $\Psi_{\min} = 0.01$, $\Delta \Psi = 0.0100$
- (e) $V = 18$ kV, $\Psi_{\max} = 0.12$, $\Psi_{\min} = 0.0$, $\Delta \Psi = 0.0100$
- (f) $V = 19$ kV, $\Psi_{\max} = 0.11$, $\Psi_{\min} = 0.01$, $\Delta \Psi = 0.0100$
- (g) $V = 20$ kV, $\Psi_{\max} = 0.10$, $\Psi_{\min} = 0.0$, $\Delta \Psi = 0.0100$

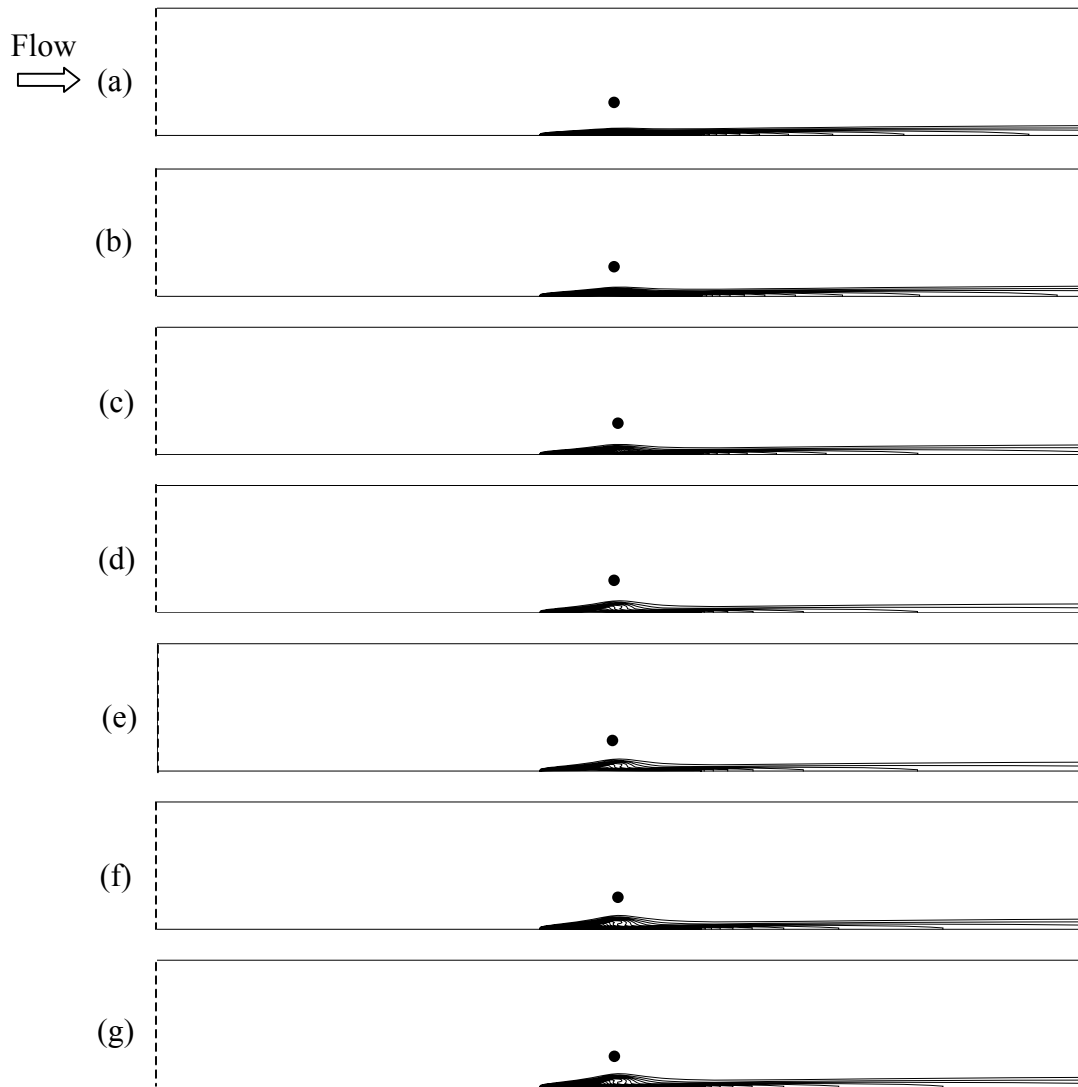


Figure 3.25 Variation of concentration fields with applied voltage
 ($u_i = 2.2$ m/s, $C_{\max} = 1.0$, $C_{\min} = 0.0$, $\Delta C = 0.05$)
 (a) $V_0 = 14$ kV, (b) $V_0 = 15$ kV, (c) $V_0 = 16$ kV, (d) $V_0 = 17$ kV,
 (e) $V_0 = 18$ kV, (f) $V_0 = 19$ kV, (g) $V_0 = 20$ kV

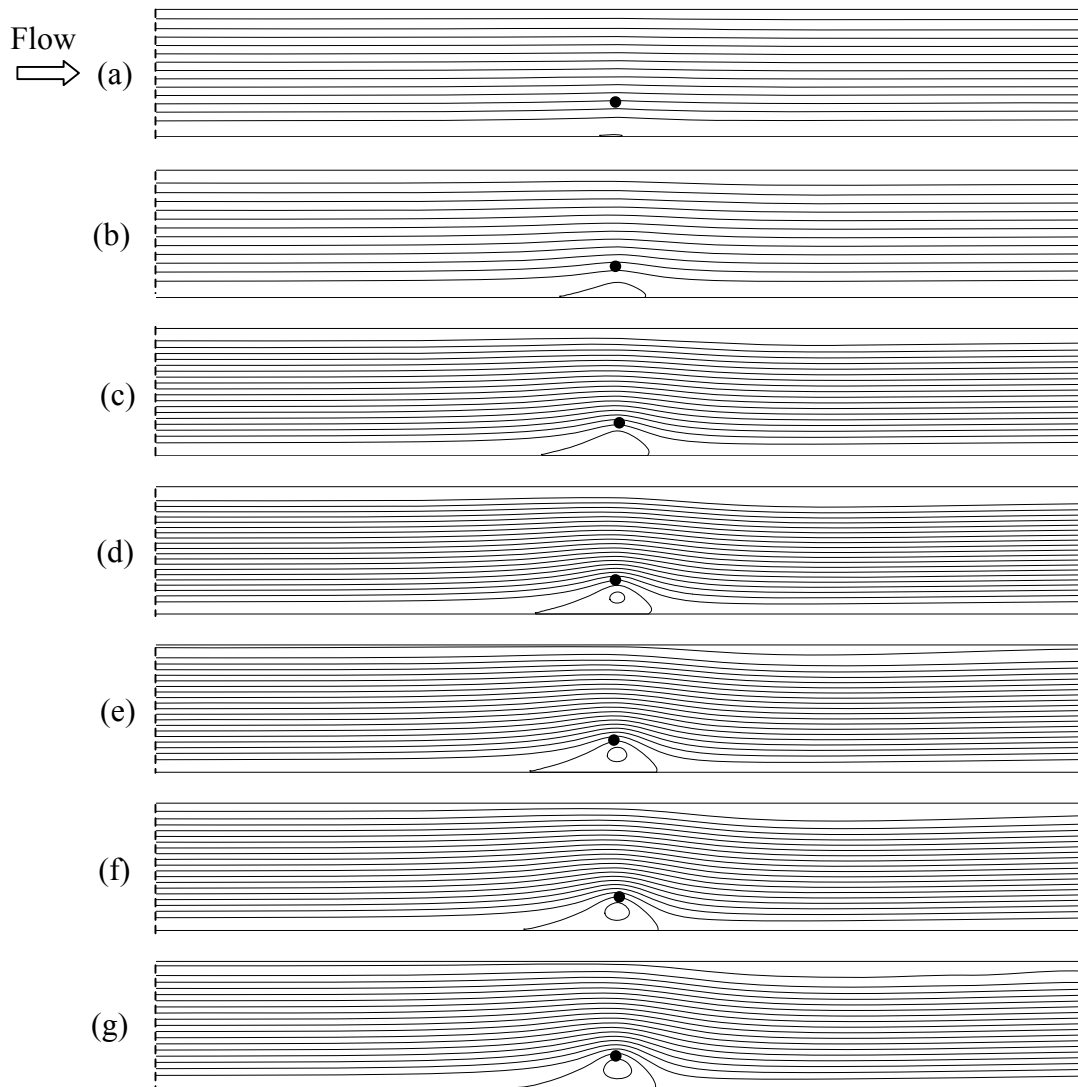


Figure 3.26 Variation of flow fields with applied voltage ($u_i = 1.0$ m/s)

- (a) $V_0 = 14$ kV, $\Psi_{\max} = 0.70$, $\Psi_{\min} = 0.0$, $\Delta \Psi = 0.05$
- (b) $V_0 = 15$ kV, $\Psi_{\max} = 0.30$, $\Psi_{\min} = -0.005$, $\Delta \Psi = 0.02$
- (c) $V_0 = 16$ kV, $\Psi_{\max} = 0.10$, $\Psi_{\min} = -0.005$, $\Delta \Psi = 0.005$
- (d) $V_0 = 17$ kV, $\Psi_{\max} = 0.055$, $\Psi_{\min} = -0.005$, $\Delta \Psi = 0.0025$
- (e) $V_0 = 18$ kV, $\Psi_{\max} = 0.055$, $\Psi_{\min} = -0.005$, $\Delta \Psi = 0.0025$
- (f) $V_0 = 19$ kV, $\Psi_{\max} = 0.050$, $\Psi_{\min} = -0.005$, $\Delta \Psi = 0.0025$
- (g) $V_0 = 20$ kV, $\Psi_{\max} = 0.050$, $\Psi_{\min} = -0.005$, $\Delta \Psi = 0.0025$

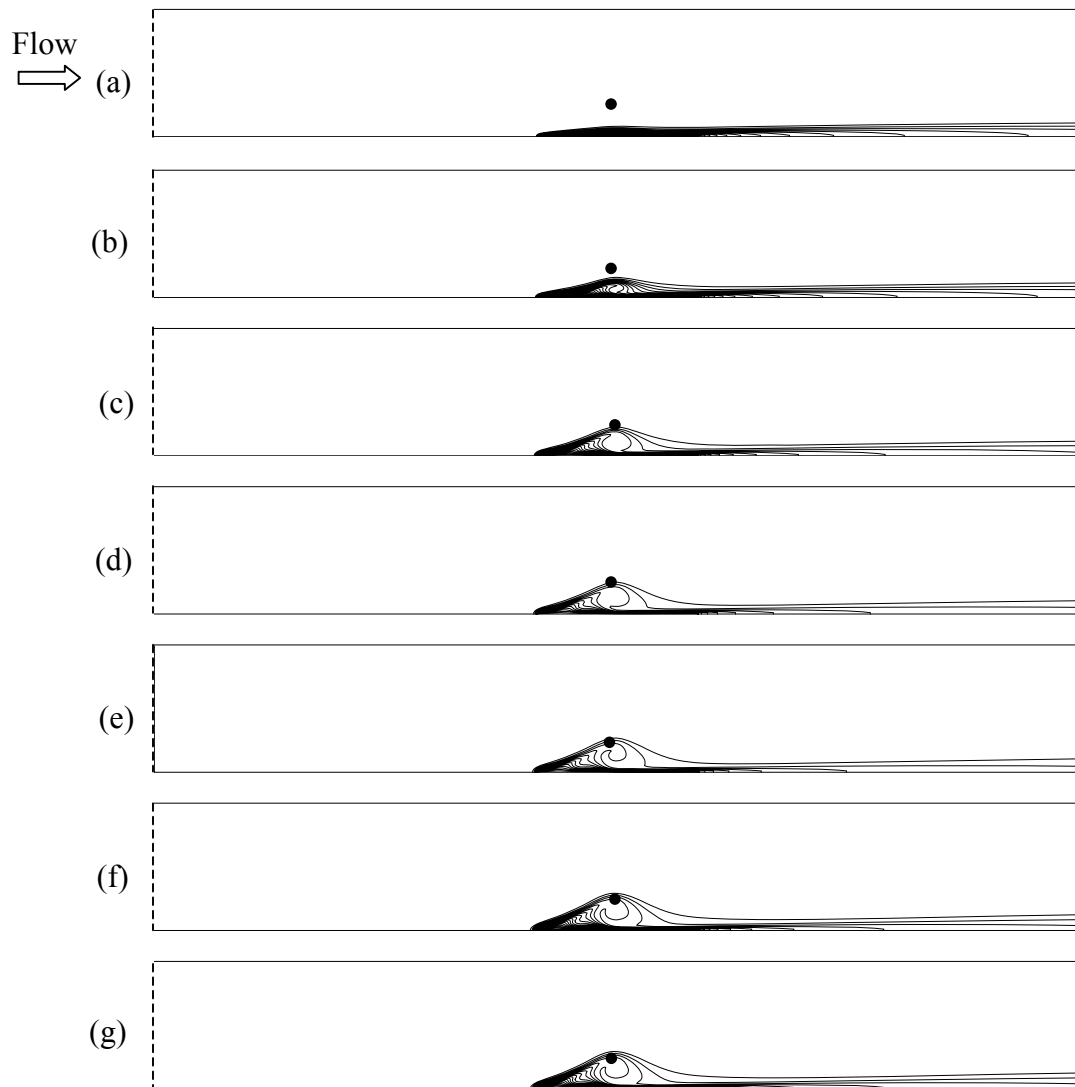


Figure 3.27 Variation of concentration fields with applied voltage
 ($u_i = 1.0$ m/s, $C_{\max} = 1.0$, $C_{\min} = 0.0$, $\Delta C = 0.05$)
 (a) $V_0 = 14$ kV, (b) $V_0 = 15$ kV, (c) $V_0 = 16$ kV, (d) $V_0 = 17$ kV,
 (e) $V_0 = 18$ kV, (f) $V_0 = 19$ kV, (g) $V_0 = 20$ kV

CHAPTER FOUR

CONCLUSIONS

The present study has addressed some fundamental questions involved in the EHD-enhanced heat and mass transfer. Particularly, the present results have once again confirmed that an electric field can significantly enhance heat and mass transfer. The important conclusions from the present study are summarized in the following sections.

4.1 EHD-enhanced Heat Transfer

Corona discharge is found to be an effective method for heat transfer enhancement. For forced convection, the enhancement increases with the applied voltage and can be as high as 350% from the present results. Although two different approaches (one-way and two-way coupling) were used to determine the interactions between the electric and flow fields, their differences are usually negligible. The results thus justify the use of one-way coupling in the earlier studies. Further analysis shows that the ion drift velocity is typically two-orders of magnitude larger than the inlet air velocity, which also lends support to the formulation based on one-way coupling. Most importantly, both numerical approaches predict the existence of oscillatory flows, which is the main mechanism for the high heat transfer enhancement.

For natural convection, the heat transfer enhancement is most notable at low Rayleigh numbers. Although the heat transfer enhancement may be quite impressive at low Rayleigh numbers ($Ra \leq 10^5$), one should be cautious that the added thermal energy from the electric field (i.e., Joule heating) may have contributes greatly to this heat transfer enhancement. On the other hand, the effects of Joule heating are negligible when the Rayleigh number is large ($Ra > 10^5$). This is because the added electric energy is

small as compared with the thermal energy provided by the differentially heated walls. The present study has an important implication for the experimental study of EHD-enhanced natural convection. When evaluating the heat transfer enhancement at low Rayleigh numbers, it is important to distinguish the various components which contribute to the heat transfer enhancement. Claims of unrealistic heat transfer enhancement may result if care is not taken.

4.2 EHD-enhanced Mass Transfer

Both experimental and numerical studies have been conducted to verify the effectiveness of electric field in the enhancement of water evaporation. The effects of corona wind, corona polarity, and cross-flow on the evaporation rate have been studied experimentally. The water evaporation rate is shown to depend on the strength of the electric field and the velocity of the airflow. In the absence of cross-flow, the enhancement in water evaporation rate increases linearly with the applied voltage. When a large volume of cross-flow is introduced over the water surface, the electric field becomes insignificant on the water evaporation enhancement. This is due to the suppression of the corona wind by the cross-flow.

A numerical study was conducted to investigate the water evaporation enhanced by electric field and cross-flow with positive discharge. The results show that with a weak cross-flow, the water evaporation can be enhanced greatly compared with that in the absence of cross-flow. If the velocity of the cross-flow is too high, it may diminish the effect of electric field. Also, the results are compared with those of the experiments. In general, the agreement between these results is quite satisfactory.

4.3 Recommendations for Future Study

Although the present study has examined some fundamental issues involved in the EHD-enhanced heat and mass transfer, there are problems remained to be explored. For example, some studies can be extended directly from the present work to further improve our understanding of the EHD-enhanced heat and mass transfer. These possible topics are discussed below.

1. Although both corona polarities (positive and negative) were employed in the present experimental study, only positive corona discharge was considered in the present numerical study. One can extend the present study to include negative corona discharge in the future numerical work. However, before taking on this problem, one needs to know the difference in the nature of corona discharge. As it is well-known that positive corona discharge is more stable and uniformly distributed along the wire electrode. As such, it can be adequately modeled as two-dimensional. On the other hand, negative corona discharge usually less stable and it promotes turbulence. Thus, a two-dimensional, laminar flow model is not appropriate for negative corona discharge. To catch all the essences of physics involved in negative corona discharge, one may have to employ three-dimensional turbulent flow model.

2. Although the present study has employed a fine wire as the electrode, other studies have used a needle as the electrode [26], which also proves to be an effective means. When considering a needle electrode in numerical study, one needs to employ a three-dimensional model. This is mainly due to the difference in the flow profile of corona wind. For a wire electrode, it produces corona wind similar to a slot jet so that it can be adequately modeled as two-dimensional. On the other hand, for a needle

electrode, it produces corona wind similar to a round jet, which is inherently three-dimensional. As such, an extension from the present study to include needle electrode will require a three-dimensional model.

3. It has been proven that electric field in the form of corona wind can significantly enhance the drying rate of wet materials. In general, all wetted materials can be considered as porous media fully or partially saturated with water. Water inside a porous medium exists in two forms; free water and bound water [47]. Free water exists between the solid cells and can be released when freezing occurs. Bound water is the water held within the solid cell wall and cannot be released if freezing occurs in the intercellular space. The present study of EHD-enhanced water evaporation can be regarded as a special case of the EHD-enhanced drying as there is no solid constituent involved. As such, the present study has only addressed the effectiveness of corona discharge on the removal of free water. For a complete understanding of the mechanisms involved in the EHD-enhanced drying, the removal of bound water by corona discharge needs to be addressed. While the experimental evaluation of the above problem may be straightforward, the numerical study will be rather challenging. Due to the presence of solid constituent, not only the calculation of electric field will become more complicated, but also the calculation of the flow and concentration fields will be more involved.

REFERENCES

1. Chang, J.-S., Kelly, A. J., and Crowley, J. M., 1995, *Handbook of Electrostatic Processes*, Marcel Dekker, New York.
2. Lykoudis, P. S., and Yu, C. P., 1962, "The Influence of Electrostrictive Forces in Natural Thermal Convection," *International Journal of Heat and Mass Transfer*, Vol. 6, pp. 853-862.
3. Macro, S. M., and Velkoff, H. R., 1963, "Effect of Electrostatic Fields on Free Convection Heat Transfer from Flat Plates," ASME Paper No. 63-HT-9.
4. Franke, M. E., 1969, "Effect of Vortices Induced by Corona Discharge on Free Convection Heat Transfer from a Vertical Plate," *Journal of Heat Transfer*, Vol. 91, pp. 427-433.
5. Yabe, A., Mori, Y., and Hijitata, K., 1978, "EHD Study of the Corona Wind between Wire and Plate Electrodes," *AIAA Journal*, Vol. 16, pp. 340-345.
6. Franke, M. E. and Huston, K. E., 1982, "Effect of Corona Discharge on the Free Convection Heat Transfer inside a Vertical Hollow Cylinder," ASME Paper, No. 82 WA/HT-20.
7. Liu, K. S., and Lai, F. C., 1997, "Effects of Electrode Location on EHD-Enhanced Natural Convection in an Enclosure," *Proceedings of the 1997 National Heat Transfer Conference*, Vol. 8 (HTD-Vol. 346), pp. 23-32.
8. Tan, K. T., and Lai, F. C., 2001, "EHD-Enhanced Natural Convection in an Enclosure: Effects of Non-Symmetric Electric Field," *Proceedings of the 2001 National Heat Transfer Conference (CD-ROM)*, NHTC2001-20065.
9. Ngo, C. C., and Lai, F. C., 2001, "Effects of Electric Field on Natural Convection in an Enclosure Heated from Below," *Proceedings of the 2001 National Heat Transfer Conference*, (CD-ROM), NHTC2001-20200.
10. Yamamoto, T., and Velkoff, H. R., 1981, "Electrohydrodynamics in an Electrostatic Precipitator," *Journal of Fluid Mechanics*, Vol. 108, pp. 1-8.
11. Tada, Takimoto, A., Ueda, D., and Hayashi, Y., 1991, "Heat Transfer Enhancement in a Convective Field with Corona Discharge," *Transactions of the Japan Society of Mechanical Engineers, Part B*, Vol. 57, No. 533, pp. 217-228.
12. Kulkarni, S. S., and Lai, F. C., 1995, "Effects of Electric Field on Mixed Convection in a Vertical Channel," *Proceedings of the 1995 National Heat Transfer Conferences*, Vol. 8, pp. 59-67.

13. Mathew, J., and Lai, F. C., 1995, "Enhanced Heat Transfer in a Horizontal Channel with Double Electrodes," *Conference Record of the 1995 IEEE Industry Applications Society 30th Annual Meeting*, Vol. 2, pp. 1472-1479.
14. Owsenek, B. L., and Seyed-Yagoobi, J., 1997, "Theoretical and Experimental Study of Electrohydrodynamic Heat Transfer Enhancement through Wire-Plate Corona Discharge," *Journal of Heat Transfer*, Vol. 119, pp. 604-610.
15. Kulacki, F. A. and Daubenmier, J. A., 1978, "A Preliminary Study of Electrohydrodynamic Augmented Baking," *Journal of Electrostatics*, Vol. 5, pp. 325-336.
16. Kirschvink-Kobayashi, A. and Kirschvink, J. L., 1986, "Electrostatic Enhancement of Industrial Drying Process," *Industrial & Engineering Chemistry Process Design and Development*, Vol. 25, pp. 1027.
17. Chen, Y. H. and Barthakur, N. N., 1991, "Potato Slab Dehydration by Air Ions from Corona Discharge", *International Journal of Biometeorology*, Vol. 35, pp. 67-70.
18. Hashinaga, F., Bajgai, T.R., Isobe, S., and Barthakur, N. N., 1999, "EHD Drying of Apple Slices," *Drying Technology*, Vol.17, NO. 3, pp. 479-495.
19. Carlon, H.R. and Latham, J., 1992, "Enhanced Drying Rates of Wetted Materials in Electric Fields," *Journal of Atmospheric and Terrestrial Physics*, Vol. 54, pp. 117-118.
20. Banarjee, S. and Law, S.E., 1998, "Electroosmotically Enhanced Drying of Biomass," *IEEE Transaction on Industry Application*, Vol. 34, No. 5, pp. 992-999.
21. Sadek, S. E., Fax, R. G., and Hurwitz, M., 1972, "The Influence of Electric Fields on Convective Heat and Mass Transfer from a Horizontal Surface under Forced Convection," *Journal of Heat Transfer*, Vol. 94, No. 2, pp. 144-148.
22. Wolny, A., 1992, "Intensification of the Evaporation Process by Electric Field," *Chemical Engineering Science*, Vol. 47, No. 3, pp. 551-554.
23. Wolny, A. and Kaniuk, R., 1996, "The Effect of Electric Field on Heat and Mass Transfer," *Drying Technology*, Vol. 14, No. 2, pp. 195-216.
24. Barthakur, N. N. and Arnold, N. P., 1995, "Evaporation Rate Enhancement of Water with Air Ions from a Corona Discharge," *International Journal of Biometeorology*, Vol. 39, pp. 29-33.

25. Lai, F. C. and Lai, K. W., 2002, "EHD-Enhanced Drying with Wire Electrode," *Drying Technology*, Vol. 20, No. 7, pp. 1389-1401.
26. Lai, F. C. and Wong, D. S., 2003, "EHD-Enhanced Drying with Needle Electrode," *Drying Technology*, Vol. 21, pp. 1291-1306.
27. Pollard, T. Smith, Cotton, J. S., 2003, "Numerical Simulation of Electric Field Distributions in Electrohydrodynamic Two-phase Flow Regimes," *IEEE Transactions on Dielectrics and Electrical Insulation*, Vol. 10, No. 1, pp. 37-51
28. Cotton, J. S., Chang, J. S., Shoukri, M., and Smith-Pollard, T., 2002, "Electrohydrodynamically Enhanced Flow Boiling in an Eccentric Horizontal Cylindrical Channel," *Conference on Electrical Insulation and Dielectric Phenomena, Annual Report*, pp. 220-223.
29. Cotton, J. S., Brocilo, D., Shoukri, M. M., Smith-Pollard, T., and Chang, J. S., 1998, "Mechanisms of Electrohydrodynamic Flow Boiling Heat Transfer in Coaxial Flow Channels of Dielectric Refrigerant R-134a," *Conference on Electrical Insulation and Dielectric Phenomena (CEIDP), Annual Report*, Vol. 1, pp. 178-181.
30. Seyed-Yagoobi, J., and Bryan, J. E., 1999, "Enhancement of Heat and Mass Transport in Single-Phase and Two-Phase Flows with Electrohydrodynamics," *Advances in Heat Transfer*, Vol. 33, pp. 95-186, Academic Press, New York.
31. Lomax, H., 2001, *Fundamentals of Computational Fluid Dynamics*, Springer, New York.
32. Kakac, S., and Yener, Y., 1995, *Convective Heat Transfer*, CRC Press, Inc.
33. Incropera, F. P., and DeWitt, D. P., 2001, *Fundamentals of Heat and Mass Transfer*, fifth edition, John Wiley, New York.
34. Shah, R. K., and London, A. L., 1978, "Laminar Flow Forced Convection in Ducts," *Supplement 1, Advanced in Heat Transfer*, Academic Press, New York.
35. Lai, F. C., McKinney, P. J., and Davidson, J. H., 1995, "Oscillatory Electrohydrodynamic Gas Flows," *Journal of Fluids Engineering*, Vol. 117, pp. 491-497.
36. Davidson, J. H., Kulacki, F. A., and Dunn, P. F., 1987, Convective Heat Transfer with Electric and Magnetic Field, *Handbook of Single-Phase Convective Heat Transfer*, S. Kakaç, R. K. Shah, and W. Aung, ed., Chapter 9, John Wiley, New York.

37. Berkovsky, B. M., and Polevikov, V. K., 1986, "Numerical Study of Problems on High-Intensive Free Convection," *Heat Transfer and Turbulent Buoyant Convection*, D. B. Spalding, and N. Afgan, ed., Hemisphere, Washington, DC, pp. 443-455.
38. Bejan, A., 2004, *Convection Heat Transfer*, third edition, John Wiley, New York, pp. 524-526.
39. Fuller, E. N., Schettler, P. D., and Giddins, J. C., 1966, "A New Method for Prediction of Binary Gas-phase Diffusion Coefficients", *Industrial and Engineering Chemistry*, Vol. 58, No. 5, pp.19-27.
40. Cengel, Y. A., and Boles, M. A., 1998, *Thermodynamics*, third edition, McGraw-Hill, New York.
41. Lamb, D. W., and Woolsey, G. A., 1995, "Characterization and Use of an Optical-Fiber Interferometer for Measurement of the Electric Wind," *Applied Optics*, Vol. 34, No. 9, pp. 1608-1616.
42. Demarest, K. R., 1998, *Engineering Electromagnetics*, Pearson Education, New York.
43. Chari, M. V. K, Salon, S. J, 2000, *Numerical Method in Electromagnetism*, Academic Press, New York.
44. Zhou, P.-B., 1993, *Numerical Analysis of Electromagnetic Fields*, Springer-Verlag, New York.
45. Lide, D. R., 1995, *Handbook of Chemistry and Physics 1913-1995*, CRC Press, Boca Raton, FL.
46. Cobine, J. D., 1941, *Gaseous Conductor*, McGraw-Hill, New York
47. Keey, R. B., 1972, *Drying: Principles and Practice*, Pergamon Press, New York.

APPENDIX A

FLOW AND TEMPERATURE FIELDS FOR ONE-WAY AND TWO-WAY COUPLING MODELS

Table A.1 Comparison of Nusselt numbers obtained from both one-way and two-way coupling models ($V_0 = 10.0$ kV).....	112
Table A.2 Comparison of Nusselt numbers obtained from both one-way and two-way coupling models ($V_0 = 12.5$ kV).....	113
Table A.3 Comparison of Nusselt numbers obtained from both one-way and two-way coupling models ($V_0 = 17.5$ kV).....	114
Figure A.1 Flow fields predicted by one-way coupling model for $V_0 = 15$ kV, $Re = 150$	115
Figure A.2 Flow fields predicted by two-way coupling model for $V_0 = 15$ kV, $Re = 150$	115
Figure A.3 Temperature fields predicted by one-way coupling model for $V_0 = 15$ kV, $Re = 150$	116
Figure A.4 Temperature fields predicted by two-way coupling model for $V_0 = 15$ kV, $Re = 150$	116
Figure A.5 Flow fields predicted by one-way coupling model for $V_0 = 15$ kV, $Re = 300$	117
Figure A.6 Flow fields predicted by two-way coupling model for $V_0 = 5$ kV, $Re = 300$	117
Figure A.7 Temperature fields predicted by one-way coupling model for $V_0 = 15$ kV, $Re = 300$	118
Figure A.8 Temperature fields predicted by two-way coupling model for $V_0 = 15$ kV, $Re = 300$	118
Figure A.9 Flow fields predicted by one-way coupling model for $V_0 = 17.5$ kV, $Re = 150$	119
Figure A.10 Flow fields predicted by two-way coupling model for $V_0 = 17.5$ kV, $Re = 150$	119

Figure A.11	Temperature fields predicted by one-way coupling model for $V_0 = 17.5$ kV, Re = 150.....	120
Figure A.12	Temperature fields predicted by two-way coupling model for $V_0 = 17.5$ kV, Re = 150.....	120
Figure A.13	Flow fields predicted by one-way coupling model for $V_0 = 17.5$ kV, Re = 300.....	121
Figure A.14	Flow fields predicted by two-way coupling model for $V_0 = 17.5$ kV, Re = 300.....	121
Figure A.15	Temperature fields predicted by one-way coupling model for $V_0 = 17.5$ kV, Re = 300.....	122
Figure A.16	Temperature fields predicted by two-way coupling model for $V_0 = 17.5$ kV, Re = 300.....	122
Figure A.17	Flow fields predicted by one-way coupling model for $V_0 = 17.5$ kV, Re = 450.....	123
Figure A.18	Flow fields predicted by two-way coupling model for $V_0 = 17.5$ kV, Re = 450.....	123
Figure A.19	Temperature fields predicted by one-way coupling model for $V_0 = 17.5$ kV, Re = 450.....	124
Figure A.20	Temperature fields predicted by two-way coupling model for $V_0 = 17.5$ kV, Re = 450.....	124
Figure A.21	Flow fields predicted by one-way coupling model for $V_0 = 17.5$ kV, Re = 600.....	125
Figure A.22	Flow fields predicted by two-way coupling model for $V_0 = 17.5$ kV, Re = 600.....	125
Figure A.23	Temperature fields predicted by one-way coupling model for $V_0 = 17.5$ kV, Re = 600.....	126
Figure A.24	Temperature fields predicted by two-way coupling model for $V_0 = 17.5$ kV, Re = 600.....	126
Figure A.25	Flow fields predicted by one-way coupling model for $V_0 = 17.5$ kV, Re = 750.....	127

Figure A.26	Flow fields predicted by two-way coupling model for $V_0 = 17.5$ kV, Re = 750.....	127
Figure A.27	Temperature fields predicted by one-way coupling model for $V_0 = 17.5$ kV, Re = 750.....	128
Figure A.28	Temperature fields predicted by two-way coupling model for $V_0 = 17.5$ kV, Re = 750.....	128
Figure A.29	Flow fields predicted by one-way coupling model for $V_0 = 17.5$ kV	129
Figure A.30	Flow fields predicted by two-way coupling model for $V_0 = 17.5$ kV	129
Figure A.31	Temperature fields predicted by one-way coupling model for $V_0 = 17.5$ kV	130
Figure A.32	Temperature fields predicted by two-way coupling model for $V_0 = 17.5$ kV	130

Table A.1 Comparison of Nusselt numbers obtained from both one-way and two-way coupling models ($V_0 = 10.0$ kV)

$V_0 = 10.0$ kV			$I_{exp} = 3.4e-5$ A									
Cross-flow Velocity m/s	Re Number	Forced Convection Nu Number	EHD-enhanced Forced Convection									
			One-way Coupling Model					Two-way Coupling Model				
			Nu Number			Stability	Period	Nu Number			Stability	Period
			Nu _{min.}	Nu _{average}	Nu _{max.}			Nu _{min.}	Nu _{average}	Nu _{max.}		
0.0759	150	14.60	25.37	26.54	27.43	Periodic	2.0	24.89	26.78	28.00	Periodic	2.0
0.1518	300	18.32		24.13		Steady			23.99		Steady	
0.2277	450	21.07		24.78		Steady			24.70		Steady	
0.3036	600	23.40		25.50		Steady			25.45		Steady	
0.3795	750	25.48		26.48		Steady			26.44		Steady	
0.4554	900	27.10		27.81		Steady			27.77		Steady	
0.5313	1050	28.65		29.22		Steady			29.18		Steady	
0.6072	1200	30.06		30.56		Steady			30.52		Steady	
0.9108	1800	34.80		35.08		Steady			35.05		Steady	
1.2144	2400	38.50		38.65		Steady			38.61		Steady	

Table A.2 Comparison of Nusselt numbers obtained from both one-way and two-way coupling models ($V_0 = 12.5$ kV)

$V_0 = 12.5$ kV			$I_{exp} = 8.8e-5$ A									
Cross-flow Velocity m/s	Re Number	Forced Convection Nu Number	EHD-enhanced Forced Convection									
			One-way Coupling Model					Two-way Coupling Model				
			Nu Number			Stability	Period	Nu Number			Stability	Period
			Nu _{min.}	Nu _{average}	Nu _{max.}			Nu _{min.}	Nu _{average}	Nu _{max.}		
0.0759	150	14.60		37.50		Steady			37.43		Steady	
0.1518	300	18.32	33.19	37.82	41.51	Periodic	2.2	34.45	39.05	43.29	Periodic	2.2
0.2277	450	21.07		31.04		Steady			30.92		Steady	
0.3036	600	23.40		31.51		Steady			31.43		Steady	
0.3795	750	25.48		31.94		Steady			31.89		Steady	
0.4554	900	27.10		32.33		Steady			32.29		Steady	
0.5313	1050	28.65		32.69		Steady			32.69		Steady	
0.6072	1200	30.06		33.12		Steady			33.11		Steady	
0.9108	1800	34.80		36.13		Steady			36.09		Steady	
1.2144	2400	38.50		39.46		Steady			39.42		Steady	

Table A.3 Comparison of Nusselt numbers obtained from both one-way and two-way coupling models ($V_0 = 17.5$ kV)

Voltage = 17.5 kV								$I_{exp} = 2.48e-4$ A				
Cross-flow Velocity m/s	Re Number	Forced Convection Nu Number	EHD-enhanced Forced Convection									
			One-way Coupling Model					Two-way Coupling Model				
			Nu Number			Stability	Period	Nu Number			Stability	Period
			Nu _{min.}	Nu _{average}	Nu _{max.}			Nu _{min.}	Nu _{average}	Nu _{max.}		
0.0759	150	14.60	43.09	50.87	58.62	Periodic	1.7	41.83	50.73	61.73	Periodic	1.6
0.1518	300	18.32	40.44	46.46	54.28	Periodic	3.0	39.29	47.02	57.86	Periodic	2.9
0.2277	450	21.07	52.14	58.58	64.98	Periodic	2.0	52.86	58.99	65.15	Periodic	1.9
0.3036	600	23.40	47.84	52.31	57.50	Periodic	2.3	48.32	52.93	58.30	Periodic	2.4
0.3795	750	25.48	41.99	42.95	44.18	Periodic	3.0	42.28	43.28	44.60	Periodic	3.0
0.4554	900	27.10		40.98		Steady			41.07		Steady	
0.5313	1050	28.65		41.57		Steady			41.46		Steady	
0.6072	1200	30.06		41.68		Steady			41.72		Steady	
0.9108	1800	34.80		42.40		Steady			42.43		Steady	
1.2144	2400	38.50		43.18		Steady			43.20		Steady	

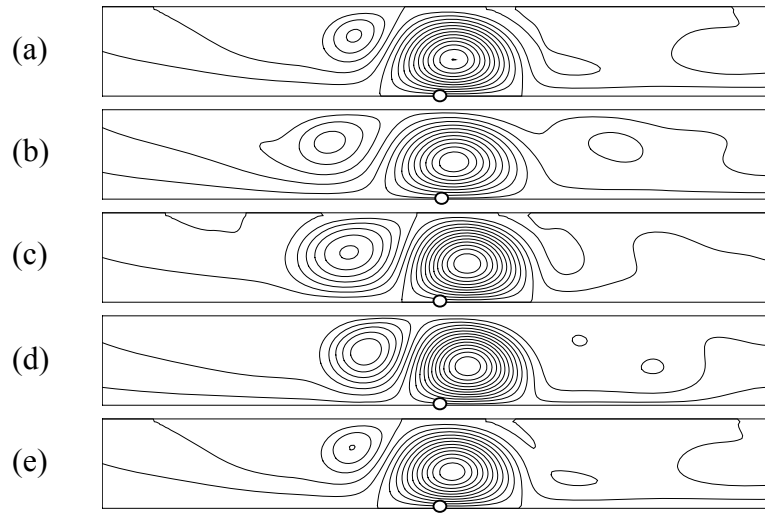


Figure A.1 Flow fields predicted by one-way coupling model for $V_0 = 15$ kV, $Re = 150$

- (a) $\tau = 55.1$, $\Psi_{\max} = 2.5$, $\Psi_{\min} = -5.5$, $\Delta\Psi = 0.5$
- (b) $\tau = 55.6$, $\Psi_{\max} = 2.7$, $\Psi_{\min} = -4.7$, $\Delta\Psi = 0.5$
- (c) $\tau = 56.1$, $\Psi_{\max} = 3.5$, $\Psi_{\min} = -5.5$, $\Delta\Psi = 0.5$
- (d) $\tau = 56.6$, $\Psi_{\max} = 3.8$, $\Psi_{\min} = -5.8$, $\Delta\Psi = 0.5$
- (e) $\tau = 57.1$, $\Psi_{\max} = 2.5$, $\Psi_{\min} = -5.5$, $\Delta\Psi = 0.5$

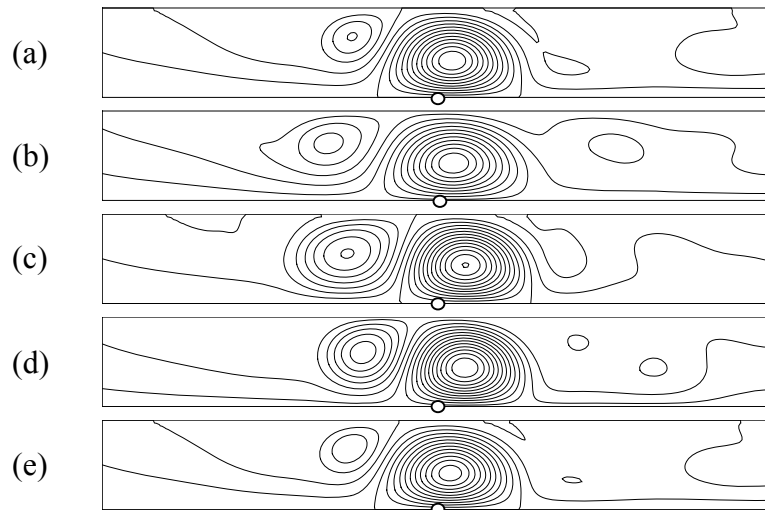


Figure A.2 Flow fields predicted by two-way coupling model for $V_0 = 15$ kV, $Re = 150$

- (a) $\tau = 56.6$, $\Psi_{\max} = 2.5$, $\Psi_{\min} = -5.5$, $\Delta\Psi = 0.5$
- (b) $\tau = 57.1$, $\Psi_{\max} = 2.6$, $\Psi_{\min} = -4.6$, $\Delta\Psi = 0.5$
- (c) $\tau = 57.6$, $\Psi_{\max} = 3.6$, $\Psi_{\min} = -5.6$, $\Delta\Psi = 0.5$
- (d) $\tau = 58.1$, $\Psi_{\max} = 3.8$, $\Psi_{\min} = -5.8$, $\Delta\Psi = 0.5$
- (e) $\tau = 58.6$, $\Psi_{\max} = 2.5$, $\Psi_{\min} = -5.5$, $\Delta\Psi = 0.5$

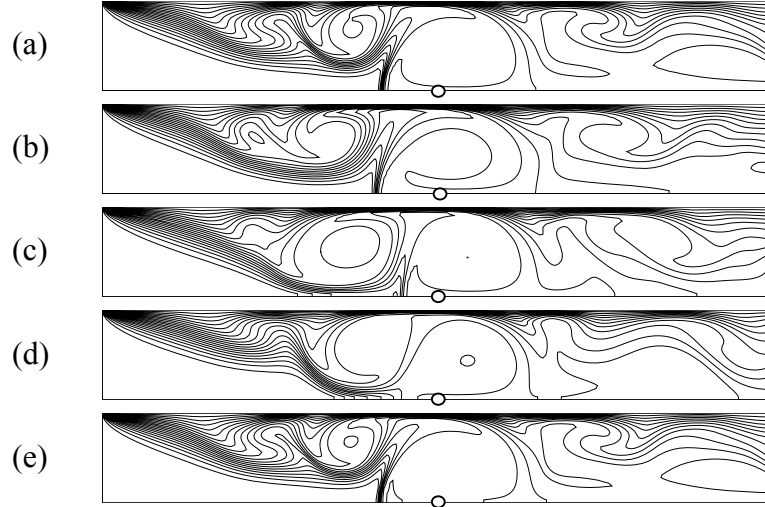


Figure A.3 Temperature fields predicted by one-way coupling model for $V_0 = 15$ kV,
 $Re = 150$

- (a) $\tau = 55.1, \theta_{\max} = 1.0, \theta_{\min} = 0.0, \Delta\theta = 0.05$
- (b) $\tau = 55.6, \theta_{\max} = 1.0, \theta_{\min} = 0.0, \Delta\theta = 0.05$
- (c) $\tau = 56.1, \theta_{\max} = 1.0, \theta_{\min} = 0.0, \Delta\theta = 0.05$
- (d) $\tau = 56.6, \theta_{\max} = 1.0, \theta_{\min} = 0.0, \Delta\theta = 0.05$
- (e) $\tau = 57.1, \theta_{\max} = 1.0, \theta_{\min} = 0.0, \Delta\theta = 0.05$

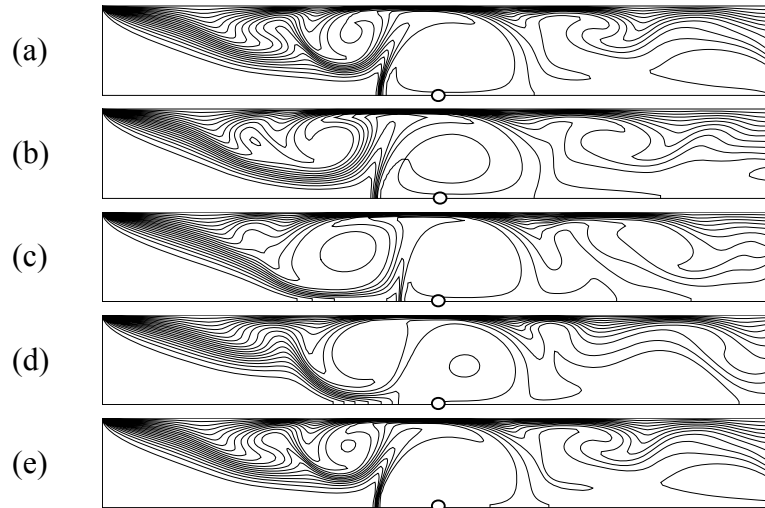


Figure A.4 Temperature fields predicted by two-way coupling model for $V_0 = 15$ kV,
 $Re = 150$

- (a) $\tau = 56.6, \theta_{\max} = 1.0, \theta_{\min} = 0.0, \Delta\theta = 0.05$
- (b) $\tau = 57.1, \theta_{\max} = 1.0, \theta_{\min} = 0.0, \Delta\theta = 0.05$
- (c) $\tau = 57.6, \theta_{\max} = 1.0, \theta_{\min} = 0.0, \Delta\theta = 0.05$
- (d) $\tau = 58.1, \theta_{\max} = 1.0, \theta_{\min} = 0.0, \Delta\theta = 0.05$
- (e) $\tau = 58.6, \theta_{\max} = 1.0, \theta_{\min} = 0.0, \Delta\theta = 0.05$

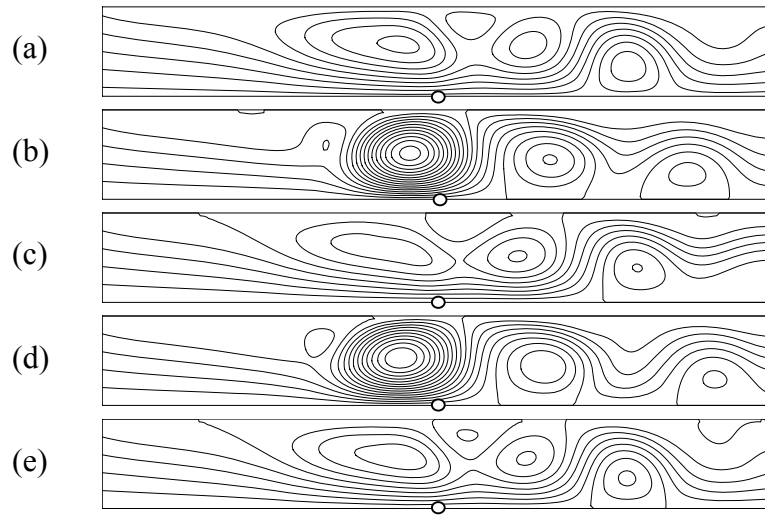


Figure A.5 Flow fields predicted by one-way coupling model for $V_0 = 15$ kV, $Re = 300$

- (a) $\tau = 102.9$, $\Psi_{\max} = 1.7$, $\Psi_{\min} = -4.3$, $\Delta\Psi = 0.2$
- (b) $\tau = 103.7$, $\Psi_{\max} = 3.2$, $\Psi_{\min} = -6.2$, $\Delta\Psi = 0.2$
- (c) $\tau = 104.5$, $\Psi_{\max} = 1.6$, $\Psi_{\min} = -4.0$, $\Delta\Psi = 0.2$
- (d) $\tau = 105.3$, $\Psi_{\max} = 3.2$, $\Psi_{\min} = -6.0$, $\Delta\Psi = 0.2$
- (e) $\tau = 106.3$, $\Psi_{\max} = 1.8$, $\Psi_{\min} = -4.4$, $\Delta\Psi = 0.2$

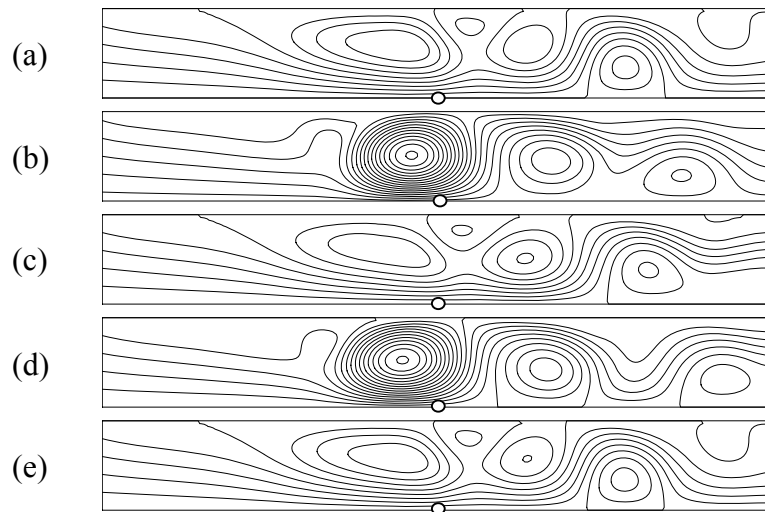


Figure A.6 Flow fields predicted by two-way coupling model for $V_0 = 5$ kV, $Re = 300$

- (a) $\tau = 101.1$, $\Psi_{\max} = 1.8$, $\Psi_{\min} = -4.8$, $\Delta\Psi = 0.2$
- (b) $\tau = 101.9$, $\Psi_{\max} = 3.3$, $\Psi_{\min} = -6.5$, $\Delta\Psi = 0.2$
- (c) $\tau = 102.7$, $\Psi_{\max} = 1.6$, $\Psi_{\min} = -4.4$, $\Delta\Psi = 0.2$
- (d) $\tau = 103.5$, $\Psi_{\max} = 3.2$, $\Psi_{\min} = -7.2$, $\Delta\Psi = 0.2$
- (e) $\tau = 104.5$, $\Psi_{\max} = 1.8$, $\Psi_{\min} = -5.0$, $\Delta\Psi = 0.2$

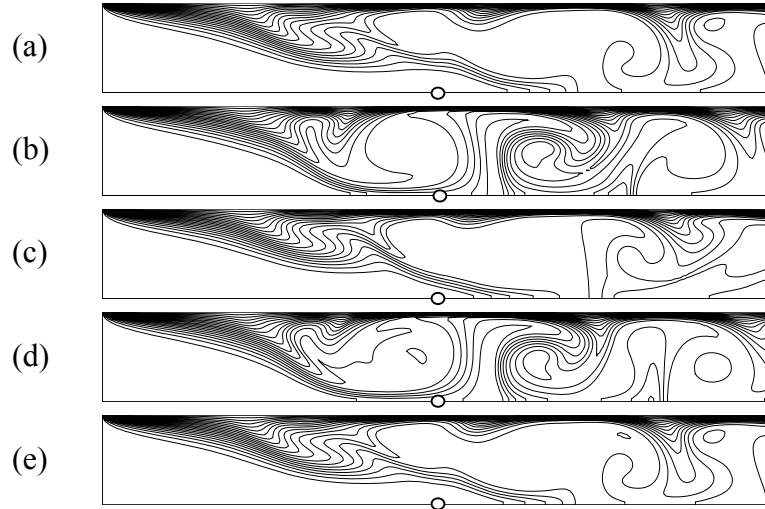


Figure A.7 Temperature fields predicted by one-way coupling model for $V_0 = 15$ kV, $Re = 300$

- (a) $\tau = 102.9$, $\theta_{\max} = 1.0$, $\theta_{\min} = 0.0$, $\Delta\theta = 0.05$
- (b) $\tau = 103.7$, $\theta_{\max} = 1.0$, $\theta_{\min} = 0.0$, $\Delta\theta = 0.05$
- (c) $\tau = 104.5$, $\theta_{\max} = 1.0$, $\theta_{\min} = 0.0$, $\Delta\theta = 0.05$
- (d) $\tau = 105.3$, $\theta_{\max} = 1.0$, $\theta_{\min} = 0.0$, $\Delta\theta = 0.05$
- (e) $\tau = 106.3$, $\theta_{\max} = 1.0$, $\theta_{\min} = 0.0$, $\Delta\theta = 0.05$

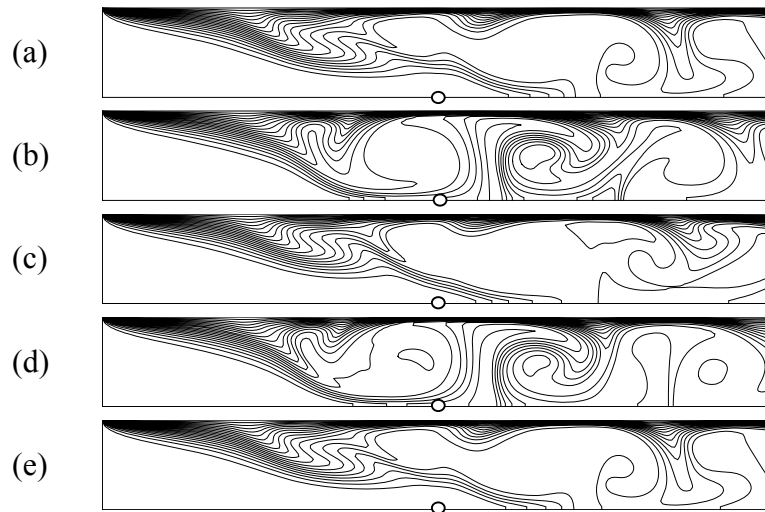


Figure A.8 Temperature fields predicted by two-way coupling model for $V_0 = 15$ kV, $Re = 300$

- (a) $\tau = 101.1$, $\theta_{\max} = 1.0$, $\theta_{\min} = 0.0$, $\Delta\theta = 0.05$
- (b) $\tau = 101.9$, $\theta_{\max} = 1.0$, $\theta_{\min} = 0.0$, $\Delta\theta = 0.05$
- (c) $\tau = 102.7$, $\theta_{\max} = 1.0$, $\theta_{\min} = 0.0$, $\Delta\theta = 0.05$
- (d) $\tau = 103.5$, $\theta_{\max} = 1.0$, $\theta_{\min} = 0.0$, $\Delta\theta = 0.05$
- (e) $\tau = 104.5$, $\theta_{\max} = 1.0$, $\theta_{\min} = 0.0$, $\Delta\theta = 0.05$

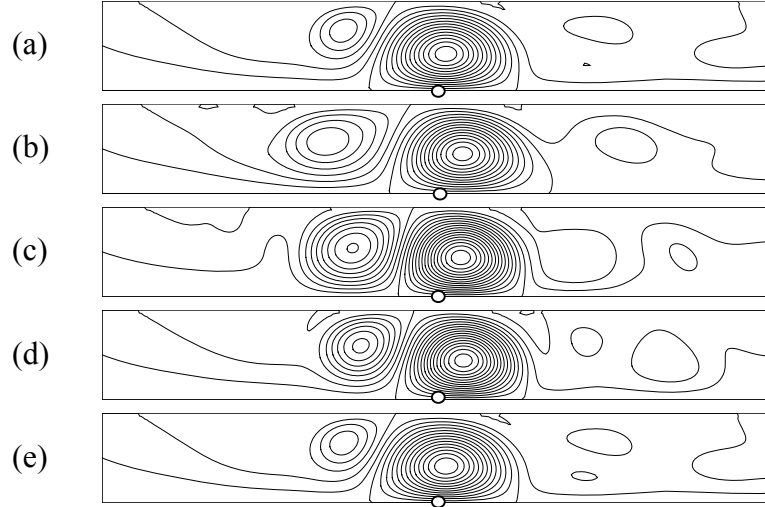


Figure A.9 Flow fields predicted by one-way coupling model for $V_0 = 17.5$ kV, $Re = 150$

- (a) $\tau = 55.1$, $\Psi_{\max} = 3.0$, $\Psi_{\min} = -6.5$, $\Delta\Psi = 0.5$
- (b) $\tau = 55.5$, $\Psi_{\max} = 3.5$, $\Psi_{\min} = -6.5$, $\Delta\Psi = 0.5$
- (c) $\tau = 55.9$, $\Psi_{\max} = 4.5$, $\Psi_{\min} = -7.5$, $\Delta\Psi = 0.5$
- (d) $\tau = 56.3$, $\Psi_{\max} = 4.5$, $\Psi_{\min} = -7.5$, $\Delta\Psi = 0.5$
- (e) $\tau = 56.8$, $\Psi_{\max} = 3.0$, $\Psi_{\min} = -6.0$, $\Delta\Psi = 0.5$

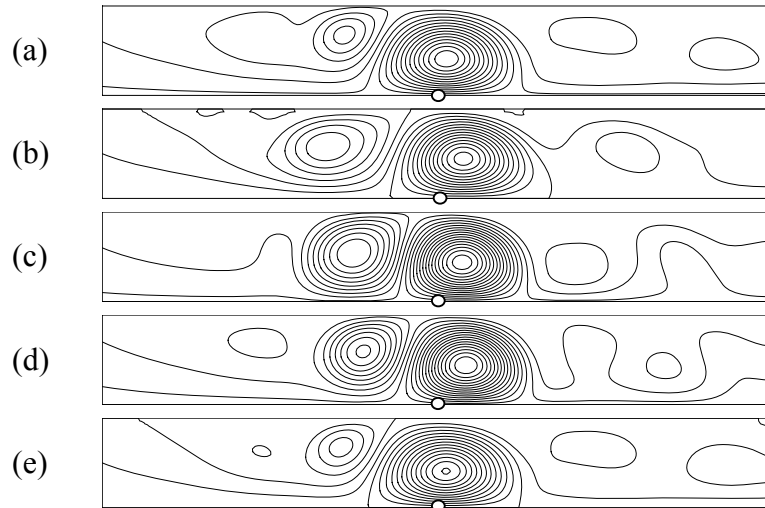


Figure A.10 Flow fields predicted by two-way coupling model for $V_0 = 17.5$ kV,
 $Re = 150$

- (a) $\tau = 55.8$, $\Psi_{\max} = 2.9$, $\Psi_{\min} = -6.4$, $\Delta\Psi = 0.5$
- (b) $\tau = 56.2$, $\Psi_{\max} = 3.5$, $\Psi_{\min} = -6.5$, $\Delta\Psi = 0.5$
- (c) $\tau = 56.6$, $\Psi_{\max} = 4.6$, $\Psi_{\min} = -7.4$, $\Delta\Psi = 0.5$
- (d) $\tau = 57.0$, $\Psi_{\max} = 4.6$, $\Psi_{\min} = -7.4$, $\Delta\Psi = 0.5$
- (e) $\tau = 57.4$, $\Psi_{\max} = 4.2$, $\Psi_{\min} = -7.3$, $\Delta\Psi = 0.5$

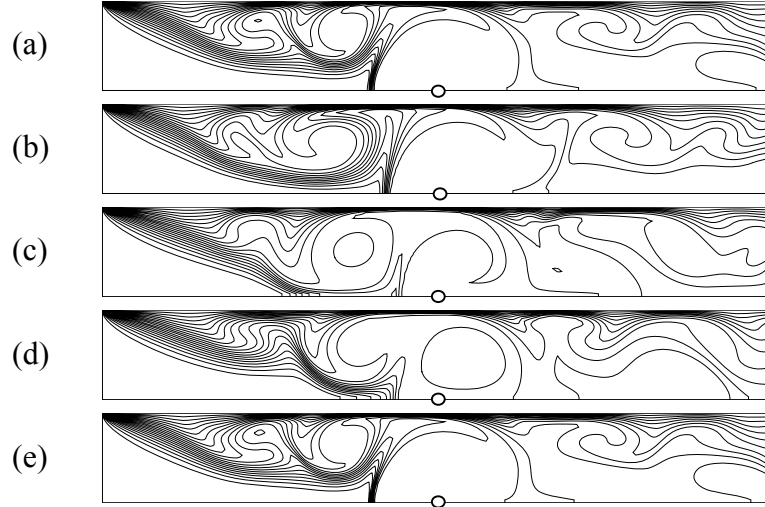


Figure A.11 Temperature fields predicted by one-way coupling model for $V_0 = 17.5$ kV,
 $Re = 150$

(a) $\tau = 55.1$, $\theta_{\max} = 1.0$, $\theta_{\min} = 0.0$, $\Delta = 0.05$

(b) $\tau = 55.5$, $\theta_{\max} = 1.0$, $\theta_{\min} = 0.0$, $\Delta = 0.05$

(c) $\tau = 55.9$, $\theta_{\max} = 1.0$, $\theta_{\min} = 0.0$, $\Delta = 0.05$

(d) $\tau = 56.3$, $\theta_{\max} = 1.0$, $\theta_{\min} = 0.0$, $\Delta = 0.05$

(e) $\tau = 56.8$, $\theta_{\max} = 1.0$, $\theta_{\min} = 0.0$, $\Delta = 0.05$

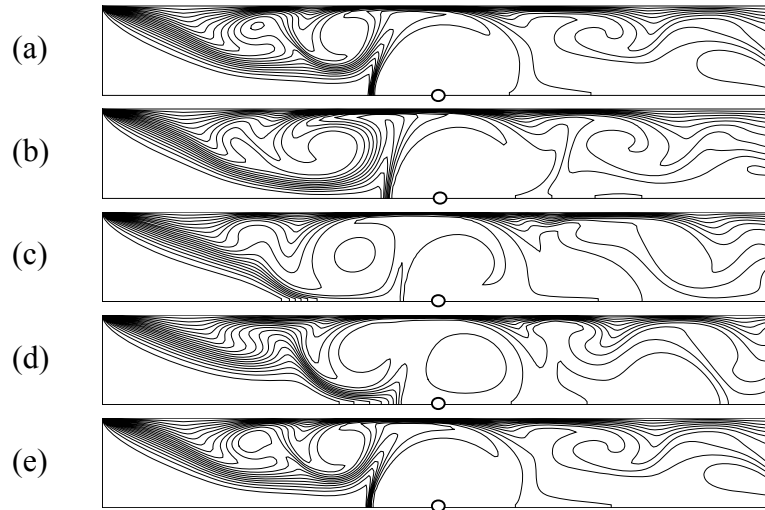


Figure A.12 Temperature fields predicted by two-way coupling model for $V_0 = 17.5$ kV,
 $Re = 150$

(a) $\tau = 55.8$, $\theta_{\max} = 1.0$, $\theta_{\min} = 0.0$, $\Delta = 0.05$

(b) $\tau = 56.2$, $\theta_{\max} = 1.0$, $\theta_{\min} = 0.0$, $\Delta = 0.05$

(c) $\tau = 56.6$, $\theta_{\max} = 1.0$, $\theta_{\min} = 0.0$, $\Delta = 0.05$

(d) $\tau = 57.0$, $\theta_{\max} = 1.0$, $\theta_{\min} = 0.0$, $\Delta = 0.05$

(e) $\tau = 57.4$, $\theta_{\max} = 1.0$, $\theta_{\min} = 0.0$, $\Delta = 0.05$

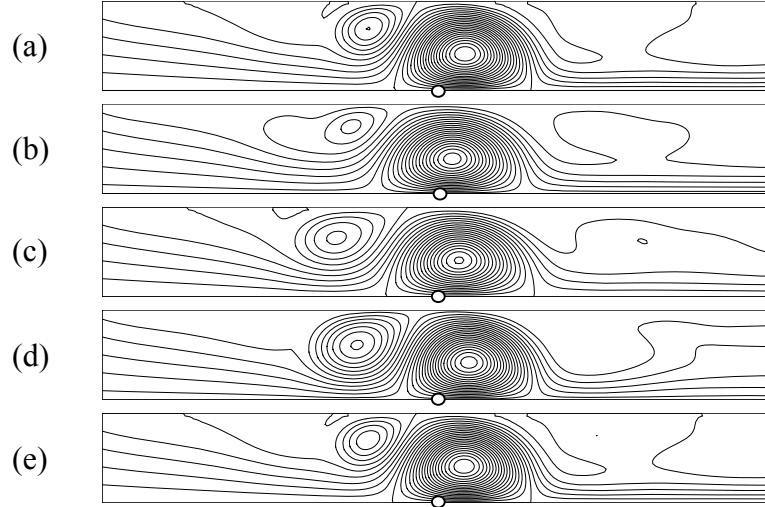


Figure A.13 Flow fields predicted by one-way coupling model for $V_0 = 17.5$ kV,
 $Re = 300$

- (a) $\tau = 56.0$, $\Psi_{\max} = 2.0$, $\Psi_{\min} = -3.6$, $\Delta\Psi = 0.2$
- (b) $\tau = 56.7$, $\Psi_{\max} = 1.5$, $\Psi_{\min} = -3.3$, $\Delta\Psi = 0.2$
- (c) $\tau = 57.4$, $\Psi_{\max} = 1.8$, $\Psi_{\min} = -3.0$, $\Delta\Psi = 0.2$
- (d) $\tau = 58.1$, $\Psi_{\max} = 2.3$, $\Psi_{\min} = -3.5$, $\Delta\Psi = 0.2$
- (e) $\tau = 59.0$, $\Psi_{\max} = 2.0$, $\Psi_{\min} = -3.6$, $\Delta\Psi = 0.2$

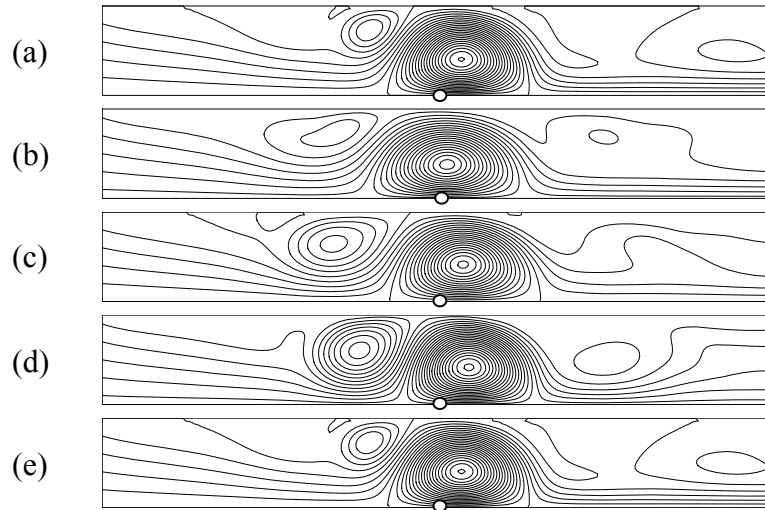


Figure A.14 Flow fields predicted by two-way coupling model for $V_0 = 17.5$ kV,
 $Re = 300$

- (a) $\tau = 58.0$, $\Psi_{\max} = 2.0$, $\Psi_{\min} = -3.6$, $\Delta\Psi = 0.2$
- (b) $\tau = 58.7$, $\Psi_{\max} = 1.5$, $\Psi_{\min} = -3.3$, $\Delta\Psi = 0.2$
- (c) $\tau = 59.4$, $\Psi_{\max} = 1.8$, $\Psi_{\min} = -3.0$, $\Delta\Psi = 0.2$
- (d) $\tau = 60.1$, $\Psi_{\max} = 2.3$, $\Psi_{\min} = -3.5$, $\Delta\Psi = 0.2$
- (e) $\tau = 60.9$, $\Psi_{\max} = 2.0$, $\Psi_{\min} = -3.6$, $\Delta\Psi = 0.2$

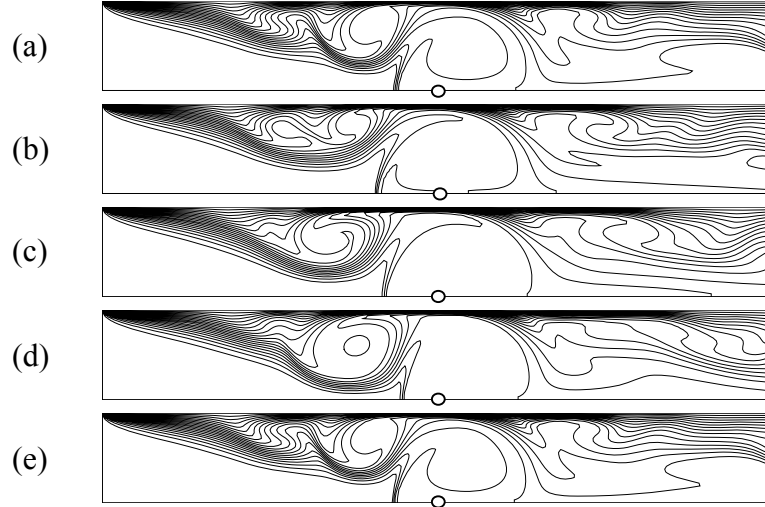


Figure A.15 Temperature fields predicted by one-way coupling model for $V_0 = 17.5$ kV,
 $Re = 300$

- (a) $\tau = 56.0, \theta_{\max} = 1.0, \theta_{\min} = 0.0, \Delta = 0.05$
- (b) $\tau = 56.7, \theta_{\max} = 1.0, \theta_{\min} = 0.0, \Delta = 0.05$
- (c) $\tau = 57.4, \theta_{\max} = 1.0, \theta_{\min} = 0.0, \Delta = 0.05$
- (d) $\tau = 58.1, \theta_{\max} = 1.0, \theta_{\min} = 0.0, \Delta = 0.05$
- (e) $\tau = 59.0, \theta_{\max} = 1.0, \theta_{\min} = 0.0, \Delta = 0.05$

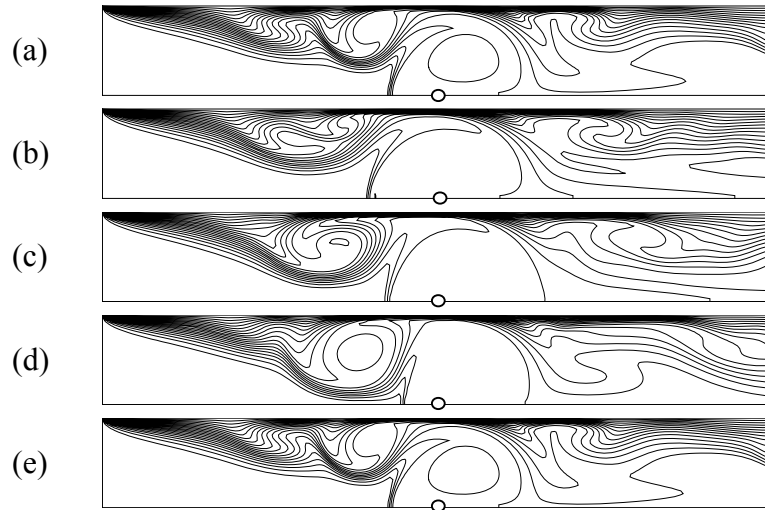


Figure A.16 Temperature fields predicted by two-way coupling model for $V_0 = 17.5$ kV,
 $Re = 300$

- (a) $\tau = 58.0, \theta_{\max} = 1.0, \theta_{\min} = 0.0, \Delta = 0.05$
- (b) $\tau = 58.7, \theta_{\max} = 1.0, \theta_{\min} = 0.0, \Delta = 0.05$
- (c) $\tau = 59.4, \theta_{\max} = 1.0, \theta_{\min} = 0.0, \Delta = 0.05$
- (d) $\tau = 60.1, \theta_{\max} = 1.0, \theta_{\min} = 0.0, \Delta = 0.05$
- (e) $\tau = 60.9, \theta_{\max} = 1.0, \theta_{\min} = 0.0, \Delta = 0.05$

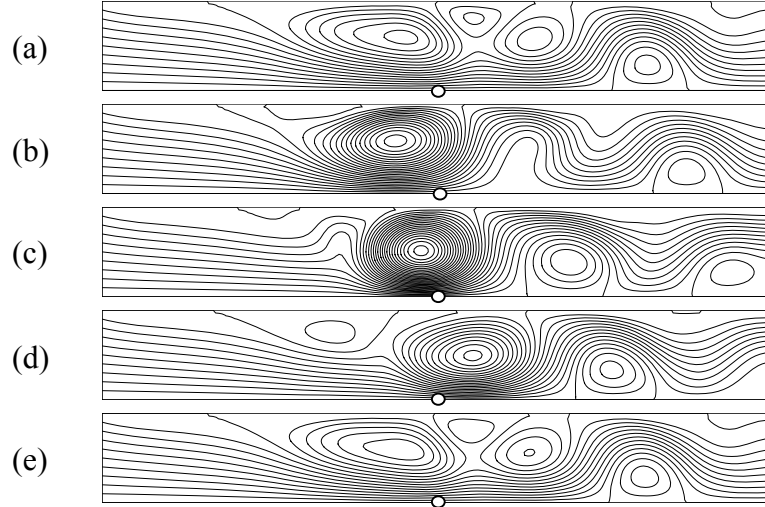


Figure A.17 Flow fields predicted by one-way coupling model for $V_0 = 17.5$ kV,
 $Re = 450$

- (a) $\tau = 58.6$, $\Psi_{\max} = 1.7$, $\Psi_{\min} = -0.3$, $\Delta\Psi = 0.1$
- (b) $\tau = 59.1$, $\Psi_{\max} = 2.6$, $\Psi_{\min} = -0.2$, $\Delta\Psi = 0.1$
- (c) $\tau = 59.6$, $\Psi_{\max} = 2.9$, $\Psi_{\min} = -0.4$, $\Delta\Psi = 0.1$
- (d) $\tau = 60.1$, $\Psi_{\max} = 2.0$, $\Psi_{\min} = -0.4$, $\Delta\Psi = 0.1$
- (e) $\tau = 60.6$, $\Psi_{\max} = 1.6$, $\Psi_{\min} = -0.3$, $\Delta\Psi = 0.1$

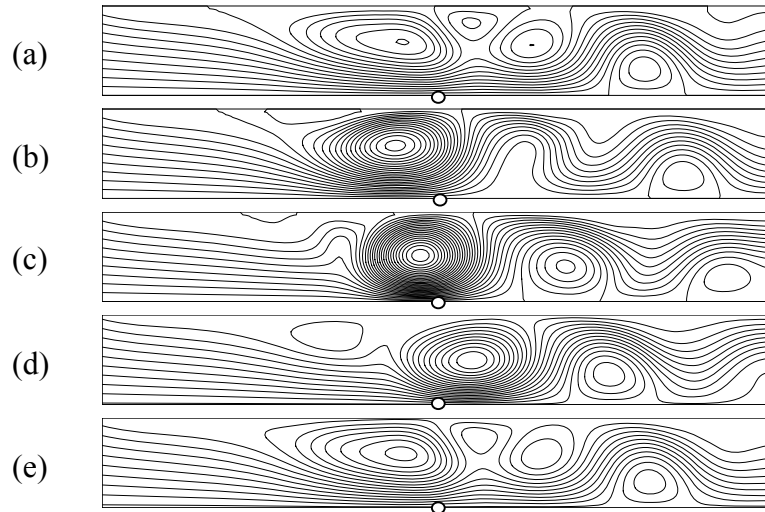


Figure A.18 Flow fields predicted by two-way coupling model for $V_0 = 17.5$ kV,
 $Re = 450$

- (a) $\tau = 56.7$, $\Psi_{\max} = 1.6$, $\Psi_{\min} = -0.3$, $\Delta\Psi = 0.1$
- (b) $\tau = 57.2$, $\Psi_{\max} = 2.5$, $\Psi_{\min} = -0.2$, $\Delta\Psi = 0.1$
- (c) $\tau = 57.7$, $\Psi_{\max} = 2.9$, $\Psi_{\min} = -0.5$, $\Delta\Psi = 0.1$
- (d) $\tau = 58.2$, $\Psi_{\max} = 2.1$, $\Psi_{\min} = -0.4$, $\Delta\Psi = 0.1$
- (e) $\tau = 58.6$, $\Psi_{\max} = 1.8$, $\Psi_{\min} = -0.3$, $\Delta\Psi = 0.1$

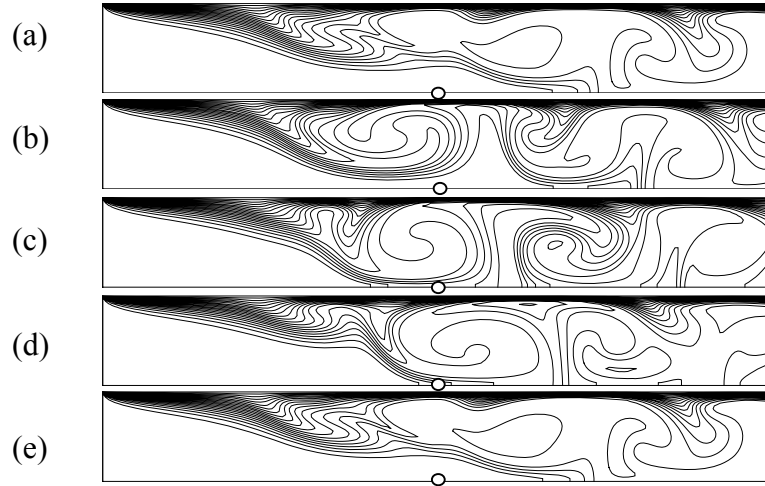


Figure A.19 Temperature fields predicted by one-way coupling model for $V_0 = 17.5$ kV,
 $Re = 450$

- (a) $\tau = 58.6, \theta_{\max} = 1.0, \theta_{\min} = 0.0, \Delta = 0.05$
- (b) $\tau = 59.1, \theta_{\max} = 1.0, \theta_{\min} = 0.0, \Delta = 0.05$
- (c) $\tau = 59.6, \theta_{\max} = 1.0, \theta_{\min} = 0.0, \Delta = 0.05$
- (d) $\tau = 60.1, \theta_{\max} = 1.0, \theta_{\min} = 0.0, \Delta = 0.05$
- (e) $\tau = 60.6, \theta_{\max} = 1.0, \theta_{\min} = 0.0, \Delta = 0.05$

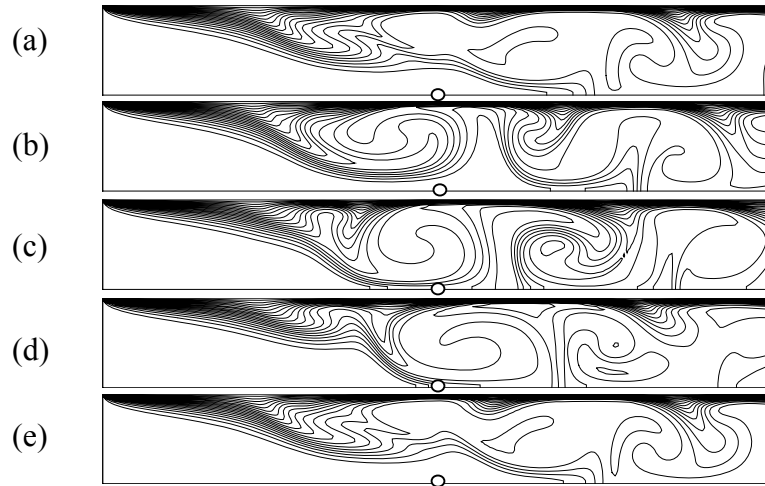


Figure A.20 Temperature fields predicted by two-way coupling model for $V_0 = 17.5$ kV,
 $Re = 450$

- (a) $\tau = 56.7, \theta_{\max} = 1.0, \theta_{\min} = 0.0, \Delta = 0.05$
- (b) $\tau = 57.2, \theta_{\max} = 1.0, \theta_{\min} = 0.0, \Delta = 0.05$
- (c) $\tau = 57.7, \theta_{\max} = 1.0, \theta_{\min} = 0.0, \Delta = 0.05$
- (d) $\tau = 58.2, \theta_{\max} = 1.0, \theta_{\min} = 0.0, \Delta = 0.05$
- (e) $\tau = 58.6, \theta_{\max} = 1.0, \theta_{\min} = 0.0, \Delta = 0.05$

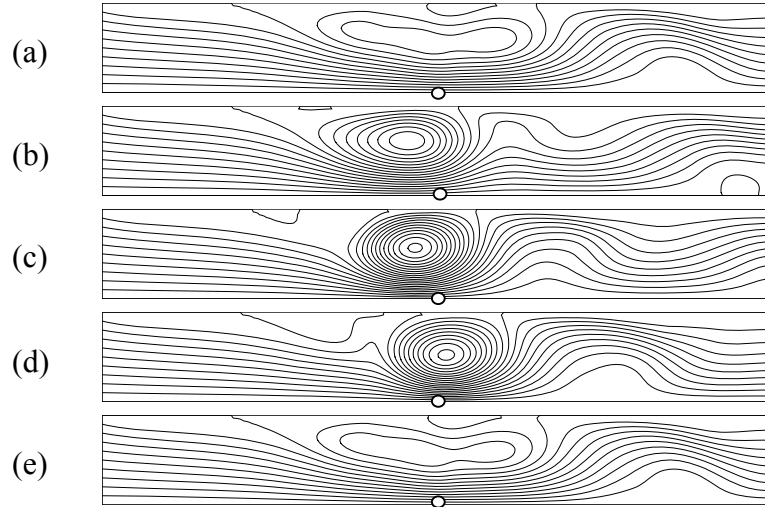


Figure A.21 Flow fields predicted by one-way coupling model for $V_0 = 17.5$ kV,
 $Re = 600$

(a) $\tau = 57.6$, $\Psi_{\max} = 1.3$, $\Psi_{\min} = 0.0$, $\Delta\Psi = 0.1$

(b) $\tau = 58.2$, $\Psi_{\max} = 1.8$, $\Psi_{\min} = 0.0$, $\Delta\Psi = 0.1$

(c) $\tau = 58.8$, $\Psi_{\max} = 2.2$, $\Psi_{\min} = 0.0$, $\Delta\Psi = 0.1$

(d) $\tau = 59.4$, $\Psi_{\max} = 2.0$, $\Psi_{\min} = 0.0$, $\Delta\Psi = 0.1$

(e) $\tau = 59.9$, $\Psi_{\max} = 1.3$, $\Psi_{\min} = 0.0$, $\Delta\Psi = 0.1$

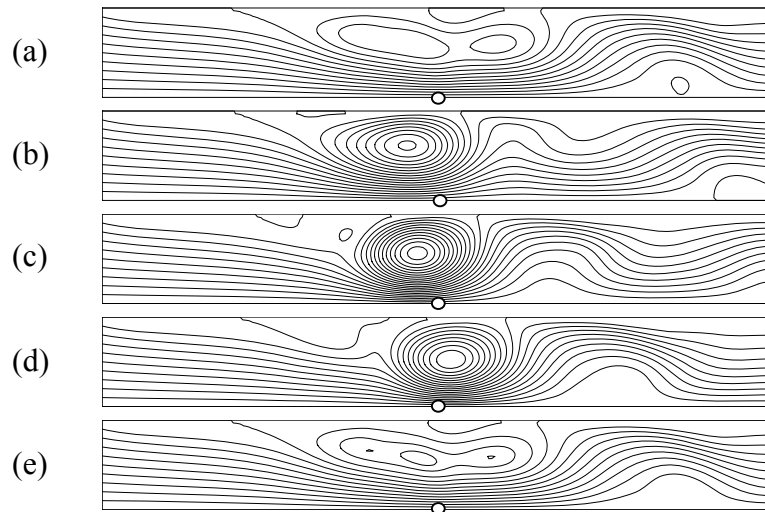


Figure A.22 Flow fields predicted by two-way coupling model for $V_0 = 17.5$ kV,
 $Re = 600$

(a) $\tau = 57.7$, $\Psi_{\max} = 1.3$, $\Psi_{\min} = 0.0$, $\Delta\Psi = 0.1$

(b) $\tau = 58.3$, $\Psi_{\max} = 1.9$, $\Psi_{\min} = 0.0$, $\Delta\Psi = 0.1$

(c) $\tau = 58.9$, $\Psi_{\max} = 2.2$, $\Psi_{\min} = 0.0$, $\Delta\Psi = 0.1$

(d) $\tau = 59.5$, $\Psi_{\max} = 1.9$, $\Psi_{\min} = 0.0$, $\Delta\Psi = 0.1$

(e) $\tau = 60.1$, $\Psi_{\max} = 1.3$, $\Psi_{\min} = 0.0$, $\Delta\Psi = 0.1$

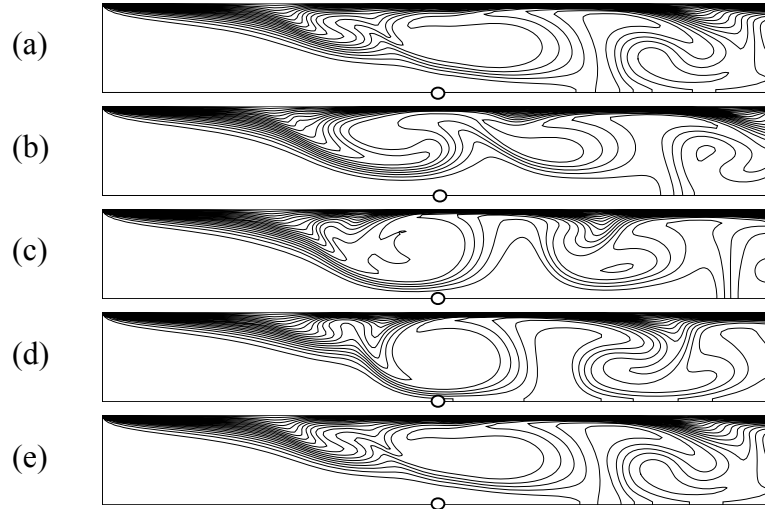


Figure A.23 Temperature fields predicted by one-way coupling model for $V_0 = 17.5$ kV,
 $Re = 600$

- (a) $\tau = 57.6, \theta_{\max} = 1.0, \theta_{\min} = 0.0, \Delta = 0.05$
- (b) $\tau = 58.2, \theta_{\max} = 1.0, \theta_{\min} = 0.0, \Delta = 0.05$
- (c) $\tau = 58.8, \theta_{\max} = 1.0, \theta_{\min} = 0.0, \Delta = 0.05$
- (d) $\tau = 59.4, \theta_{\max} = 1.0, \theta_{\min} = 0.0, \Delta = 0.05$
- (e) $\tau = 59.9, \theta_{\max} = 1.0, \theta_{\min} = 0.0, \Delta = 0.05$

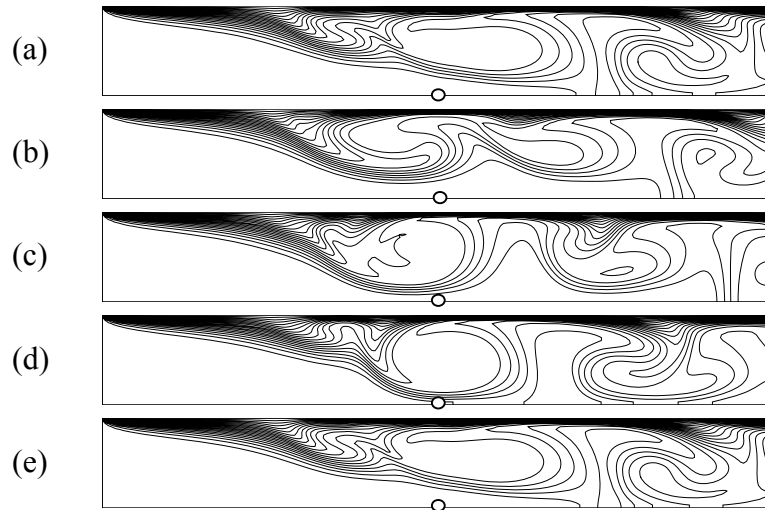


Figure A.24 Temperature fields predicted by two-way coupling model for $V_0 = 17.5$ kV,
 $Re = 600$

- (a) $\tau = 57.7, \theta_{\max} = 1.0, \theta_{\min} = 0.0, \Delta = 0.05$
- (b) $\tau = 58.3, \theta_{\max} = 1.0, \theta_{\min} = 0.0, \Delta = 0.05$
- (c) $\tau = 58.9, \theta_{\max} = 1.0, \theta_{\min} = 0.0, \Delta = 0.05$
- (d) $\tau = 59.5, \theta_{\max} = 1.0, \theta_{\min} = 0.0, \Delta = 0.05$
- (e) $\tau = 60.1, \theta_{\max} = 1.0, \theta_{\min} = 0.0, \Delta = 0.05$

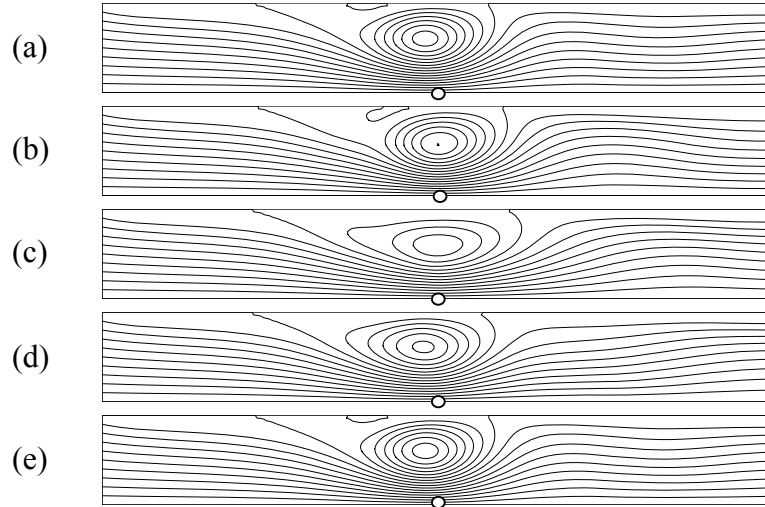


Figure A.25 Flow fields predicted by one-way coupling model for $V_0 = 17.5$ kV,
 $Re = 750$

- (a) $\tau = 58.4$, $\Psi_{\max} = 1.7$, $\Psi_{\min} = 0.0$, $\Delta\Psi = 0.1$
- (b) $\tau = 59.2$, $\Psi_{\max} = 1.6$, $\Psi_{\min} = 0.0$, $\Delta\Psi = 0.1$
- (c) $\tau = 60.0$, $\Psi_{\max} = 1.4$, $\Psi_{\min} = 0.0$, $\Delta\Psi = 0.1$
- (d) $\tau = 60.8$, $\Psi_{\max} = 1.6$, $\Psi_{\min} = 0.0$, $\Delta\Psi = 0.1$
- (e) $\tau = 61.4$, $\Psi_{\max} = 1.7$, $\Psi_{\min} = 0.0$, $\Delta\Psi = 0.1$

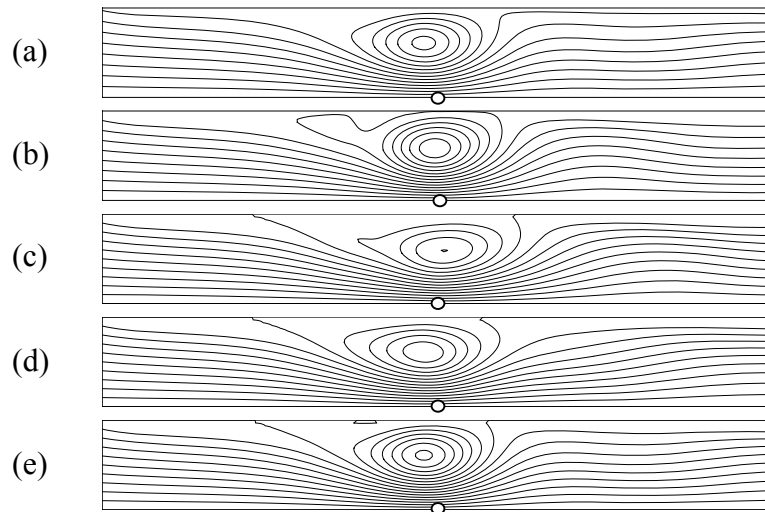


Figure A.26 Flow fields predicted by two-way coupling model for $V_0 = 17.5$ kV,
 $Re = 750$

- (a) $\tau = 58.2$, $\Psi_{\max} = 1.7$, $\Psi_{\min} = 0.0$, $\Delta\Psi = 0.1$
- (b) $\tau = 59.0$, $\Psi_{\max} = 1.9$, $\Psi_{\min} = 0.0$, $\Delta\Psi = 0.1$
- (c) $\tau = 59.8$, $\Psi_{\max} = 2.3$, $\Psi_{\min} = 0.0$, $\Delta\Psi = 0.1$
- (d) $\tau = 60.6$, $\Psi_{\max} = 2.0$, $\Psi_{\min} = 0.0$, $\Delta\Psi = 0.1$
- (e) $\tau = 61.2$, $\Psi_{\max} = 1.7$, $\Psi_{\min} = 0.0$, $\Delta\Psi = 0.1$

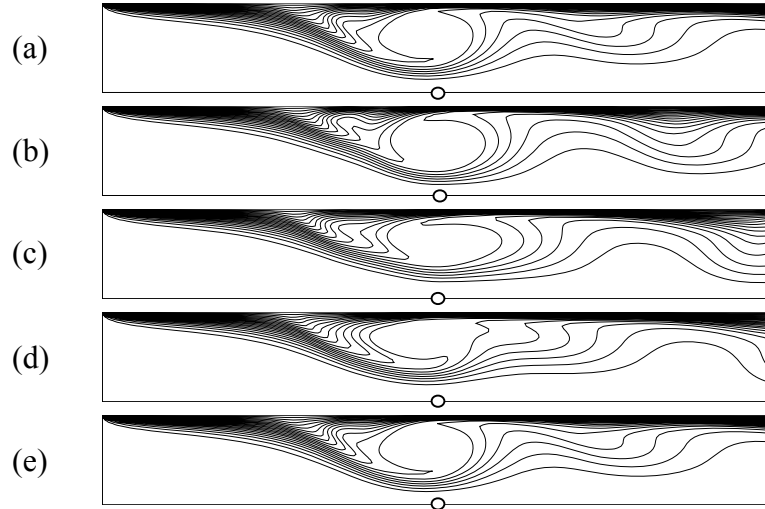


Figure A.27 Temperature fields predicted by one-way coupling model for $V_0 = 17.5$ kV,
 $Re = 750$

- (a) $\tau = 58.4$, $\theta_{\max} = 1.0$, $\theta_{\min} = 0.0$, $\Delta = 0.05$
- (b) $\tau = 59.2$, $\theta_{\max} = 1.0$, $\theta_{\min} = 0.0$, $\Delta = 0.05$
- (c) $\tau = 60.0$, $\theta_{\max} = 1.0$, $\theta_{\min} = 0.0$, $\Delta = 0.05$
- (d) $\tau = 60.8$, $\theta_{\max} = 1.0$, $\theta_{\min} = 0.0$, $\Delta = 0.05$
- (e) $\tau = 61.4$, $\theta_{\max} = 1.0$, $\theta_{\min} = 0.0$, $\Delta = 0.05$

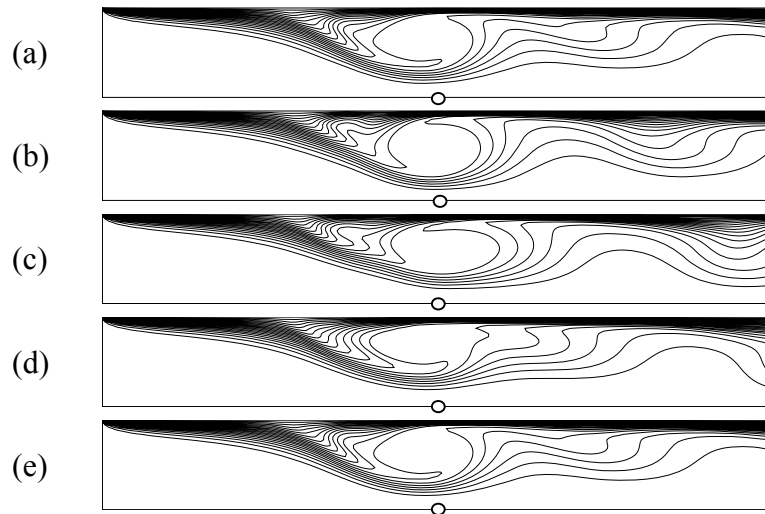


Figure A.28 Temperature fields predicted by two-way coupling model for $V_0 = 17.5$ kV,
 $Re = 750$

- (a) $\tau = 58.2$, $\theta_{\max} = 1.0$, $\theta_{\min} = 0.0$, $\Delta = 0.05$
- (b) $\tau = 59.0$, $\theta_{\max} = 1.0$, $\theta_{\min} = 0.0$, $\Delta = 0.05$
- (c) $\tau = 59.8$, $\theta_{\max} = 1.0$, $\theta_{\min} = 0.0$, $\Delta = 0.05$
- (d) $\tau = 60.6$, $\theta_{\max} = 1.0$, $\theta_{\min} = 0.0$, $\Delta = 0.05$
- (e) $\tau = 61.2$, $\theta_{\max} = 1.0$, $\theta_{\min} = 0.0$, $\Delta = 0.05$

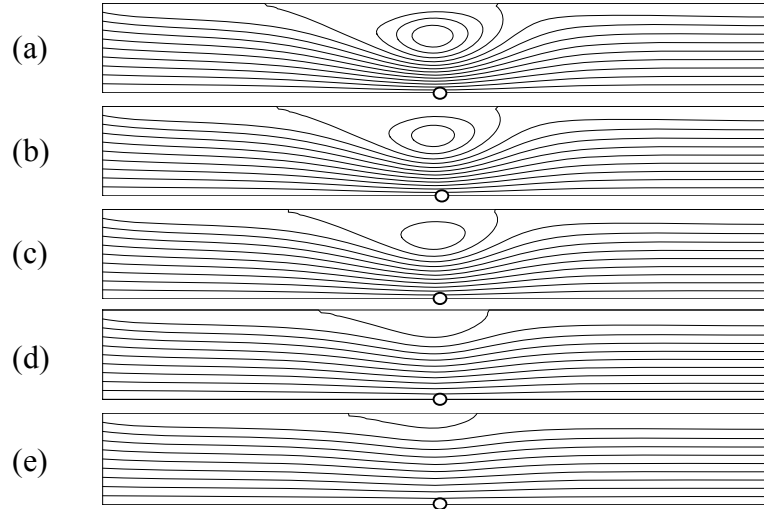


Figure A.29 Flow fields predicted by one-way coupling model for $V_0 = 17.5$ kV

- (a) $Re = 900$, $\Psi_{\max} = 1.2$, $\Psi_{\min} = 0.5$, $\Delta\Psi = 0.05$
- (b) $Re = 1050$, $\Psi_{\max} = 1.2$, $\Psi_{\min} = 0.5$, $\Delta\Psi = 0.05$
- (c) $Re = 1200$, $\Psi_{\max} = 1.1$, $\Psi_{\min} = 0.5$, $\Delta\Psi = 0.05$
- (d) $Re = 1800$, $\Psi_{\max} = 1.0$, $\Psi_{\min} = 0.5$, $\Delta\Psi = 0.05$
- (e) $Re = 2400$, $\Psi_{\max} = 1.0$, $\Psi_{\min} = 0.5$, $\Delta\Psi = 0.05$

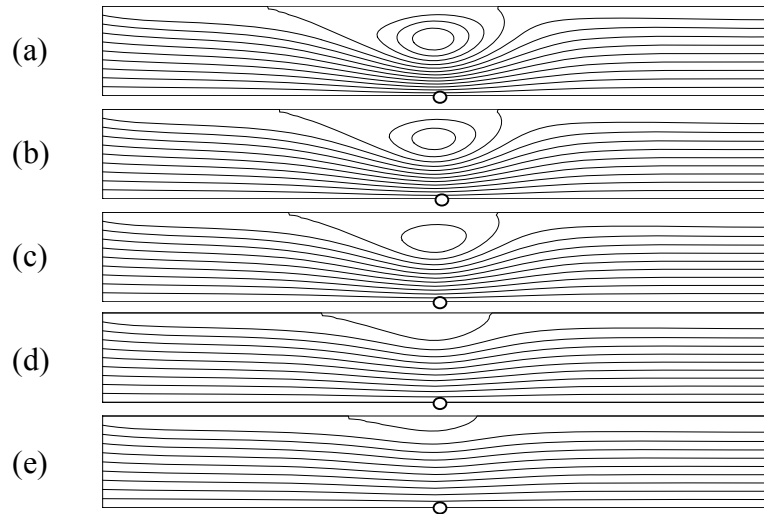


Figure A.30 Flow fields predicted by two-way coupling model for $V_0 = 17.5$ kV

- (a) $Re = 900$, $\Psi_{\max} = 1.2$, $\Psi_{\min} = 0.5$, $\Delta\Psi = 0.05$
- (b) $Re = 1050$, $\Psi_{\max} = 1.2$, $\Psi_{\min} = 0.5$, $\Delta\Psi = 0.05$
- (c) $Re = 1200$, $\Psi_{\max} = 1.1$, $\Psi_{\min} = 0.5$, $\Delta\Psi = 0.05$
- (d) $Re = 1800$, $\Psi_{\max} = 1.0$, $\Psi_{\min} = 0.5$, $\Delta\Psi = 0.05$
- (e) $Re = 2400$, $\Psi_{\max} = 1.0$, $\Psi_{\min} = 0.5$, $\Delta\Psi = 0.05$

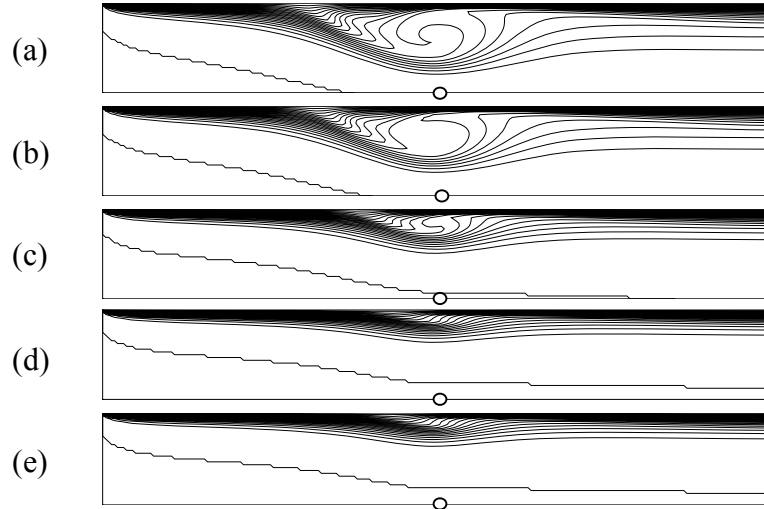


Figure A.31 Temperature fields predicted by one-way coupling model for $V_0 = 17.5$ kV

- (a) $Re = 900$, $\theta_{\max} = 1.0$, $\theta_{\min} = 0.0$, $\Delta = 0.05$
- (b) $Re = 1050$, $\theta_{\max} = 1.0$, $\theta_{\min} = 0.0$, $\Delta = 0.05$
- (c) $Re = 1200$, $\theta_{\max} = 1.0$, $\theta_{\min} = 0.0$, $\Delta = 0.05$
- (d) $Re = 1800$, $\theta_{\max} = 1.0$, $\theta_{\min} = 0.0$, $\Delta = 0.05$
- (e) $Re = 2400$, $\theta_{\max} = 1.0$, $\theta_{\min} = 0.0$, $\Delta = 0.05$

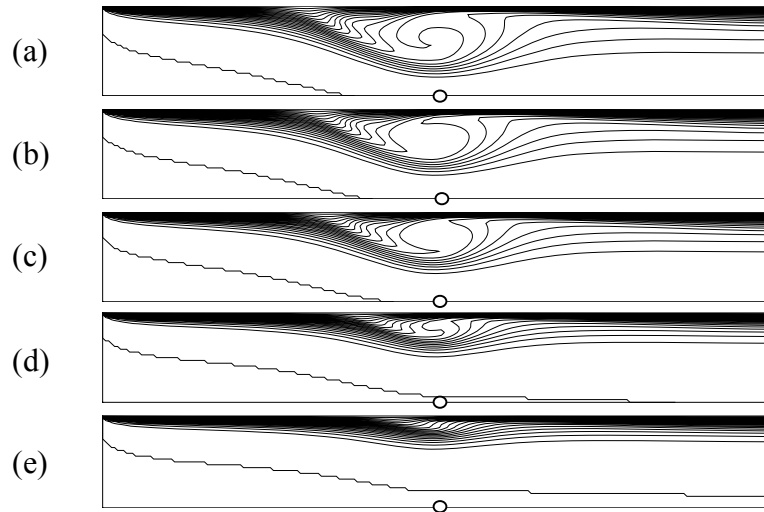


Figure A.32 Temperature fields predicted by two-way coupling model for $V_0 = 17.5$ kV

- (a) $Re = 900$, $\theta_{\max} = 1.0$, $\theta_{\min} = 0.0$, $\Delta = 0.05$
- (b) $Re = 1050$, $\theta_{\max} = 1.0$, $\theta_{\min} = 0.0$, $\Delta = 0.05$
- (c) $Re = 1200$, $\theta_{\max} = 1.0$, $\theta_{\min} = 0.0$, $\Delta = 0.05$
- (d) $Re = 1800$, $\theta_{\max} = 1.0$, $\theta_{\min} = 0.0$, $\Delta = 0.05$
- (e) $Re = 2400$, $\theta_{\max} = 1.0$, $\theta_{\min} = 0.0$, $\Delta = 0.05$

APPENDIX B

FLOW AND TEMPERATURE FIELDS OF JOULE

HEATING

Figure B.1	Flow fields at the wire position 3 ($V_0 = 12.0$ kV, $Ra = 10^4$, with Joule heating)	133
Figure B.2	Flow fields at the wire position 3 ($V_0 = 12.0$ kV, $Ra = 10^4$, without Joule heating)	133
Figure B.3	Temperature fields at the wire position 3 ($V_0 = 12.0$ kV, $Ra = 10^4$, with Joule heating)	134
Figure B.4	Temperature fields at the wire position 3 ($V_0 = 12.0$ kV, $Ra = 10^4$, without Joule heating)	134
Figure B.5	Flow fields at the wire position 3 ($V_0 = 12.0$ kV, $\Delta\Psi = 0.005$).....	135
Figure B.6	Temperature fields at the wire position 3 ($V_0 = 12.0$ kV, $\theta_{\max} = 1.0$, $\theta_{\min} = 0.0$, $\Delta\theta=0.1$)	135
Figure B.7	Flow fields at the wire position 2 ($V_0 = 12.0$ kV, $Ra = 10^4$, with Joule heating)	136
Figure B.8	Flow fields at the wire position 2 ($V_0 = 12.0$ kV, $Ra = 10^4$, without Joule heating)	136
Figure B.9	Flow fields at the wire position 2 ($V_0 = 15.0$ kV, $Ra = 10^6$, with Joule heating)	137
Figure B.10	Flow fields at the wire position 2 ($V_0 = 15.0$ kV, $Ra = 10^6$, without Joule heating)	137
Figure B.11	Temperature fields at the wire position 2 ($V_0 = 15.0$ kV, $Ra = 10^6$, with Joule heating)	138
Figure B.12	Temperature fields at the wire position 2 ($V_0 = 15.0$ kV, $Ra = 10^6$, without Joule heating)	138
Figure B.13	Flow fields at the wire position 1 ($V_0 = 12.0$ kV, $Ra = 10^4$, with Joule heating)	139

Figure B.14	Flow fields at the wire position 1 ($V_0 = 12.0$ kV, $Ra = 10^4$, without Joule heating)	139
Figure B.15	Temperature fields at the wire position 1 ($V_0 = 12.0$ kV, $Ra = 10^4$, with Joule heating)	140
Figure B.16	Temperature fields at the wire position 1 ($V_0 = 12.0$ kV, $Ra = 10^4$, without Joule heating)	140
Figure B.17	Flow fields at the wire position 1 ($V_0 = 12.0$ kV)	141
Figure B.18	Temperature at the wire position 1 ($V_0 = 12.0$ kV, $\theta_{\max} = 1.0$, $\theta_{\min} = 0.0$, $\Delta\theta = 0.1$)	141
Figure B.19	Flow fields at the wire position 1 ($V_0 = 15.0$ kV, $Ra = 10^6$, with Joule heating)	142
Figure B.20	Flow fields at the wire position 1 ($V_0 = 15.0$ kV, $Ra = 10^6$, without Joule heating)	142
Figure B.21	Temperature fields at wire the position 1 ($V_0 = 15.0$ kV, $Ra = 10^6$, with Joule heating)	143
Figure B.22	Temperature fields at the wire position 1 ($V_0 = 15.0$ kV, $Ra = 10^6$, without Joule heating)	143
Figure B.23	Variation of Nusselt number with time for $V_0 = 12.0$ kV	144
Figure B.24	Variation of Nusselt number with time for $V_0 = 12.0$ kV	145
Figure B.25	Variation of Nusselt number with time for $V_0 = 15.0$ kV	146
Figure B.26	Variation of Nusselt number with time for $V_0 = 15.0$ kV	147
Figure B.27	Variation of Nusselt number with time for $V_0 = 18.0$ kV	148
Figure B.28	Variation of Nusselt number with time for $V_0 = 18.0$ kV	149

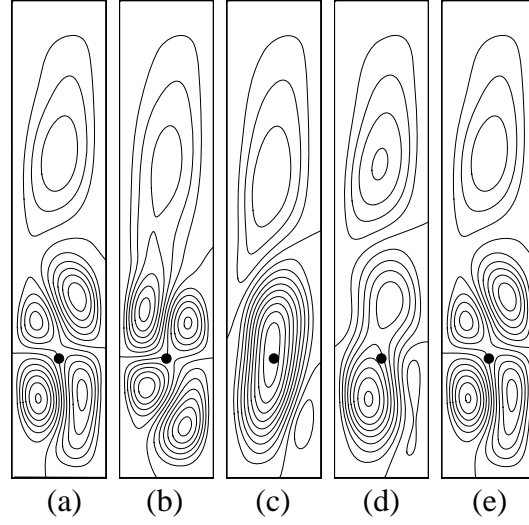


Figure B.1 Flow fields at the wire position 3 ($V_0 = 12.0$ kV, $Ra = 10^4$, with Joule heating)

- (a) $\tau = 614.7, \Psi_{\max} = 0.030, \Psi_{\min} = -0.030, \Delta\Psi = 0.005$
- (b) $\tau = 630.2, \Psi_{\max} = 0.030, \Psi_{\min} = -0.035, \Delta\Psi = 0.005$
- (c) $\tau = 645.7, \Psi_{\max} = 0.050, \Psi_{\min} = -0.020, \Delta\Psi = 0.005$
- (d) $\tau = 661.2, \Psi_{\max} = 0.040, \Psi_{\min} = -0.020, \Delta\Psi = 0.005$
- (e) $\tau = 676.7, \Psi_{\max} = 0.030, \Psi_{\min} = -0.030, \Delta\Psi = 0.005$

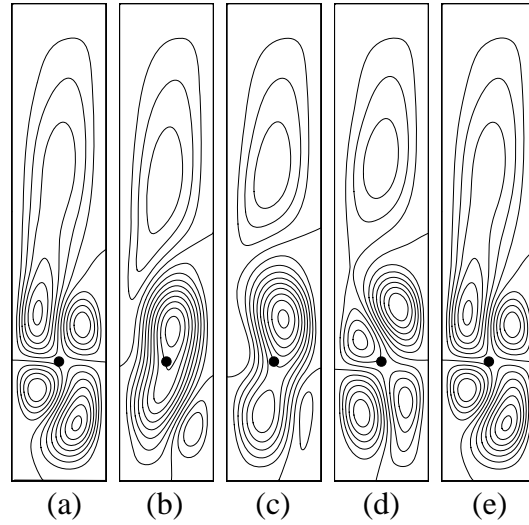


Figure B.2 Flow fields at the wire position 3 ($V_0 = 12.0$ kV, $Ra = 10^4$, without Joule heating)

- (a) $\tau = 615.8, \Psi_{\max} = 0.025, \Psi_{\min} = -0.040, \Delta\Psi = 0.005$
- (b) $\tau = 629.3, \Psi_{\max} = 0.050, \Psi_{\min} = -0.020, \Delta\Psi = 0.005$
- (c) $\tau = 642.8, \Psi_{\max} = 0.050, \Psi_{\min} = -0.020, \Delta\Psi = 0.005$
- (d) $\tau = 656.3, \Psi_{\max} = 0.035, \Psi_{\min} = -0.025, \Delta\Psi = 0.005$
- (e) $\tau = 670.8, \Psi_{\max} = 0.025, \Psi_{\min} = -0.040, \Delta\Psi = 0.005$

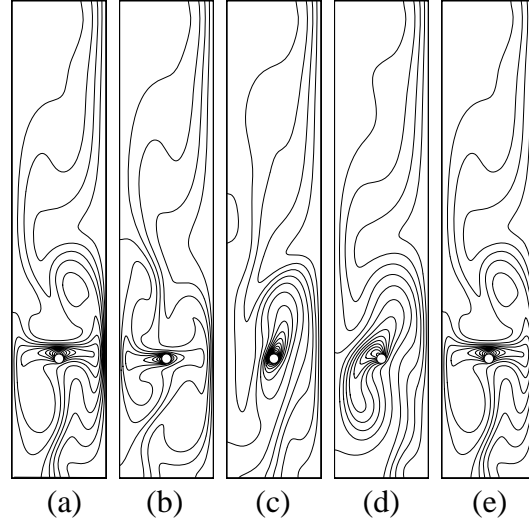


Figure B.3 Temperature fields at the wire position 3 ($V_0 = 12.0$ kV, $Ra = 10^4$, with Joule heating)

- (a) $\tau = 614.7$, $\theta_{\max} = 3.4$, $\theta_{\min} = 0.0$, $\Delta\theta = 0.2$
- (b) $\tau = 630.2$, $\theta_{\max} = 3.6$, $\theta_{\min} = 0.0$, $\Delta\theta = 0.2$
- (c) $\tau = 645.7$, $\theta_{\max} = 4.4$, $\theta_{\min} = 0.0$, $\Delta\theta = 0.2$
- (d) $\tau = 661.2$, $\theta_{\max} = 3.2$, $\theta_{\min} = 0.0$, $\Delta\theta = 0.2$
- (e) $\tau = 676.7$, $\theta_{\max} = 3.4$, $\theta_{\min} = 0.0$, $\Delta\theta = 0.2$

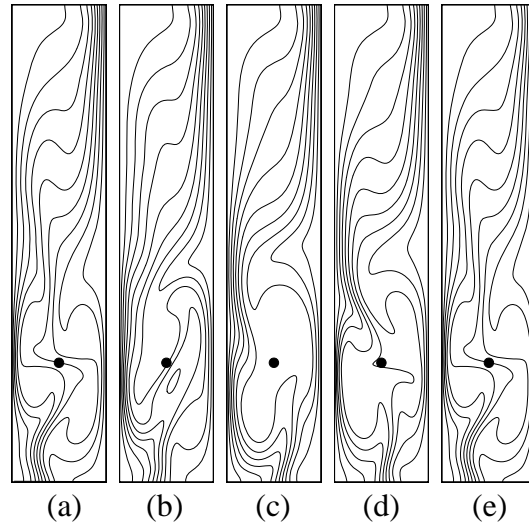


Figure B.4 Temperature fields at the wire position 3 ($V_0 = 12.0$ kV, $Ra = 10^4$, without Joule heating)

- (a) $\tau = 615.8$, $\theta_{\max} = 1.0$, $\theta_{\min} = 0.0$, $\Delta\theta = 0.1$
- (b) $\tau = 629.3$, $\theta_{\max} = 1.0$, $\theta_{\min} = 0.0$, $\Delta\theta = 0.1$
- (c) $\tau = 642.8$, $\theta_{\max} = 1.0$, $\theta_{\min} = 0.0$, $\Delta\theta = 0.1$
- (d) $\tau = 656.3$, $\theta_{\max} = 1.0$, $\theta_{\min} = 0.0$, $\Delta\theta = 0.1$
- (e) $\tau = 670.8$, $\theta_{\max} = 1.0$, $\theta_{\min} = 0.0$, $\Delta\theta = 0.1$

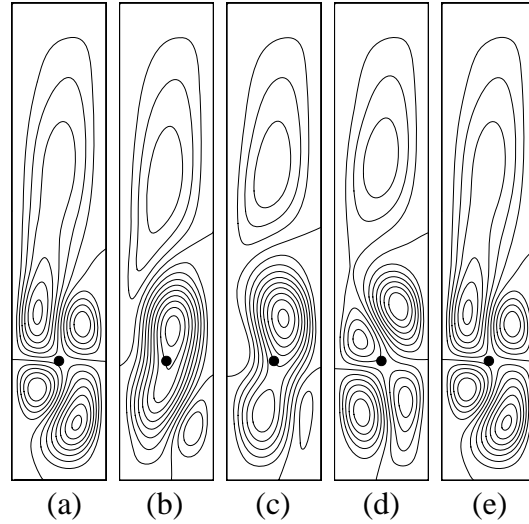


Figure B.5 Flow fields at the wire position 3 ($V_0 = 12.0$ kV, $\Delta\Psi = 0.005$)

- (a) $Ra = 10^5$, with joule heating, $\Psi_{\max} = 0.02$, $\Psi_{\min} = -0.045$
- (b) $Ra = 10^5$, without joule heating, $\Psi_{\max} = 0.00$, $\Psi_{\min} = -0.050$
- (c) $Ra = 10^6$, with joule heating, $\Psi_{\max} = 0.0$, $\Psi_{\min} = -0.070$
- (d) $Ra = 10^6$, without joule heating, $\Psi_{\max} = 0.0$, $\Psi_{\min} = -0.070$

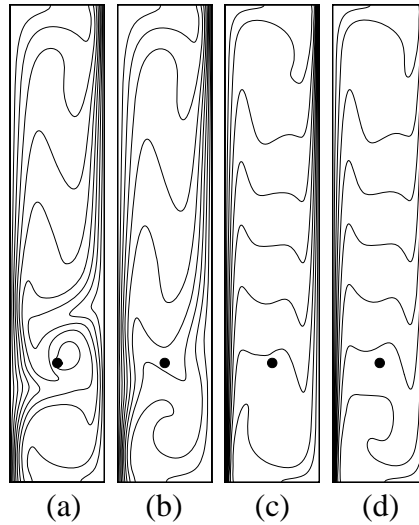


Figure B.6 Temperature fields at the wire position 3
($V_0 = 12.0$ kV, $\theta_{\max} = 1.0$, $\theta_{\min} = 0.0$, $\Delta\theta=0.1$)

- (a) $Ra = 10^5$, with Joule heating
- (b) $Ra = 10^5$, without Joule heating
- (c) $Ra = 10^6$, with Joule heating
- (d) $Ra = 10^6$, without Joule heating

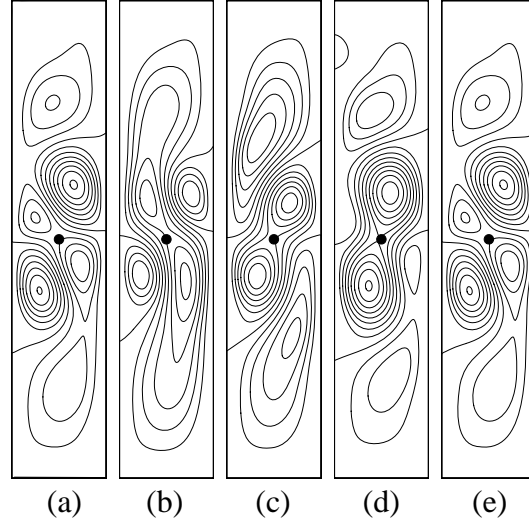


Figure B.7 Flow fields at the wire position 2 ($V_0 = 12.0\text{kV}$, $Ra = 10^4$, with Joule heating)

- (a) $\tau = 656.1$, $\Psi_{\max} = 0.040$, $\Psi_{\min} = -0.030$, $\Delta\Psi = 0.005$
- (b) $\tau = 668.6$, $\Psi_{\max} = 0.020$, $\Psi_{\min} = -0.035$, $\Delta\Psi = 0.005$
- (c) $\tau = 681.1$, $\Psi_{\max} = 0.035$, $\Psi_{\min} = -0.030$, $\Delta\Psi = 0.005$
- (d) $\tau = 693.6$, $\Psi_{\max} = 0.045$, $\Psi_{\min} = -0.020$, $\Delta\Psi = 0.005$
- (e) $\tau = 705.8$, $\Psi_{\max} = 0.040$, $\Psi_{\min} = -0.025$, $\Delta\Psi = 0.005$

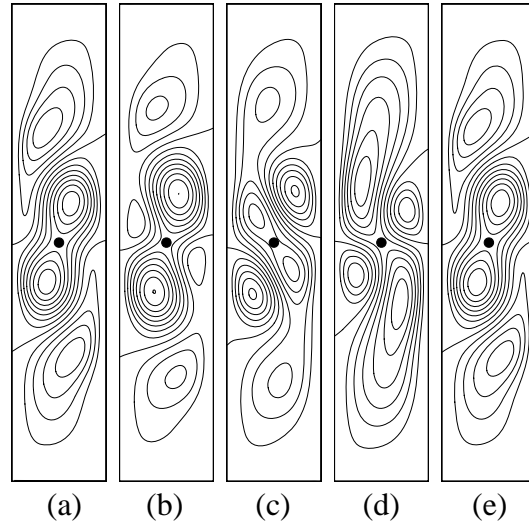


Figure B.8 Flow fields at the wire position 2 ($V_0 = 12.0\text{ kV}$, $Ra = 10^4$, without Joule heating)

- (a) $\tau = 611.9$, $\Psi_{\max} = 0.040$, $\Psi_{\min} = -0.025$, $\Delta\Psi = 0.005$
- (b) $\tau = 623.9$, $\Psi_{\max} = 0.040$, $\Psi_{\min} = -0.020$, $\Delta\Psi = 0.005$
- (c) $\tau = 635.9$, $\Psi_{\max} = 0.030$, $\Psi_{\min} = -0.030$, $\Delta\Psi = 0.005$
- (d) $\tau = 647.9$, $\Psi_{\max} = 0.020$, $\Psi_{\min} = -0.035$, $\Delta\Psi = 0.005$
- (e) $\tau = 660.9$, $\Psi_{\max} = 0.040$, $\Psi_{\min} = -0.025$, $\Delta\Psi = 0.005$

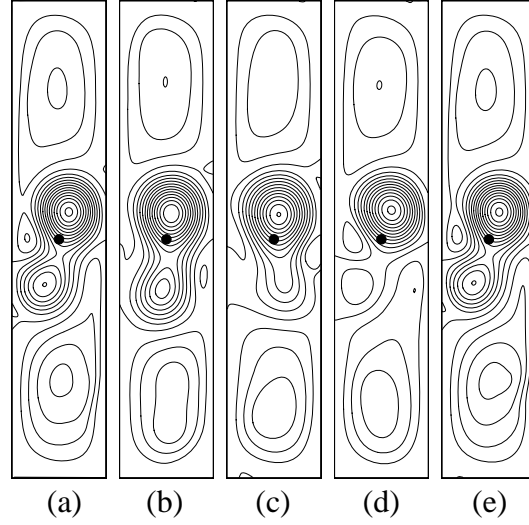


Figure B.9 Flow fields at the wire position 2 ($V_0 = 15.0$ kV, $Ra = 10^6$, with Joule heating)

- (a) $\tau = 629.0$, $\Psi_{\max} = 0.13$, $\Psi_{\min} = -0.05$, $\Delta\Psi = 0.005$
- (b) $\tau = 636.0$, $\Psi_{\max} = 0.13$, $\Psi_{\min} = -0.05$, $\Delta\Psi = 0.005$
- (c) $\tau = 643.0$, $\Psi_{\max} = 0.13$, $\Psi_{\min} = -0.05$, $\Delta\Psi = 0.005$
- (d) $\tau = 650.0$, $\Psi_{\max} = 0.13$, $\Psi_{\min} = -0.05$, $\Delta\Psi = 0.005$
- (e) $\tau = 659.0$, $\Psi_{\max} = 0.13$, $\Psi_{\min} = -0.05$, $\Delta\Psi = 0.005$

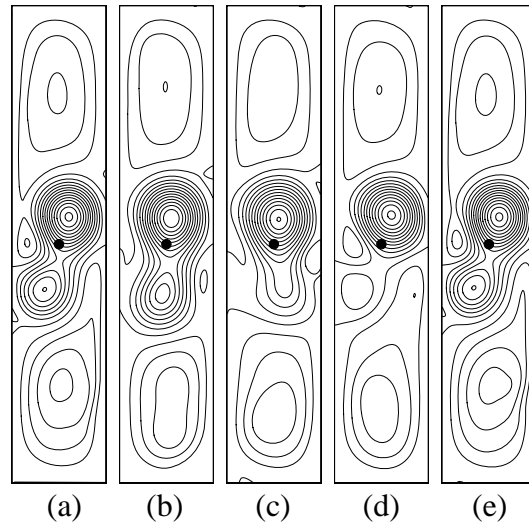


Figure B.10 Flow fields at the wire position 2 ($V_0 = 15.0$ kV, $Ra = 10^6$, without Joule heating)

- (a) $\tau = 618.0$, $\Psi_{\max} = 0.13$, $\Psi_{\min} = -0.05$, $\Delta\Psi = 0.005$
- (b) $\tau = 625.0$, $\Psi_{\max} = 0.13$, $\Psi_{\min} = -0.05$, $\Delta\Psi = 0.005$
- (c) $\tau = 632.0$, $\Psi_{\max} = 0.13$, $\Psi_{\min} = -0.05$, $\Delta\Psi = 0.005$
- (d) $\tau = 639.0$, $\Psi_{\max} = 0.13$, $\Psi_{\min} = -0.05$, $\Delta\Psi = 0.005$
- (e) $\tau = 646.3$, $\Psi_{\max} = 0.13$, $\Psi_{\min} = -0.05$, $\Delta\Psi = 0.005$

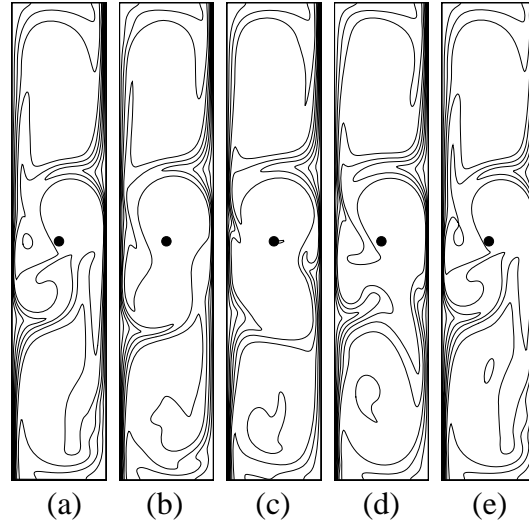


Figure B.11 Temperature fields at the wire position 2 ($V_0 = 15.0$ kV, $Ra = 10^6$, with Joule heating)

- (a) $\tau = 629.0$, $\theta_{\max} = 1.0$, $\theta_{\min} = 0.0$, $\Delta\theta = 0.05$
- (b) $\tau = 636.0$, $\theta_{\max} = 1.0$, $\theta_{\min} = 0.0$, $\Delta\theta = 0.05$
- (c) $\tau = 643.0$, $\theta_{\max} = 1.0$, $\theta_{\min} = 0.0$, $\Delta\theta = 0.05$
- (d) $\tau = 650.0$, $\theta_{\max} = 1.0$, $\theta_{\min} = 0.0$, $\Delta\theta = 0.05$
- (e) $\tau = 659.0$, $\theta_{\max} = 1.0$, $\theta_{\min} = 0.0$, $\Delta\theta = 0.05$

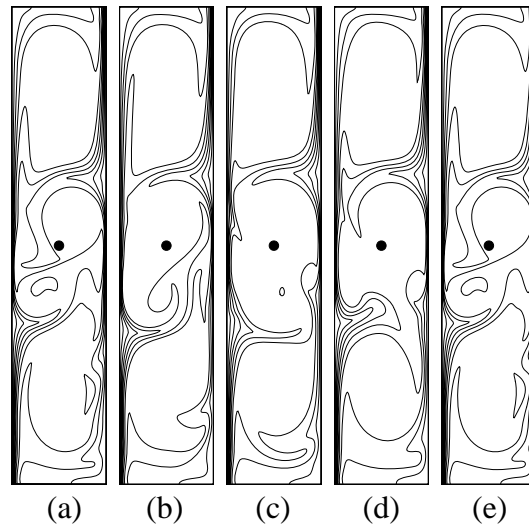


Figure B.12 Temperature fields at the wire position 2 ($V_0 = 15.0$ kV, $Ra = 10^6$, without Joule heating)

- (a) $\tau = 618.0$, $\theta_{\max} = 1.0$, $\theta_{\min} = 0.0$, $\Delta\theta = 0.05$
- (b) $\tau = 625.0$, $\theta_{\max} = 1.0$, $\theta_{\min} = 0.0$, $\Delta\theta = 0.05$
- (c) $\tau = 632.0$, $\theta_{\max} = 1.0$, $\theta_{\min} = 0.0$, $\Delta\theta = 0.05$
- (d) $\tau = 639.0$, $\theta_{\max} = 1.0$, $\theta_{\min} = 0.0$, $\Delta\theta = 0.05$
- (e) $\tau = 646.3$, $\theta_{\max} = 1.0$, $\theta_{\min} = 0.0$, $\Delta\theta = 0.05$

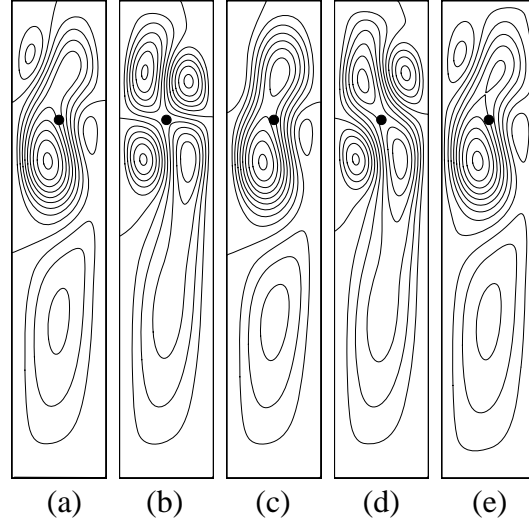


Figure B.13 Flow fields at the wire position 1 ($V_0 = 12.0$ kV, $Ra = 10^4$, with Joule heating)

- (a) $\tau = 697.5$, $\Psi_{\max} = 0.050$, $\Psi_{\min} = -0.020$, $\Delta\Psi = 0.005$
- (b) $\tau = 722.5$, $\Psi_{\max} = 0.025$, $\Psi_{\min} = -0.035$, $\Delta\Psi = 0.005$
- (c) $\tau = 747.5$, $\Psi_{\max} = 0.050$, $\Psi_{\min} = -0.020$, $\Delta\Psi = 0.005$
- (d) $\tau = 772.5$, $\Psi_{\max} = 0.030$, $\Psi_{\min} = -0.030$, $\Delta\Psi = 0.005$
- (e) $\tau = 798.9$, $\Psi_{\max} = 0.050$, $\Psi_{\min} = -0.020$, $\Delta\Psi = 0.005$

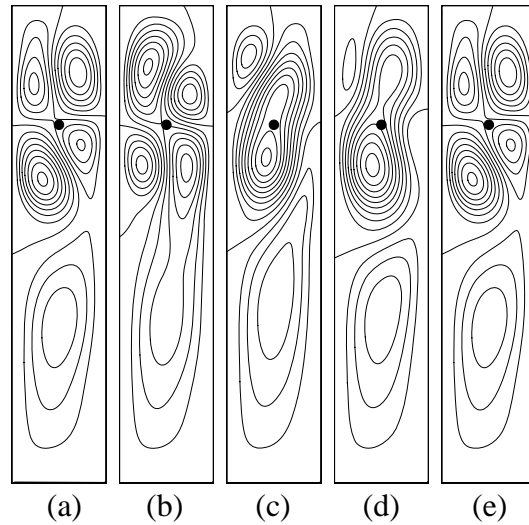


Figure B.14 Flow fields at the wire position 1 ($V_0 = 12.0$ kV, $Ra = 10^4$, without Joule heating)

- (a) $\tau = 768.3$, $\Psi_{\max} = 0.040$, $\Psi_{\min} = -0.025$, $\Delta\Psi = 0.005$
- (b) $\tau = 781.9$, $\Psi_{\max} = 0.025$, $\Psi_{\min} = -0.040$, $\Delta\Psi = 0.005$
- (c) $\tau = 795.5$, $\Psi_{\max} = 0.050$, $\Psi_{\min} = -0.020$, $\Delta\Psi = 0.005$
- (d) $\tau = 809.1$, $\Psi_{\max} = 0.050$, $\Psi_{\min} = -0.020$, $\Delta\Psi = 0.005$
- (e) $\tau = 822.9$, $\Psi_{\max} = 0.040$, $\Psi_{\min} = -0.025$, $\Delta\Psi = 0.005$

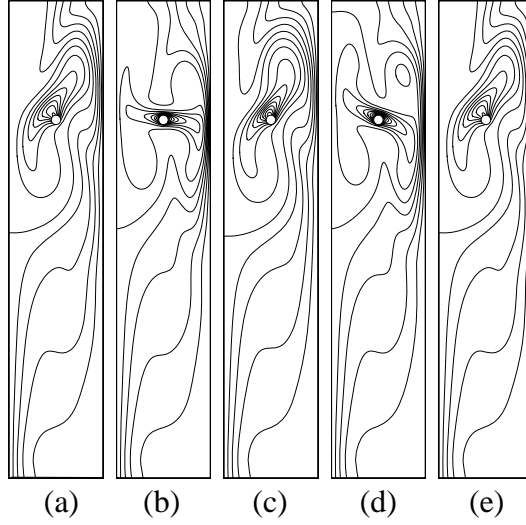


Figure B.15 Temperature fields at the wire position 1 ($V_0 = 12.0$ kV, $Ra = 10^4$, with Joule heating)

- (a) $\tau = 697.5$, $\theta_{\max} = 3.0$, $\theta_{\min} = 0.0$, $\Delta\theta = 0.2$
- (b) $\tau = 722.5$, $\theta_{\max} = 4.0$, $\theta_{\min} = 0.0$, $\Delta\theta = 0.2$
- (c) $\tau = 747.5$, $\theta_{\max} = 3.2$, $\theta_{\min} = 0.0$, $\Delta\theta = 0.2$
- (d) $\tau = 772.5$, $\theta_{\max} = 4.0$, $\theta_{\min} = 0.0$, $\Delta\theta = 0.2$
- (e) $\tau = 798.9$, $\theta_{\max} = 3.0$, $\theta_{\min} = 0.0$, $\Delta\theta = 0.2$

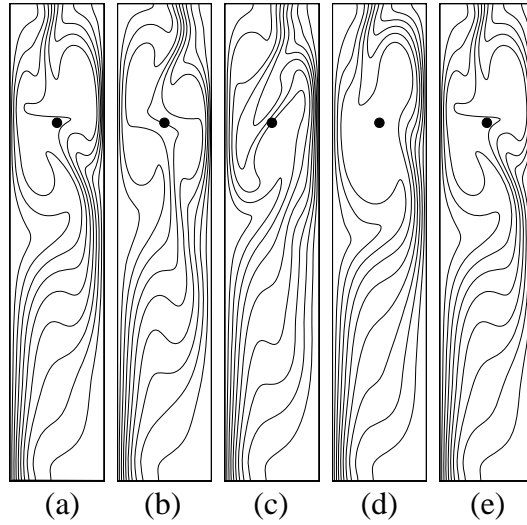


Figure B.16 Temperature fields at the wire position 1 ($V_0 = 12.0$ kV, $Ra = 10^4$, without Joule heating)

- (a) $\tau = 768.3$, $\theta_{\max} = 1.0$, $\theta_{\min} = 0.0$, $\Delta\theta = 0.2$
- (b) $\tau = 781.9$, $\theta_{\max} = 1.0$, $\theta_{\min} = 0.0$, $\Delta\theta = 0.2$
- (c) $\tau = 795.5$, $\theta_{\max} = 1.0$, $\theta_{\min} = 0.0$, $\Delta\theta = 0.2$
- (d) $\tau = 809.1$, $\theta_{\max} = 1.0$, $\theta_{\min} = 0.0$, $\Delta\theta = 0.2$
- (e) $\tau = 822.9$, $\theta_{\max} = 1.0$, $\theta_{\min} = 0.0$, $\Delta\theta = 0.2$

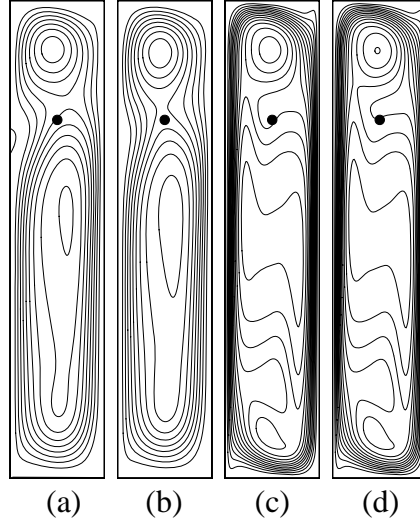


Figure B.17 Flow fields at the wire position 1 ($V_0 = 12.0$ kV)
 (a) $Ra = 10^5$, with Joule heating, $\Psi_{\max} = 0.01$, $\Psi_{\min} = -0.050$, $\Delta\Psi = 0.005$
 (b) $Ra = 10^5$, without Joule heating, $\Psi_{\max} = 0.00$, $\Psi_{\min} = -0.050$, $\Delta\Psi = 0.005$
 (c) $Ra = 10^6$, with Joule heating, $\Psi_{\max} = 0.00$, $\Psi_{\min} = -0.070$, $\Delta\Psi = 0.005$
 (d) $Ra = 10^6$, without Joule heating, $\Psi_{\max} = 0.00$, $\Psi_{\min} = -0.070$, $\Delta\Psi = 0.005$)

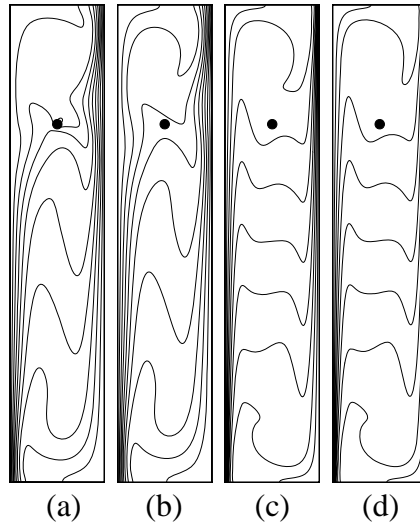


Figure B.18 Temperature at the wire position 1
 ($V_0 = 12.0$ kV, $\theta_{\max} = 1.0$, $\theta_{\min} = 0.0$, $\Delta\theta = 0.1$)
 (a) $Ra = 10^5$, with Joule heating
 (b) $Ra = 10^5$, without Joule heating
 (c) $Ra = 10^6$, with Joule heating
 (d) $Ra = 10^6$, without Joule heating

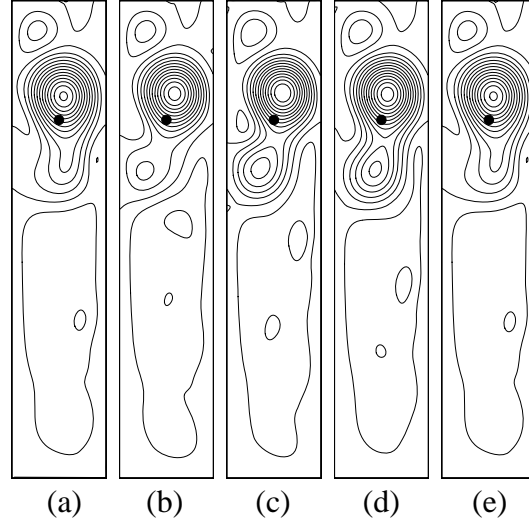


Figure B.19 Flow fields at the wire position 1 ($V_0 = 15.0$ kV, $Ra = 10^6$, with Joule heating)

- (a) $\tau = 1017.2$, $\Psi_{\max} = 0.130$, $\Psi_{\min} = -0.03$, $\Delta\Psi = 0.01$
- (b) $\tau = 1024.4$, $\Psi_{\max} = 0.120$, $\Psi_{\min} = -0.03$, $\Delta\Psi = 0.01$
- (c) $\tau = 1031.6$, $\Psi_{\max} = 0.120$, $\Psi_{\min} = -0.03$, $\Delta\Psi = 0.01$
- (d) $\tau = 1038.8$, $\Psi_{\max} = 0.130$, $\Psi_{\min} = -0.03$, $\Delta\Psi = 0.01$
- (e) $\tau = 1046.0$, $\Psi_{\max} = 0.130$, $\Psi_{\min} = -0.03$, $\Delta\Psi = 0.01$

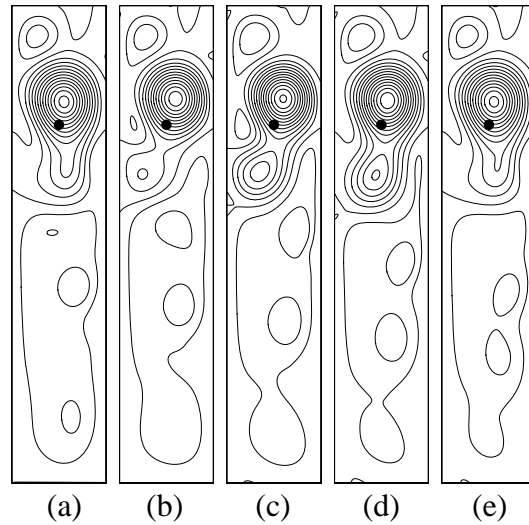


Figure B.20 Flow fields at the wire position 1 ($V_0 = 15.0$ kV, $Ra = 10^6$, without Joule heating)

- (a) $\tau = 1011.8$, $\Psi_{\max} = 0.130$, $\Psi_{\min} = -0.03$, $\Delta\Psi = 0.01$
- (b) $\tau = 1018.7$, $\Psi_{\max} = 0.120$, $\Psi_{\min} = -0.03$, $\Delta\Psi = 0.01$
- (c) $\tau = 1025.6$, $\Psi_{\max} = 0.130$, $\Psi_{\min} = -0.03$, $\Delta\Psi = 0.01$
- (d) $\tau = 1032.5$, $\Psi_{\max} = 0.130$, $\Psi_{\min} = -0.03$, $\Delta\Psi = 0.01$
- (e) $\tau = 1039.4$, $\Psi_{\max} = 0.130$, $\Psi_{\min} = -0.03$, $\Delta\Psi = 0.01$

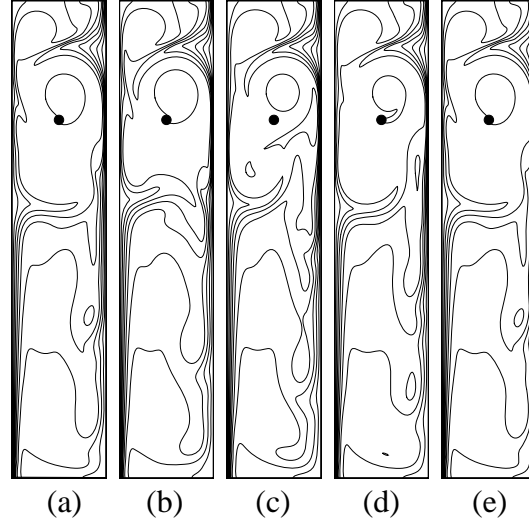


Figure B.21 Temperature fields at wire the position 1 ($V_0 = 15.0$ kV, $Ra = 10^6$, with Joule heating)

- (a) $\tau = 1017.2$, $\theta_{\max} = 1.0$, $\theta_{\min} = 0.0$, $\Delta\theta = 0.1$
- (b) $\tau = 1024.4$, $\theta_{\max} = 1.0$, $\theta_{\min} = 0.0$, $\Delta\theta = 0.1$
- (c) $\tau = 1031.6$, $\theta_{\max} = 1.0$, $\theta_{\min} = 0.0$, $\Delta\theta = 0.1$
- (d) $\tau = 1038.8$, $\theta_{\max} = 1.0$, $\theta_{\min} = 0.0$, $\Delta\theta = 0.1$
- (e) $\tau = 1046.0$, $\theta_{\max} = 1.0$, $\theta_{\min} = 0.0$, $\Delta\theta = 0.1$

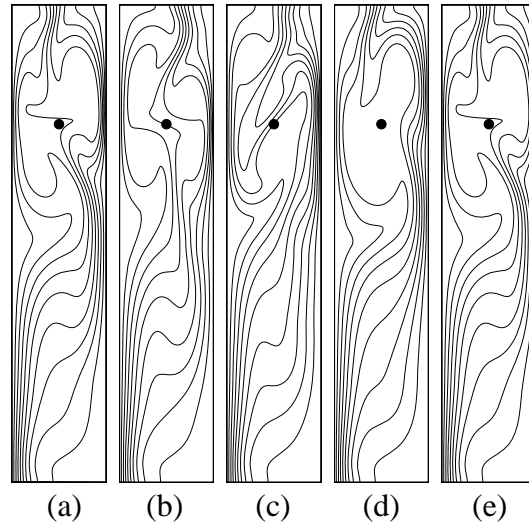


Figure B.22 Temperature fields at the wire position 1 ($V_0 = 15.0$ kV, $Ra = 10^6$, without Joule heating)

- (a) $\tau = 1011.8$, $\theta_{\max} = 1.0$, $\theta_{\min} = 0.0$, $\Delta\theta = 0.1$
- (b) $\tau = 1018.7$, $\theta_{\max} = 1.0$, $\theta_{\min} = 0.0$, $\Delta\theta = 0.1$
- (c) $\tau = 1025.6$, $\theta_{\max} = 1.0$, $\theta_{\min} = 0.0$, $\Delta\theta = 0.1$
- (d) $\tau = 1032.5$, $\theta_{\max} = 1.0$, $\theta_{\min} = 0.0$, $\Delta\theta = 0.1$
- (e) $\tau = 1039.4$, $\theta_{\max} = 1.0$, $\theta_{\min} = 0.0$, $\Delta\theta = 0.1$

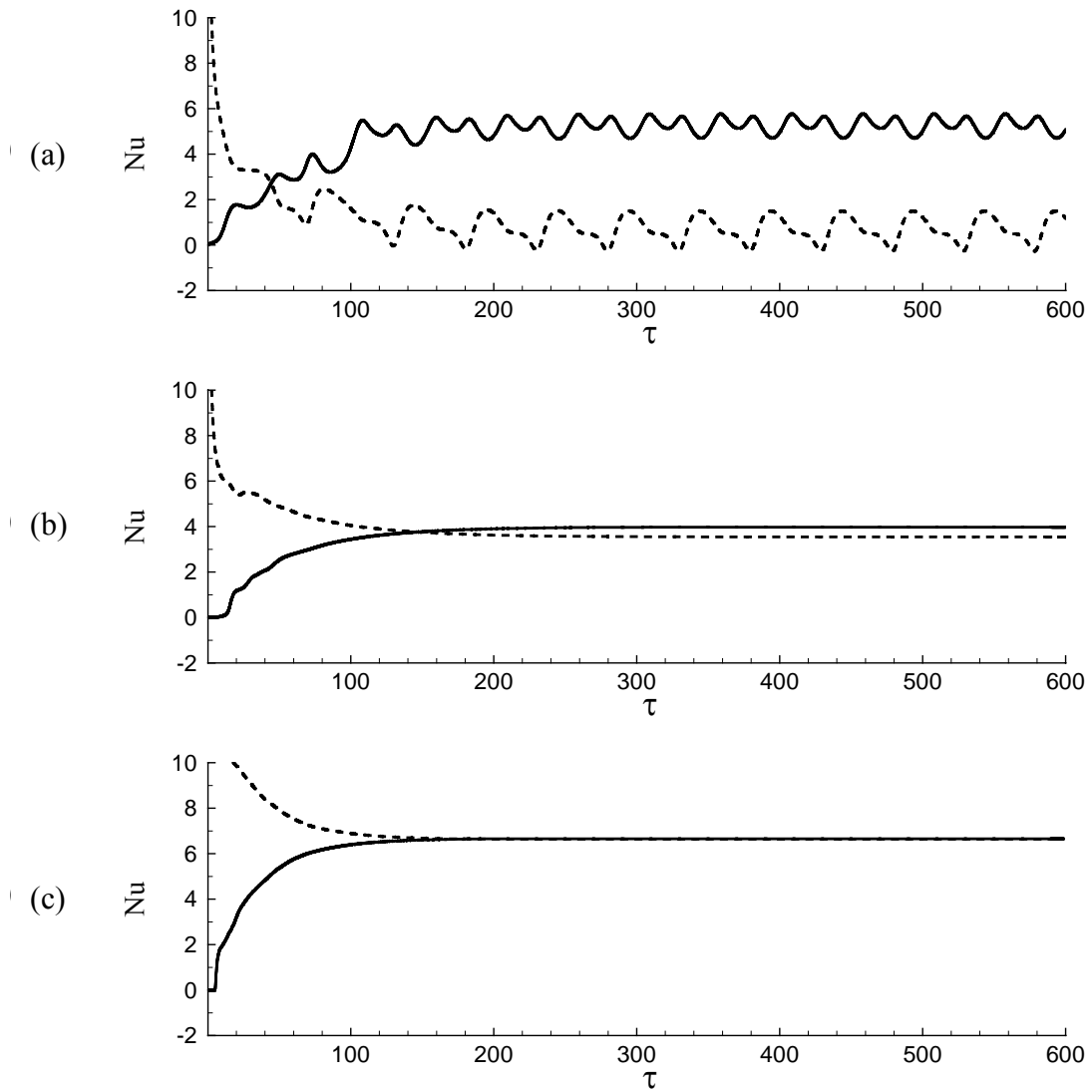


Figure B.23 Variation of Nusselt number with time for $V_0 = 12.0$ kV at the wire position 2 (with Joule heating, solid---cold wall, dashed--- hot wall)
 (a) $Ra = 10^4$, (b) $Ra = 10^5$, (c) $Ra = 10^6$

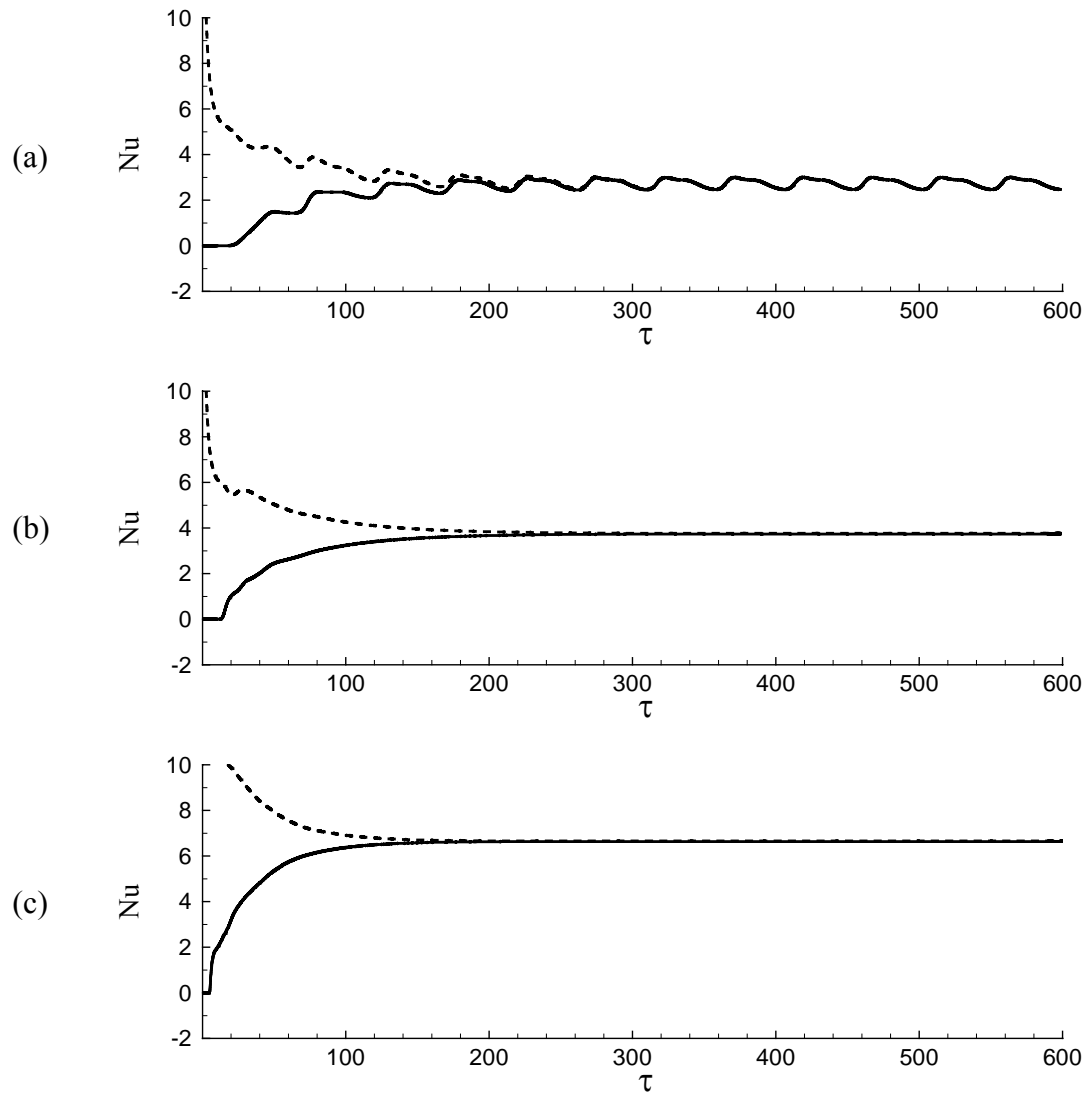


Figure B.24 Variation of Nusselt number with time for $V_0 = 12.0$ kV at the wire position 2 (without Joule heating, solid---cold wall, dashed--- hot wall)
 (a) $Ra = 10^4$, (b) $Ra = 10^5$, (c) $Ra = 10^6$

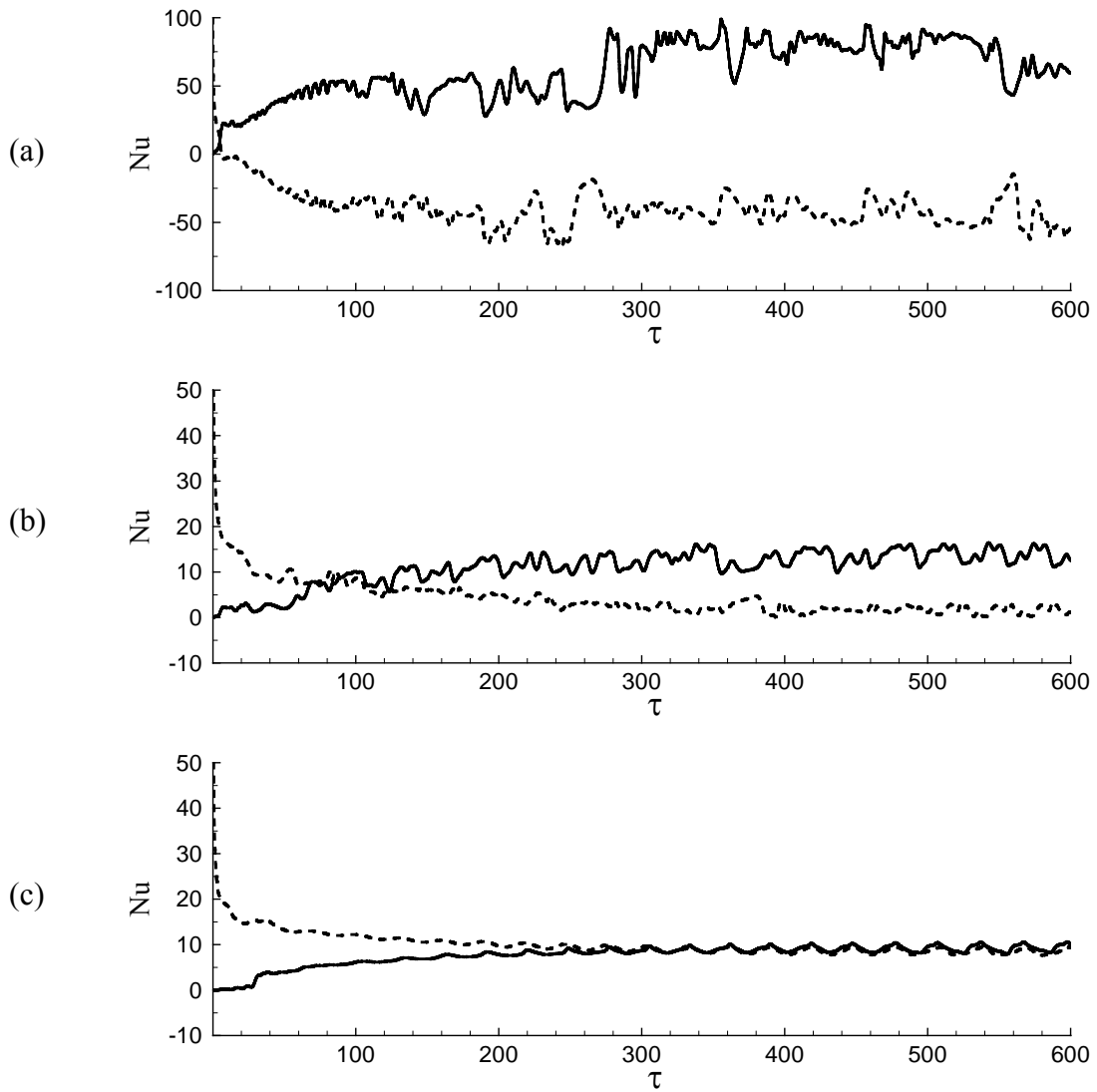


Figure B.25 Variation of Nusselt number with time for $V_0 = 15.0$ kV at the wire position 2 (with Joule heating, solid---cold wall, dashed--- hot wall)
 (a) $Ra = 10^4$, (b) $Ra = 10^5$, (c) $Ra = 10^6$

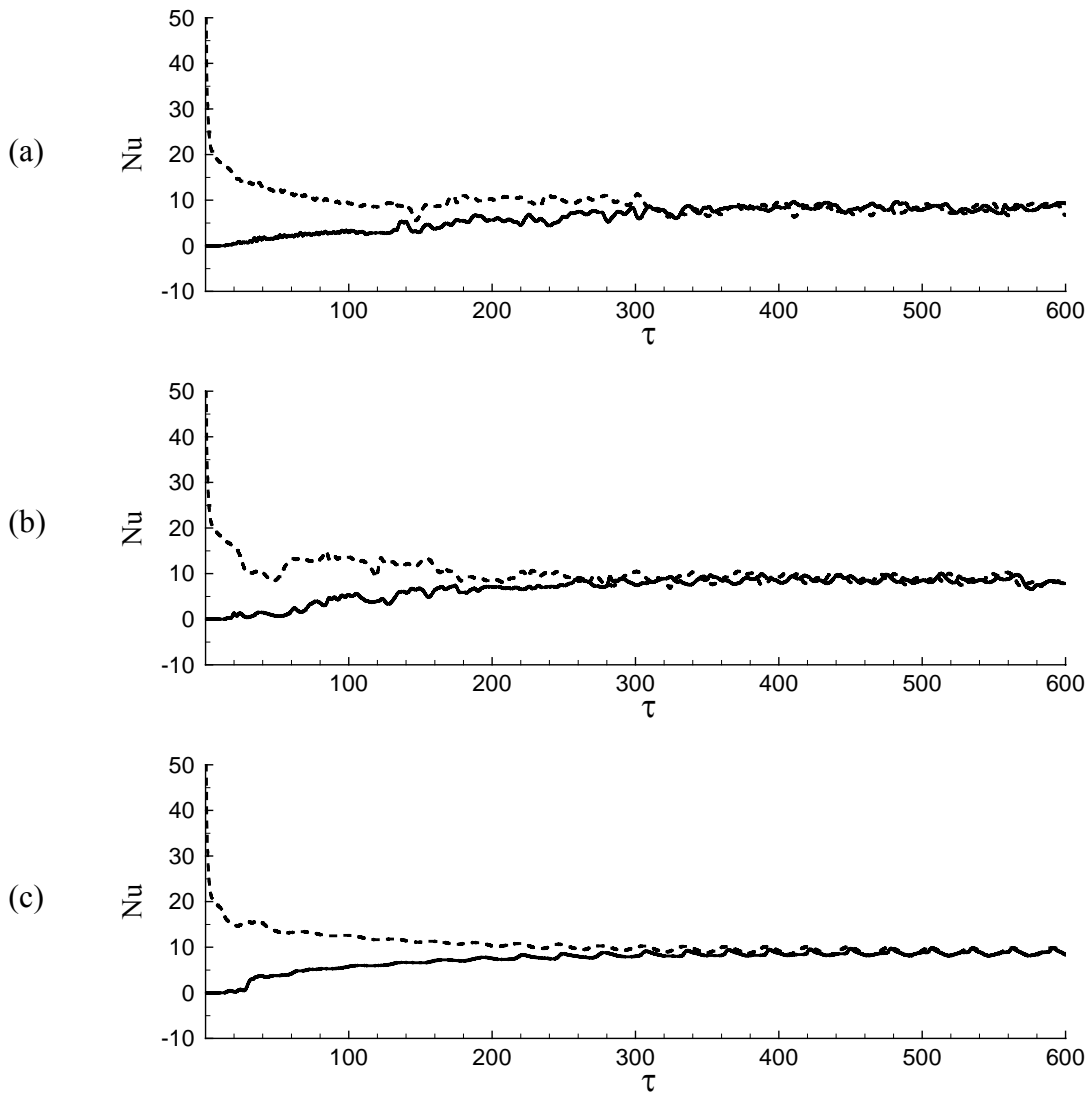


Figure B.26 Variation of Nusselt number with time for $V_0 = 15.0$ kV at the wire position 2 (without Joule heating, solid---cold wall, dashed--- hot wall)
 (a) $Ra = 10^4$, (b) $Ra = 10^5$, (c) $Ra = 10^6$

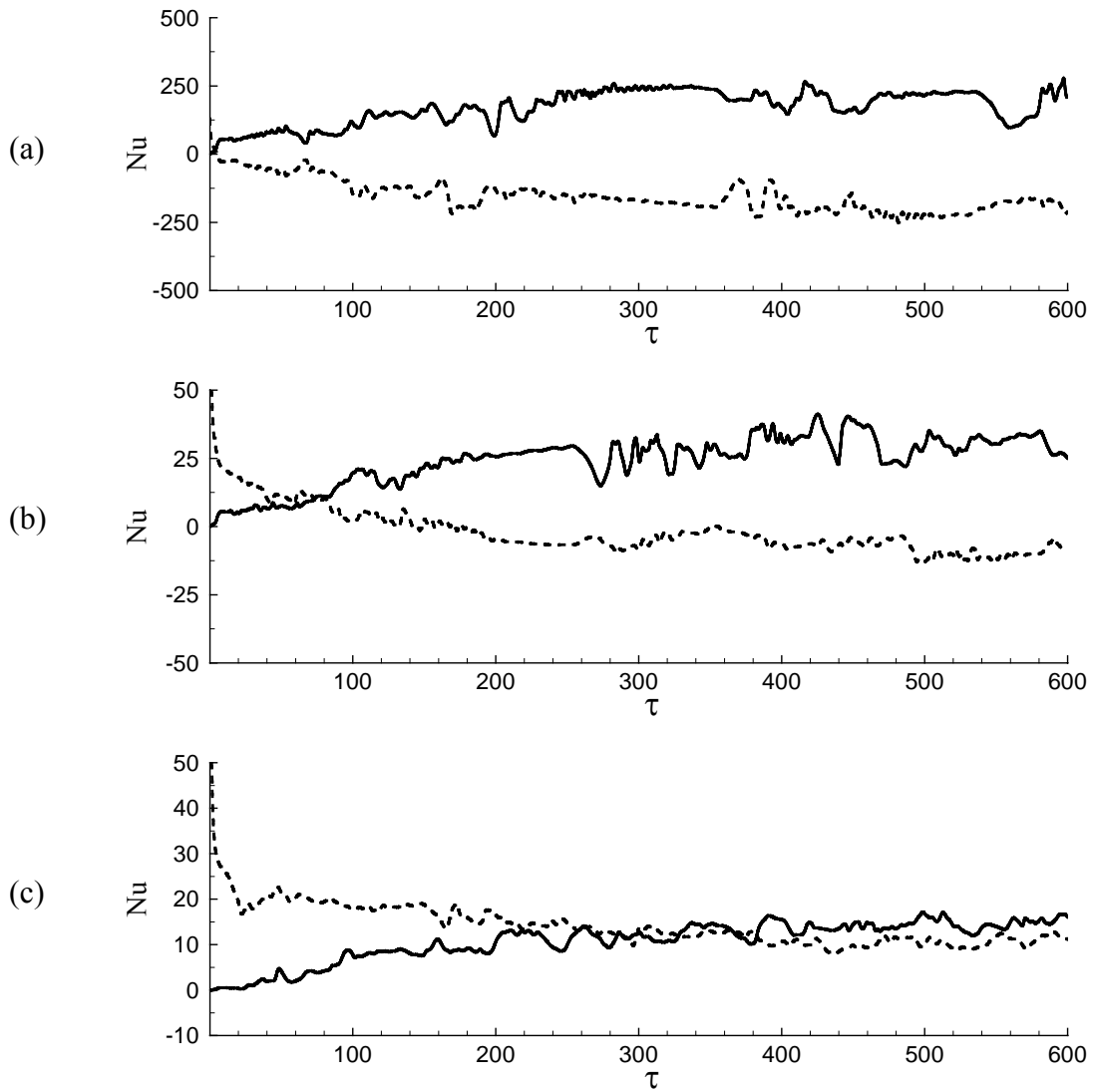


Figure B.27 Variation of Nusselt number with time for $V_0 = 18.0$ kV at the wire position 2 (with Joule heating, solid---cold wall, dashed--- hot wall)
 (a) $Ra = 10^4$, (b) $Ra = 10^5$, (c) $Ra = 10^6$

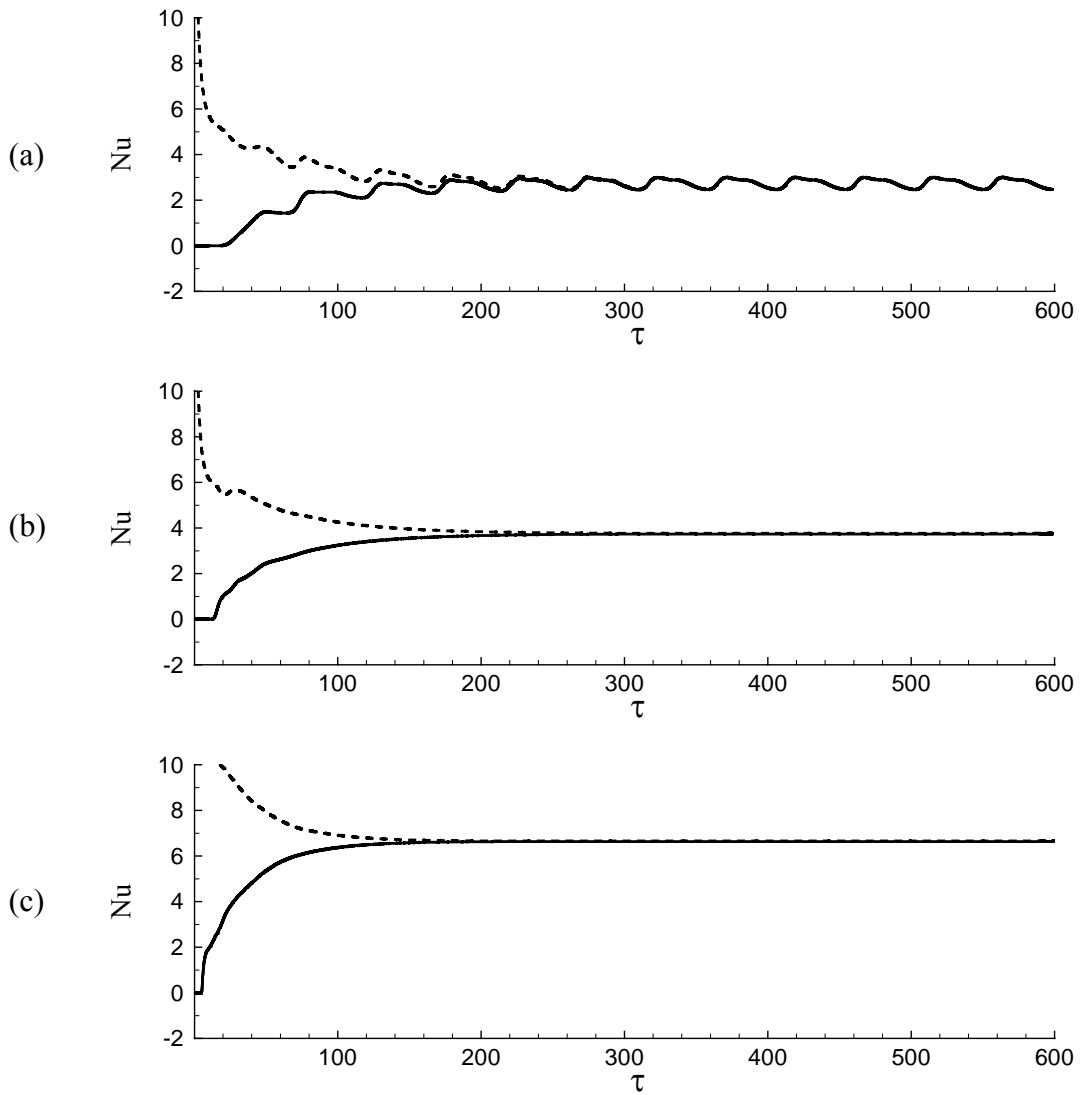


Figure B.28 Variation of Nusselt number with time for $V_0 = 18.0$ kV at the wire position 2 (without Joule heating, solid---cold wall, dashed--- hot wall)
 (a) $Ra = 10^4$, (b) $Ra = 10^5$, (c) $Ra = 10^6$

APPENDIX C

EXPERIMENT RESULTS

Table C.1 Positive corona discharge without cross-flow.....	151
Table C.2 Positive corona discharge with cross-flow ($u_i = 2.2$ m/s).....	151
Table C.3 Negative corona discharge without cross-flow.....	152
Table C.4 Negative discharge with cross-flow ($u_i = 2.2$ m/s).....	152

Table C.1 Positive corona discharge without cross-flow

Positive Discharge Without Cross-flow		Net weight lost		Average Ambient		Re _{EHD}	Sherwood Number		
Voltage	Current	Electrode	Ambient	Temp.	Humidity		Electrode Sh _e	Ambient Sh _a	Sh _e / Sh _a
kV	μA	g/s (10 ⁻⁴)		°C	RH%				
14	12.6	8.56	4.71	23.4	51.9	14.633	0.0986	0.0543	1.7945
15	19.5	14.84	5.85	25.5	30.4	18.039	0.1049	0.0413	2.5368
16	29.4	17.89	6.25	25.4	28.9	22.159	0.1247	0.0436	2.8624
17	40.2	20.17	6.28	26.0	29.1	25.846	0.1353	0.0421	3.2118
18	47.9	21.29	6.20	25.5	30.7	28.273	0.1511	0.0440	3.4339
19	63.9	21.29	5.80	26.2	35.5	32.558	0.1547	0.0422	3.6707
20	78.9	21.95	5.41	26.1	38.2	36.195	0.1676	0.0413	4.0573

Table C.2 Positive corona discharge with cross-flow (u_i = 2.2 m/s)

Positive Discharge With Cross-flow		Net weight lost		Average Ambient		N _{EHD}	Sherwood Number		
Voltage	Current	Electrode	Ambient	Temp.	Humidity		Electrode Sh _e	Ambient Sh _a	Sh _e / Sh _a
kV	μA	g/s (10 ⁻⁴)		°C	RH%				
14	14.4	25.58	6.76	27.2	37.8	0.216	0.1807	0.0478	3.7840
15	25.1	26.35	8.01	26.6	36.1	0.285	0.1883	0.0572	3.2896
16	38.0	27.22	7.28	27	33.3	0.351	0.1817	0.0486	3.7390
17	50.2	26.64	7.56	26.4	34.6	0.403	0.1885	0.0535	3.5238
18	67.0	27.60	7.61	27	32.6	0.466	0.1823	0.0503	3.6268
19	81.2	29.10	8.04	26.4	29.9	0.513	0.1922	0.0531	3.6194
20	93.7	29.98	9.52	26.5	27.4	0.551	0.1900	0.0603	3.1492

Table C.3 Negative corona discharge without cross-flow

Negative Discharge Without Cross-flow		Net weight lost		Average Ambient		Re _{EHD}	Sherwood Number		
Voltage	Current	Electrode	Ambient	Temp.	Humidity		Electrode Sh _e	Ambient Sh _a	Sh _e / Sh _a
kV	μA	g/s (10 ⁻⁴)		°C	RH%				
14	4.3	8.88	5.70	26.0	26.0	6.978	0.0571	0.0366	1.5580
15	13.5	11.79	5.74	24.0	43.5	12.471	0.1124	0.0643	2.0540
16	30.4	17.22	6.29	25.9	31.2	18.561	0.1198	0.0438	2.7377
17	38.3	18.10	7.04	25.5	33.5	20.870	0.1338	0.0595	2.5710
18	56.0	20.77	6.22	26.0	31.7	25.182	0.1446	0.0433	3.3392
19	74.0	23.53	6.98	25.7	28.8	28.983	0.1604	0.0476	3.3711
20	85.8	23.19	6.58	25.8	35.1	31.196	0.1721	0.0503	3.5243

Table C.4 Negative discharge with cross-flow (u_i = 2.2 m/s)

Negative Discharge With Cross-flow		Net weight lost		Average Ambient		N _{EHD}	Sherwood Number		
Voltage	Current	Electrode	Ambient	Temp.	Humidity		Electrode Sh _e	Ambient Sh _a	Sh _e / Sh _a
kV	μA	g/s (10 ⁻⁴)		°C	RH%				
14	19.8	16.01	5.50	23.7	50.3	0.209	0.1765	0.0606	2.9109
15	33.0	15.17	5.84	24.0	49.8	0.270	0.1627	0.0626	2.5976
16	42.2	17.00	5.96	23.2	49.6	0.305	0.1905	0.0668	2.8523
17	58.0	16.93	6.07	23.4	48.3	0.358	0.1828	0.0655	2.7891
18	79.2	16.59	6.33	22.9	49.5	0.418	0.1890	0.0721	2.6209
19	103.4	18.47	6.80	22.8	44.3	0.478	0.1921	0.0707	2.7162
20	133.2	21.16	7.12	23.0	40.7	0.542	0.2043	0.0687	2.9719